

# Methodical developments for preclinical stem cell tracking on a clinical 3 Tesla MRI

Ph.D. Thesis

conducted at the

Institute of Medical Engineering,  
Graz, University of Technology



by

**Clemens Diwoky**

December, 2014

Supervisor: Univ. Prof. Dipl.-Ing. Dr.techn. Rudolf Stollberger



Für Isabelle



## **Statutory Declaration**

I declare that I have authored this thesis independently, that I have not used other than the declared sources/resources and that I have explicitly marked all material which has been quoted either literally or by content from the used sources.

Graz,

## **Eidesstattliche Erklärung**

Ich erkläre an Eides statt, dass ich die vorliegende Arbeit selbstständig verfasst, andere als die angegebenen Quellen/Hilfsmittel nicht benutzt und die den benutzten Quellen wörtlich und inhaltlich entnommenen Stellen als solche kenntlich gemacht habe.

Graz, am

---

# Abstract

In recent years, MRI as a non-invasive radiation free modality of diagnostic imaging became an irreplaceable versatile technique for preclinical animal research. Dedicated animal MR systems do exist, but the broad availability of clinical MRI facilities and the cost-effectiveness of a combined clinical and preclinical use in conjunction with the high costs for dedicated animal systems make preclinical research on clinical MRI hardware very attractive.

Central to the present work are methodical developments of MR techniques able to visualize and assess the pathway of superparamagnetic iron oxide (SPIO) labeled functional stem cells in vivo. Aims followed by this thesis focus on an enhanced specificity and sensitivity of the produced cellular contrast and on robust scanning schemes facilitating artifact free sub-millimeter resolution images on clinical large bore systems. In this context it is demonstrated that 3D radial imaging trajectories are beneficial in the sense of reduced motional artifacts and desired background signal properties for detecting single iron oxide labeled cells in small mammals. Other techniques developed in this work employ the dipolar field pattern of iron oxide labeled stem cells in order to change the initially dark hypointense contrast of cells into a positive contrast which is better differentiable from heterogeneous tissue structures. Best results are obtained by employing this cellular magnetic footprint combined with high-resolution 3D radial imaging. A dedicated image reconstruction of the acquired datasets is able to gain positive contrast of single cells in vivo.

**Keywords:** *stem cell tracking with MRI, SPIO contrast, 3D radial acquisition, UTE, bUTE, off-resonant reconstruction*

---

# Zusammenfassung

Die MRT als nichtinvasives strahlenfreies bildgebendes Diagnoseverfahren wurde in den letzten Jahren zur unersetzlichen und vielseitigen Methode der präklinischen Tierforschung. Spezielle MRT Systeme für Kleintiere existieren zwar, aber die breite Verfügbarkeit von klinischen MRT Geräten und die Kosteneffizienz eines kombinierten klinisch- präklinischen Einsatzes sowie die hohen Kosten für spezielle Tiersysteme machen den Einsatz von klinischer MRT Hardware in der präklinischen Forschung sehr attraktiv.

Im Mittelpunkt der vorliegenden Arbeit stehen methodische Entwicklungen von MR-Techniken, welche in der Lage sind, in vivo den Verlauf von mit Eisenoxid (SPIO) markierten funktionellen Stammzellen zu visualisieren. Ziele dieser Arbeit fokussieren sich auf eine erhöhte Spezifität sowie Sensitivität des Zellkontrastes und auf robuste Akquisitionsstrategien, welche artefaktfreie Sub-Millimeter Auflösungen in klinischen MRT-Systemen erlauben sollen. In diesem Zusammenhang wird gezeigt, dass 3D radiale Trajektorien vorteilhaft sind im Sinne reduzierter Bewegungsartefakte und gewünschter Hintergrundsignaleigenschaften und zum Nachweis einzelner mit Eisenoxid markierter Zellen in kleinen Säugetieren führt. Andere Techniken, welche in dieser Arbeit entwickelt wurden, nutzen die dipolare Feldverteilung der Eisenoxidpartikel, um den zunächst dunklen, hypointensen Kontrast, in einen positiven, aus heterogenen Gewebestrukturen besser differenzierbaren Kontrast umzuwandeln. Die besten Ergebnisse werden durch die Verwendung dieses zellulären magnetischen Fußabdruckes kombiniert mit hochauflösender 3D radialen Bildakquise erzielt. Eine spezielle Bildrekonstruktion der so erhobenen Datensätze ist in der Lage, positiven Kontrast von Einzelzellen in vivo zu gewinnen.

**Schlüsselwörter:** *Stammzellen Detektion mittels MRT, SPIO Kontrast, 3D Radiale Akquisition, UTE, bUTE, nicht-resonante Rekonstruktion*

---

# Contents

<b>Abstract</b>	<b>vii</b>
<b>Zusammenfassung</b>	<b>ix</b>
<b>List of Figures</b>	<b>xvii</b>
<b>List of Tables</b>	<b>xxi</b>
<b>Glossary</b>	<b>xxiii</b>
<b>1 Introduction</b>	<b>1</b>
1.1 Main aims of the thesis . . . . .	3
1.2 Specific aims . . . . .	3
1.3 Structure of the thesis . . . . .	3
<b>2 Basic principles of MR guided cell tracking</b>	<b>7</b>
2.1 Contrasts for cellular imaging . . . . .	8
2.1.1 Relaxation . . . . .	8
2.1.1.1 Longitudinal relaxation $T_1$ . . . . .	8
2.1.1.2 Intrinsic transverse relaxation $T_2$ . . . . .	9
2.1.1.3 External transverse relaxation $T_2'$ . . . . .	9
2.1.1.4 Relaxation and imaging contrast . . . . .	10
2.1.2 Magnetic properties of materials used as MR contrast agents . .	10
2.1.2.1 Paramagnetism . . . . .	11
2.1.2.2 Superparamagnetism . . . . .	12
2.1.3 Iron oxide contrast agents . . . . .	12
2.1.3.1 Longitudinal relaxation of superparamagnetic iron oxides	12

## CONTENTS

---

2.1.3.2	Transverse relaxation caused by condensed paramagnetic structures . . . . .	14
2.2	Cell labeling and contrast agent quantification . . . . .	18
2.2.1	Contrast agents used for cellular labeling . . . . .	18
2.2.2	Cell labeling . . . . .	20
2.2.2.1	Cellular labeling and contrast agent efficiency . . . . .	22
2.2.2.2	Biocompatibility of MR contrast agents . . . . .	23
2.2.3	Quantification of cellular iron label . . . . .	24
2.2.3.1	Transmission electron microscopy . . . . .	24
2.2.3.2	ICP-MS & AAS . . . . .	24
2.2.3.3	Histochemical detection of iron . . . . .	25
2.2.3.4	Susceptometry . . . . .	26
2.3	Acquisition strategies for cell tracking with MRI . . . . .	31
2.3.1	Gradient Echo Sequences . . . . .	31
2.3.1.1	$T_2^*$ contrast of GRE acquisitions . . . . .	33
2.3.1.2	Synergistic $T_1$ - $T_2^*$ contrast . . . . .	34
2.3.1.3	Cell tracking studies based on GRE . . . . .	35
2.3.2	Fully Balanced Steady State Sequences . . . . .	37
2.3.2.1	$T_2^*$ contrast in the steady state . . . . .	38
2.3.2.2	Cell tracking studies based on bSSFP . . . . .	42
2.3.3	Sequences producing positive cellular contrast . . . . .	43
2.3.3.1	Cell tracking studies based on positive contrast techniques . . . . .	44
2.4	Technical considerations at imaging sub-millimeter resolutions on clinical MRI hardware . . . . .	45
2.4.1	SNR . . . . .	45
2.4.2	Main magnetic fieldstrength . . . . .	48
2.4.3	RF-coils . . . . .	49
2.4.4	Signal averaging . . . . .	51
2.4.5	Gradient performance . . . . .	51

<b>3</b>	<b>Amplification strategies for cell tracking with Cartesian trajectories</b>	<b>55</b>
3.1	Enhanced contrast of single cells through zero-padding . . . . .	56
3.1.1	Introduction . . . . .	56
3.1.2	Theory . . . . .	58
3.1.2.1	Cellular contrast and the image point spread function . . . . .	58
3.1.2.2	Zero-padding . . . . .	59
3.1.3	Methods . . . . .	60
3.1.3.1	Simulations . . . . .	60
3.1.3.2	In vitro experiments . . . . .	60
3.1.3.3	Reconstruction . . . . .	61
3.1.4	Results . . . . .	61
3.1.5	Discussion . . . . .	64
3.2	Mapping field perturbations for cell tracking with positive contrast . . . . .	66
3.2.1	Introduction . . . . .	66
3.2.2	Theory . . . . .	66
3.2.3	Sequence development . . . . .	68
3.2.3.1	Saturation by inversion recovery . . . . .	68
3.2.3.2	Narrow bandwidth inversion pulses . . . . .	70
3.2.3.3	Sequence timing . . . . .	72
3.2.4	Methods . . . . .	74
3.2.4.1	RF pulse design . . . . .	74
3.2.4.2	RF excitation profile measurements . . . . .	74
3.2.4.3	NMR of the ilium . . . . .	75
3.2.4.4	In vitro measurements . . . . .	75
3.2.5	Results . . . . .	76
3.2.6	Discussion . . . . .	80
<b>4</b>	<b>Cell tracking with 3D radial UTE</b>	<b>83</b>
4.1	Introduction to radial MRI . . . . .	84
4.1.1	Acquisition of radial data . . . . .	84
4.1.2	Nyquist criterium in radial MRI and the effect of undersampling . . . . .	86
4.1.3	Reconstruction . . . . .	87
4.1.4	Features of radial sampling for preclinical MRI . . . . .	88

## CONTENTS

---

4.1.4.1	Background SNR and SNR of reduced acquisitions . . .	88
4.1.4.2	Image artifacts due to motion . . . . .	89
4.2	3D UTE . . . . .	91
4.2.1	Introduction . . . . .	91
4.2.2	Sequence development . . . . .	91
4.2.2.1	K-space trajectory . . . . .	91
4.2.2.2	Non-uniform sampling during gradient ramp-up . . . . .	94
4.2.2.3	Transmit/receive switching delay . . . . .	95
4.2.2.4	Corrections for gradient imperfections . . . . .	97
4.2.3	Methods . . . . .	100
4.2.3.1	In vivo cell tracking model . . . . .	100
4.2.3.2	In vivo imaging . . . . .	101
4.2.4	Results . . . . .	101
4.2.5	Discussion . . . . .	103
<b>5</b>	<b>Cell tracking with 3D radial UTE trajectories in coherent steady state</b>	<b>105</b>
5.1	bSSFP imaging with half-echo acquisition . . . . .	106
5.1.1	Introduction . . . . .	106
5.1.2	Theory . . . . .	106
5.1.3	Methods . . . . .	108
5.1.3.1	Pulse sequence and reconstruction . . . . .	108
5.1.3.2	Contrast phantom preparation . . . . .	108
5.1.3.3	Relaxometry . . . . .	109
5.1.3.4	Phantom measurements . . . . .	110
5.1.3.5	In vivo imaging . . . . .	110
5.1.4	Results . . . . .	111
5.1.4.1	Phantom measurements . . . . .	111
5.1.4.2	In vivo imaging . . . . .	114
5.1.5	Discussion . . . . .	115
5.2	Single cell detection using off-resonant reconstructions of 3D center-out bSSFP . . . . .	118
5.2.1	Introduction . . . . .	118
5.2.2	Theory . . . . .	118

5.2.3	Methods . . . . .	121
5.2.4	Results . . . . .	124
5.2.5	Discussion . . . . .	131
<b>6</b>	<b>Summary &amp; Discussion</b>	<b>135</b>
6.1	Summary . . . . .	135
6.2	Discussion & Future Work . . . . .	136
6.2.1	Translating preclinical cell tracking to clinical practice . . . . .	138
<b>A</b>	<b>Shinnar Le Roux (SLR) Transform</b>	<b>141</b>
A.1	SLR-based RF pulse design . . . . .	142
	<b>References</b>	<b>147</b>
	<b>Curriculum Vitae</b>	<b>157</b>
	<b>List of Publications</b>	<b>159</b>
	<b>Acknowledgements</b>	<b>165</b>

## CONTENTS

---

# List of Figures

2.1	Transmission electron microscopy of iron oxide labeled MSCs . . . . .	25
2.2	Microscopy of Prussian blue stained EPC network . . . . .	26
2.3	Suszeptometric measurement of cellular BMS . . . . .	29
2.4	$T_1$ and $T_2^*$ contrast regime of SPIOs . . . . .	34
2.5	bSSFP signal response to off-resonances . . . . .	40
2.6	bSSFP signal response to iron loaded cells . . . . .	41
2.7	Scale between human and preclinical MRI. . . . .	45
2.8	Principle of NMR signal reception. . . . .	46
2.9	Gradient performance and TE. . . . .	54
3.1	Negative contrast due to intra-voxel phase dispersion and contrast re- duction in dependence of intra-cellular positioning. . . . .	57
3.2	Contrast reduction from a displaced imaging grid for a 50 pg Fe cell. . .	62
3.3	Expected contrast gain for different cellular iron loads through re-alignment of cells with the imaging grid. . . . .	63
3.4	In-vitro result: Enhanced cellular contrast through zero-padding . . . .	64
3.5	Enhanced cellular contrast with zero-padding; comparison with high res- olution images . . . . .	65
3.6	Half width at full maximum of the proton NMR peak of both, free and lipid bound protons, is enlarged in closed proximity to paramagnetic objects. . . . .	67
3.7	Saturating on-resonant water, regions closed to paramagnetic objects are highlighted. . . . .	68
3.8	Dual band enhanced susceptibility imaging; Pulse sequence. . . . .	73
3.9	Quality of SLR saturation pulses . . . . .	76

## LIST OF FIGURES

---

3.10	1H spectra of four different regions in the iliac crest. . . . .	77
3.11	Comparison of the cellular contrast of GRE, IRON and the proposed dual band saturation technique . . . . .	78
3.12	Cellular contrast quantification of GRE, IRON and dual band positive contrast imaging. . . . .	79
3.13	Comparison of IRON to the proposed dual band technique. . . . .	80
4.1	2D radial PA . . . . .	85
4.2	Imaging iron loaded cells in heterogeneous background tissues. . . . .	92
4.3	3D UTE pulse sequence diagram and k-space trajectory . . . . .	93
4.4	Sampling delay at UTE imaging caused by decoupling of the receive coils. . . . .	96
4.5	Schematic of k-space measurement. . . . .	99
4.6	Comparison of 2D GRE, 3D GRE and 3D UTE for cell tracking. . . . .	102
5.1	Comparison of echo-centered bSSFP compared to half-echo bSSFP (bUTE) . . . . .	107
5.2	Phantom measurements comparing bUTE to echo-centered bSSFP tissue contrast. . . . .	112
5.3	Quantitative contrast analysis of balanced half-echoes compared to echo centered bSSFP. . . . .	113
5.4	In vivo comparison of 3D UTE, echo-centered bSSFP and bUTE. . . . .	115
5.5	In vivo comparison of 2D GRE, 3D UTE and 3D bUTE. . . . .	116
5.6	Effect of the 3D radial half-echo PSF to off-resonant spins. . . . .	119
5.7	Off-resonant reconstructed image representation. . . . .	124
5.8	Off-resonant reconstruction spectrum in dependency of imaging bandwidth and iron load. . . . .	125
5.9	Cellular contrast gained by off-resonant reconstruction in dependence of cellular iron load and imaging resolution. . . . .	126
5.10	Off-resonant signal change for varying echo center positions. . . . .	126
5.11	Off-resonant reconstruction of a single cell phantom. . . . .	127
5.12	Off-resonant reconstruction at different imaging resolutions. . . . .	128
5.13	Boxplots comparing the in vitro on-resonant bSSFP CNR with the off-resonant reconstruction technique. . . . .	129
5.14	In vivo application of the off-resonant reconstruction. . . . .	130

## LIST OF FIGURES

---

5.15 Off-center intra-voxel position modulates the off-resonant reconstruction spectrum. . . . .	133
A.1 SLR RF pulse design: Nutation caused by the $j$ th hard pulse. . . . .	142

## LIST OF FIGURES

---

# List of Tables

4.1	Measurement parameters for the in vivo UTE experiment. . . . .	101
5.1	Radial half-echo bSSFP tissue phantom properties. . . . .	109
5.2	Measurement parameters for the bUTE phantom experiment. . . . .	110
5.3	Measurement parameters for the bUTE in vivo experiment. . . . .	111
5.4	SNR measurements comparing bUTE to echo-centered bSSFP. . . . .	113

## GLOSSARY

---

# Glossary

<b>AAS</b>	atomic absorption spectroscopy	<b>FLASH</b>	fast low-angle shot; spoiled GRE
<b>ADC</b>	analog to digital converter	<b>FOV</b>	field-of-view
<b>B</b>	magnetic flux density	<b>FT</b>	Fourier transform
<b>B<sub>0</sub></b>	MR main magnetic flux density	<b>G</b>	linear magnetic gradient field
<b>BMS</b>	bulk magnetic susceptibility	<b>GRAPPA</b>	parallel imaging reconstruction in Fourier space
<b>bSSFP</b>	balanced steady state free precession; true fast imaging with steady-state free precession (TrueFISP)	<b>GRE</b>	gradient recalled echo
<b>bUTE</b>	balanced ultra-short time to echo	<b>H</b>	magnetic field
<b>BW</b>	bandwidth	<b>ICP-MS</b>	inductively coupled plasma mass spectroscopy
<b>CA</b>	contrast agent	<b>IFFT</b>	inverse fast Fourier transform
<b>CNR</b>	contrast-to-noise ratio	<b>ISO-center</b>	center of the magnet where imaging gradients have zero magnetic field
<b>CR</b>	contrast ratio	<b>LMD</b>	local magnetic dose
<b>CS</b>	chemical shift	<b>M</b>	magnetization
<b>CT</b>	X-ray computed tomography	<b>MIP</b>	minimum intensity projection
<b>DFT</b>	discrete Fourier transform	<b>MR</b>	magnetic resonance
<b>DT</b>	sampling dwell time	<b>MRI</b>	magnetic resonance imaging
<b>ECFC</b>	endothelial colony forming progenitor cell	<b>MSC</b>	mesenchymal stem cell
<b>EP</b>	electroporation	<b>NEX</b>	number of excitations; number of repeated measurements
<b>FDA</b>	food and drug administration	<b>NMR</b>	nuclear magnetic resonance
<b>FFT</b>	fast Fourier transform	<b>ORRS</b>	off-resonant reconstruction spectrum
<b>FID</b>	free induction decay; At UTE imaging, the acquisition directly after excitation.	<b>PA</b>	projection acquisition
		<b>PBS</b>	phosphate buffered saline
		<b>PET</b>	positron emission tomography
		<b>PNS</b>	peripheral nerve stimulation
		<b>PSF</b>	point spread function
		<b>R<sub>1</sub></b>	$1/T_1$ ; $T_1$ relaxation rate
		<b>r<sub>1</sub></b>	$T_1$ relaxivity
		<b>R<sub>2</sub></b>	$1/T_2$ ; $T_2$ relaxation rate
		<b>r<sub>2</sub></b>	$T_2$ relaxivity

## GLOSSARY

---

<b>RF</b>	radio frequency	<b>T<sub>2</sub></b>	transverse relaxation time, spin-spin relaxation time
<b>RF pulse</b>	radio frequency pulse; The transversal circular polarized radiofrequency field used to excite the spins	<b>T<sub>aq</sub></b>	acquisition time; total scan time
<b>ROS</b>	reactive oxygen species	<b>T1</b>	longitudinal relaxation time; spin-lattice relaxation time
<b>SENSE</b>	sensitivity encoding; parallel imaging reconstruction in image space	<b>TE</b>	time to echo
<b>SNR</b>	signal-to-noise ratio	<b>TEM</b>	transmission electron microscopy
<b>SOS</b>	sum-of-squares	<b>TF</b>	turbo factor of TSE, FSE or RARE
<b>SPECT</b>	single photon emission computed tomography	<b>TI</b>	inversion time
<b>SPIO</b>	super paramagnetic iron oxide	<b>TR</b>	repetition time
<b>SWIFT</b>	sweep imaging with Fourier transformation	<b>TSE</b>	turbo spin echo; fast spin echo (FSE); rapid acquisition with relaxation enhancement (RARE)
<b>T'<sub>2</sub></b>	relaxation time caused by static field inhomogeneities	<b>USPIO</b>	ultrasmall super paramagnetic iron oxide
<b>T<sub>2</sub>*</b>	effective transversal relaxation time	<b>UTE</b>	ultra-short time to echo
		<b>ZP</b>	zero padding

# 1

## Introduction

Preclinical research on small mammals, especially rodents, is of essential impact on medical basic research. Genetically modified mice are relatively easy to breed and keep models for human diseases [1]. In the past, using invasive diagnostic methods, large numbers of animals had to be killed at predefined intervals in order to get longitudinal information. With non-invasive imaging techniques, less animals are required and no animals need to be sacrificed during the study, hence longitudinal studies can be made in vivo, and data is even better comparable [2, 3]. Therefore, non-invasive imaging, especially MRI, gained importance not only in clinical, but also in preclinical research. Among several existing modalities for in vivo imaging of small rodents which are in preclinical use, MRI offers many additional benefits. In contrast to in vivo fluorescence imaging, MRI offers a view on organs localized far below the surface [4]. Other than micro-PET, two-photon imaging and SPECT [5], MRI offers good spatial and temporal resolution. MRI beats micro-CT [6] and digital subtraction angiography [7] concerning soft-tissue resolution. Furthermore, the use of contrast agents in MRI [8] helps to show pathologic processes like inflammation, tumors or cardiac infarction.

### Cell Tracking

The goal of cell tracking is to monitor the fate of single cells in live organs. Tracking the distribution of injected cells promises to solve the limitation in optimizing novel cell transplantation strategies by delivering information on the time scales of cell homing and the capability of monitoring the cell migration process [9, 10, 11, 12, 13]. From this

## 1. INTRODUCTION

---

information, dosage and timing of stem cell injection can be optimized for individual pathologies.

The recent ability to visualize cells by labeling with MR specific contrast agents has changed the paradigm of cell tracking which formerly used to be an invasive, histology based procedure to the non-invasive imaging modality of MRI [12, 14]. Applications are found in oncology tracking macrophages and lymphocytes to tumor sites [11], in studying myocardial repair after infarction by imaging stem cell traffic to the infarction site [13], in neurology by tracking neural precursors to stroke [10], or in stem cell transplantation monitoring early tissue rejection [9].

The presented thesis was motivated by stem cell therapies for leukemia patients initiated by a collaboration with the Stem Cell Research Unit at the Institute of Hematology, Medical University of Graz. The common goal was to develop an MRI based single cell tracking method which allows for an early detection of host-versus-graft disease by monitoring homing and/or rejection of donor cells within bone marrow.

**Why single cell detection?** Cellular imaging with MRI has to cope with the detection of single cells, rather than huge populations because:

- Imaging cell migration processes in vivo is accompanied by a high dilution of the administered cells in the vascular system. Therefore, a minor fraction of the labeled cells will approach the final target.
- A reduced cellular concentration may be desirable if cells are injected directly into the target tissue where cell migration processes are to be investigated. At high local cell dosages, the image background signal may be degraded by the high amount of contrast agent and, thus, obstruct the visibility of cellular pathways.
- Labeling a minor fraction of the applied therapeutic stem cells may be desirable, as biocompatibility issues of labeled entities cannot be excluded.

## 1.1 Main aims of the thesis

- To develop MR acquisition and reconstruction methods which allow for:
  1. In vivo imaging of single labeled cells in rodents on clinical MRI hardware.
  2. Improve the sensitivity and specificity of the acquired images to the labeled entities.

## 1.2 Specific aims

- To employ standard imaging techniques with changes to:
  1. Their image reconstruction in order to enhance cellular sensitivity.
  2. The preparation pulses preceding the sequence readout in order to enhance cellular specificity by producing a hyperintense cellular contrast.
- To show that image acquisition based on radial trajectories is highly beneficial in preclinical cell tracking especially with the given gradient performance of clinical MRIs.
- To implement a 3D radial acquisition allowing for ultra-short echo times in order to gain
  1. Motion insensitive high resolution images.
  2. High tissue background signal to improve cellular detection.
- To show that acquisition of the fully balanced steady state in conjunction with 3D radial half-echo acquisition improves image SNR and cellular CNR.
- To show that 3D radial half echo bSSFP imaging allows for a unique cellular contrast employing a new developed image reconstruction technique.

## 1.3 Structure of the thesis

### Chapter 2: Basic principles of MR guided cell tracking

A review on the contrast mechanisms and contrast agents used for cell tracking is presented. Cellular labeling strategies as well as cellular contrast agent quantification are discussed. In addition, state of the art MR acquisition techniques and cell tracking studies are presented. Finally, the chapter closes with a brief summary on the challenges that come with the implementation of preclinical MRI methods on clinical MR hardware.

## 1. INTRODUCTION

---

### **Chapter 3: Amplification strategies for cell tracking with Cartesian trajectories**

Standard MR acquisition strategies are employed and adopted for cell tracking with high specificity and sensitivity. Section *Enhanced contrast of single cells through zero-padding* describes the relationship between time-discrete data acquisition and final image representation of magnetically labeled cells. A method is described which allows for a boost in cellular contrast based on an a priori knowledge about the contrast mechanisms of iron loaded cells and the concepts of data-windowing. This section is based on the conference proceeding *Enhanced contrast of punctuate paramagnetic structures through zero-padding* [15]. Section *Mapping field perturbations for cell tracking with positive contrast* discusses the design of an MRI pulse sequence exploiting the field perturbation produced by paramagnetically loaded cells for cell tracking with positive contrast. The proposed approach focuses on the application in bone marrow where a major fraction of proton signal originates from lipids. This section is based on the conference proceeding *MRI of Stem Cells in Bone Marrow* [16] and *High Sensitivity Positive Contrast Imaging of Stem Cells in Bone Marrow* [17].

### **Chapter 4: Cell tracking with 3D radial UTE**

*Introduction to radial MRI* introduces the basic idea of non-Cartesian, radial data acquisition for preclinical MRI. The employed trajectory design as well as the properties of radial MR data acquisition and reconstruction for high resolution preclinical imaging are discussed. This chapter is based on the conference proceeding *Robust In-vivo Detection of SPIO Labeled Cells with MRI* [18]. The next section, *3D UTE*, discusses the use of ultra-short TE gradient echo sequences in the context of cellular imaging. This chapter is based partly on the conference proceedings *UTE Imaging for Single Cell Detection with Positive Contrast* [19], *On Possible Pitfalls in Working on SPIO Labelled Cells with 2D UTE Sequences* [20] and *Robust In-vivo Detection of SPIO Labeled Cells with MRI* [18].

## Chapter 5: Cell tracking with 3D radial UTE trajectories in coherent steady state

This chapter introduces the acquisition scheme of 3D radial center out bSSFP. The first section *bSSFP imaging with half-echo acquisition* is based partially on the conference proceeding *3D radial bUTE* [21]. Section *Single cell detection using off-resonant reconstructions of 3D center-out bSSFP* presents a new acquisition and reconstruction scheme for positive contrast imaging of single labeled cells. It is based on the journal publication *Positive contrast of SPIO-labeled cells by off-resonant reconstruction of 3D radial half-echo bSSFP* [22] with the individual author contributions:

- Clemens Diwoy: Basic concept on the off-resonant reconstruction of 3D half-echo bSSFP for cell tracking, numerical simulations, pulse sequence development, reconstruction and MRI measurements.
- Daniel Liebmann: Cell labeling, viability and functionality tests.
- Bernhard Neumayer: Assistance in the preparation of the manuscript, post-processing and data interpretation.
- Andreas Reinisch: Large scale propagation of stem cells, viability and functionality tests and labeling of cells.
- Florian Knoll: Assistance in the reconstruction of the 3D radial datasets and implementation of the reconstruction on the graphics processing unit.
- Dirk Strunk: General assistance during all stem cell tasks and preparation of the manuscript.
- Rudolf Stollberger: General assistance during all tasks, including methodological work and preparation of the manuscript.

## Chapter 6: Summary & Discussion

Summarizes the work and highlights the contributions of this thesis to the field of preclinical cellular imaging. An outlook is provided to which extent the presented work can be translated into clinical practice.

## 1. INTRODUCTION

---

2

## Basic principles of MR guided cell tracking

### 2.1 Contrasts for cellular imaging

Contrast in MRI is defined as the magnitude difference of the measured signal between two tissues under investigation. Assuming a constant coil sensitivity, the measured signal corresponds to the transversal magnetization of a tissue sample as discussed in chapter 2.4.1 dealing with signal-to-noise. The acquired magnetization magnitude depends on external factors such as the polarizing field strength and the MR pulse sequence used to acquire the signal on the one hand, and inherent tissue contrast properties such as proton density, relaxation and proton exchange mechanisms on the other. Given a tissue of interest which is to be imaged with high contrast from the surrounding tissue, often referred to as background signal, the MRI pulse sequence is chosen so as to benefit from the inherent contrast mechanism which differs most dominantly.

In cell tracking, the objects under investigation are cells which inherently do not possess MR properties that differ from those of the non-targeted (background) tissue. Therefore, a key requirement for cell tracking is the availability of labeling agents which significantly modulate the MR contrast of the administered cells. The most common way of enhancing MR contrast is to change the relaxation rate of free water protons by a labeling agent.

#### 2.1.1 Relaxation

##### 2.1.1.1 Longitudinal relaxation $T_1$

In a constant magnetic field  $B_0$ , the longitudinal component of the nuclear steady state spin system, condensed as net magnetization  $M_0$ , is orientated in parallel to the main polarizing field  $B_0$ . This spin system can absorb energy from a radio frequency (RF) field [23, 24, 25] with a frequency corresponding to  $f_0 = \gamma B_0$ , with  $\gamma$  the nuclei specific gyromagnetic ratio. The result is a transition between the parallel (low-energy) to the anti-parallel (high-energy) state of the spins, tilting the net magnetization  $M_0$  from the longitudinal ( $B_0$  orientated) to the transversal plane. If the radio frequency source is switched off, the spins undergo an energy exchange with the surrounding lattice leading to a continuous loss of energy of the excited spin system. The main energy transfer is evoked by interactions with the electron spin orbits of neighbored atoms and molecules at the frequency of nuclear spin precession  $\omega_0 = 2\pi f_0$ . As a consequence, the spins return to the state of thermal equilibrium in the direction of the main field  $B_0$ . This

mechanism can be described by the longitudinal or spin-lattice relaxation time  $T_1$ . The recovery of the longitudinal component of the magnetization  $M_z$  follows

$$\frac{dM_z}{dt} = -\frac{M_z - M_0}{T_1} \quad (2.1)$$

where  $M_z - M_0$  tends to zero with  $e^{-t/T_1}$ . At room temperature  $T_1$  is typically in the range of 0.1 to 10 seconds for protons in dielectric materials.

### 2.1.1.2 Intrinsic transverse relaxation $T_2$

After excitation with an external RF field, the transversal net component of the magnetization  $M_{xy}$  is phase coherent with the rotating excitation field. Due to fluctuations in the microscopic magnetic field environment caused by magnetic dipole moments of neighboring atoms as well as unpaired electrons, the initial synchronous precession of the spins is disrupted, and the phase coherence of the spin system is lost. This irreversible loss in phase coherence reduces the net transversal component  $M_{xy}$  exponentially with a decay time  $T_2$ :

$$\frac{dM_{xy}}{dt} = -\frac{M_{xy}}{T_2}. \quad (2.2)$$

Because dipolar interactions are the source for this decay, it is often referred to as dipole-dipole interaction or transversal relaxation. For solids it is usually found that  $T_1 \gg T_2$  and liquids  $T_1 \approx T_2$ .  $T_2$  is usually in the range of 10  $\mu$ s to 1 s. The reciprocal values  $R_1 = T_1^{-1}$  and  $R_2 = T_2^{-1}$  are called relaxation rates.

### 2.1.1.3 External transverse relaxation $T_2'$

There is an additional dephasing of the transversal magnetization caused by external field inhomogeneities often referred to as  $T_2'$  decay. It is important to note that coherence loss due to inherent fluctuations of the magnetic field environment described by  $T_2$  is random and irreversible whereas external field perturbations are ordered and constant. Given an appropriate pulse sequence such as a spin echo [26], this de-phasing caused by constant external fields can be re-phased. Under the assumption that the local field distribution follows a Lorentzian distribution (which is not the case for

## 2. BASIC PRINCIPLES OF MR GUIDED CELL TRACKING

---

strong magnetized particles discussed next), both transverse dissipative effects can be condensed to the effective transversal relaxation rate:

$$\frac{1}{T_2^*} = \frac{1}{T_2} + \frac{1}{T_2'} \quad (2.3)$$

### 2.1.1.4 Relaxation and imaging contrast

Exploitation of  $T_1$  and  $T_2$  effects provides the basis for tissue identification in MRI. The transversal magnetization  $M_{xy}$ , hence, signal intensity depends on the available amount of longitudinal magnetization  $M_z$  to be flipped into the transversal plane as well as the net (phase coherent) transversal spin ensemble at the time of acquisition. Consequentially tissue signal tends to increase with increasing longitudinal relaxation  $1/T_1$  and decreases with increasing  $1/T_2$  and  $1/T_2^*$ . Pulsesequences that emphasize changes in  $1/T_1$  are referred to in literature as  $T_1$ -weighted and produce a hyperintense contrast for short  $T_1$  specimens. Contrary,  $T_2$ -weighted scans produce hypointense contrast for components with a short  $T_2$  time.

MR contrast agents generally reduce both,  $T_1$  and  $T_2$ , but usually they are classified as  $T_1$  or  $T_2$  agents corresponding to their dominant relaxation mechanism [27]. The efficiency with which the complex enhances proton relaxation rates of water is measured in terms of the relaxivity values  $r_1$  and  $r_2$ . The tissue relaxation rate increase per millimole of agent  $c_{CA}$  is given by the linear relaxivity approximation

$$\frac{1}{T_1} = \frac{1}{T_{10}} + r_1 \cdot c_{CA} \quad \text{and} \quad \frac{1}{T_2} = \frac{1}{T_{20}} + r_2 \cdot c_{CA} \quad (2.4)$$

with  $T_{10}$  and  $T_{20}$  the unenhanced tissue relaxation times. The ratio of  $r_2/r_1$  is used for classification of MR contrast agents.  $T_1$  agents usually have  $r_2/r_1$  ratios in the order of 1 to 2, whereas that value for  $T_2$  agents, such as iron oxide particles, gets as high as 10 or more.

### 2.1.2 Magnetic properties of materials used as MR contrast agents

A compound that is able to influence the relaxation times of water protons has to be paramagnetic [28, 29, 30]. Hence, within this section, a brief overview in magnetic interactions with matter is presented.

If matter is placed in a static magnetic field  $\vec{H}$ , the electrons' orbitals and spin magnetic moments orientate with the applied field. This response is described by the magnetic susceptibility  $\chi$

$$\vec{M} = \chi \vec{H} \quad (2.5)$$

with  $\vec{M}$  the orientated density of magnetic moments of a material or magnetization. For atoms that have unpaired electrons positioned in their outer spin orbitals, the magnetization is non-zero and describes the amplification of the magnetic flux  $\vec{B}$  by introducing the material to the magnetic field

$$\vec{B} = \mu_0 (\vec{H} + \vec{M}) \quad (2.6)$$

where  $\mu_0$  is the permeability of free space. Generally susceptibility is a temperature as well as field dependent parameter defined for paramagnetic substances through the Brillouin equation with  $\hbar$  the Planck constant divided by  $2\pi$ ,  $k_B$  the Boltzmann constant and  $T$  the absolute temperature as

$$\chi = \frac{\hbar\gamma}{2B} \tanh\left(\frac{\hbar\gamma B}{2k_B T}\right) \quad (2.7)$$

and as a consequence, susceptibility induced field inhomogeneity scales with the main magnetic field strength.

### 2.1.2.1 Paramagnetism

Given the above definitions, paramagnetism is described by a positive magnetic susceptibility and zero net resultant magnetization in the absence of an external magnetic field (no remanent magnetization). The large and fluctuating magnetic moments of the unpaired electrons hosted by paramagnetic ions absorb energy from the proton spin system resulting in  $T_1$  and  $T_2$  relaxation first described by Bloembergen and Solomon [28, 29] and later expanded to paramagnetic macromolecules by Gueron [30]. Paramagnetic ions used as MR contrast agents are found in the chemical subset of transition

## 2. BASIC PRINCIPLES OF MR GUIDED CELL TRACKING

---

metals and lanthanides such as for example Gadolinium(III) with seven unpaired electrons or Iron(III) with 5 unpaired electrons. If the solvent (free protons) is brought near a paramagnetic core, relaxation is described by the theory of *inner sphere relaxation* and the interested reader is referred to the work of Solomon and Bloembergen [28, 29].

### 2.1.2.2 Superparamagnetism

Superparamagnetism occurs in materials consisting of large numbers of paramagnetic ions structured to a crystal lattice (as for example in iron oxides of magnetite  $\text{Fe}_3\text{O}_4$ ). Those crystals are smaller than a Weiss domain (<15 nm [31]) which forces all electron magnetic moments to align in the same direction if an external field is applied, resulting in a very high magnetic moment. Electron spins in such crystals interact with each other through spin-coupling. Within such coupled spin systems, there is more than one possible direction of alignment if an external magnetic field is applied. The magnetization over the Weiss domains gets anisotropic, which allows a paramagnetic crystal to have no remanent magnetization. This is due to the energy differences of the alignments (anisotropic or easy axes, e.g. 6 for a crystal of magnetite) which are smaller compared to a spin system with just the parallel and anti-parallel state. Hence if the polarizing field is switched off, the thermal agitation ('shaking') of the crystal is sufficient to relax the total magnetic moment immediately.

### 2.1.3 Iron oxide contrast agents

#### 2.1.3.1 Longitudinal relaxation of superparamagnetic iron oxides

$T_1$  relaxation of superparamagnetic crystals is driven by two mechanisms: The Néel relaxation and the particle rotational relaxation. Both interactions relaxate the protons' excited state through fluctuations of the magnetic field surrounding the particles often denoted as *outer sphere relaxation*. Néel relaxation is a property of anisotropic paramagnetic crystals and describes the orientational flipping of electron spins between the easy axes given by the crystals anisotropy through thermal shaking. It is described by the Néel relaxation time  $\tau_N$  [32]

$$\tau_N = \tau_0 e^{KV/k_B T} \quad (2.8)$$

with  $\tau_0$  a constant depending on spin-orbit coupling,  $K$  the crystals anisotropy constant,  $V$  the crystal volume,  $T$  the absolute temperature and  $k_B$  the Boltzmann constant.  $\tau_N$  is in the order of nanoseconds for small crystals (<10 nm) but can be considerably longer if the crystal enlarges.

The second mechanism, orientational relaxation or Curie relaxation, describes the fact that the crystal is rotating. Hence, fluctuations of its total microscopic magnetic moment are observed and characterized by the rotational correlation time constant  $\tau_R$

$$\tau_R = \frac{4\pi a^3}{3} \cdot \frac{\eta}{k_B T} \quad (2.9)$$

with  $a$  the radius of the particle and  $\eta$  the viscosity of the surrounding matrix. Both factors, the Néel relaxation  $\tau_N$  and the rotational correlation time  $\tau_R$  act together and cause the total fluctuation in re-orientation of the crystals' magnetic moment  $\tau_C$ :

$$1/\tau_C = 1/\tau_N + 1/\tau_R. \quad (2.10)$$

For outer sphere  $T_1$  relaxation, water diffuses through the local magnetic field gradient of the paramagnetic crystal. The interaction is a dipolar coupling between the protons and the magnetic field of the particle which is modulated by  $1/\tau_C$ . Most efficient  $T_1$  relaxation is gained for  $\tau_C \approx 1/(\gamma B_0)$  (in case of a 3 T MRI,  $1/(\gamma B_0) \approx 8$  ns). Therefore, higher relaxivity values  $r_1$  are observed for smaller superparamagnetic particles since they possess a fast Néel relaxation (low anisotropic energy) and high rotational relaxation rates close to the protons larmor frequency. Due to the cooperative behavior of the spins, iron oxides generally have a higher magnetic moment on a per-atom basis compared to single paramagnetic atoms like Gd(III). This results in a significantly higher  $r_1$  relaxation rate (typically 4 - 5 times higher compared to GdDTPA). A smaller crystal core as beneficial for  $r_1$ , has a smaller magnetic moment. Hence, the  $r_2$  relaxation rate is reduced. Therefore, the particles' crystal size determining the anisotropy energy is a crucial parameter for the  $r_2/r_1$  behavior of iron oxide contrast agents. In order to produce contrast agents with high  $r_1$  and  $r_2$  properties, superparamagnetic

## 2. BASIC PRINCIPLES OF MR GUIDED CELL TRACKING

---

iron oxides (SPIO) are commonly made from single iron oxide cores in the range of 4 - 10 nm aggregated to colloids with hydrated diameters of 50 - 100 nm.

### 2.1.3.2 Transverse relaxation caused by condensed paramagnetic structures

Local variations of the magnetic susceptibility cause disturbances of the  $B_0$  field as described in equations 2.5 and 2.6. According to the field dependent Larmor frequency  $f_0 = \gamma B_0$ , the precessional frequency of the spins gets spatially heterogeneous and causes  $T_2'$  decay.

The heterogeneities can be classified based on their spatial extent into the macroscopic and mesoscopic scale. The macroscopic scale is related to large-scale bulk magnetic susceptibility shifts of air-tissue interfaces or imperfect  $B_0$  shimming commonly much larger than the voxel size. The mesoscopic scale, on the other hand, comprises an intermediate scale, larger than the atomic and molecular distances, but smaller than voxel dimensions. It is the mesoscopic scale which gives rise to the tissue specific property of  $T_2'$ . In addition to the frequency spread which causes different spin phases surrounding an SPIO, the presence of molecular diffusion has an influence on the apparent  $R_2'$  rate. For a well known field distribution, the effect of diffusion on the apparent transversal magnetization within a heterogeneous environment can be described by the Bloch-Torrey equation [33]

$$\frac{\vec{M}}{dt} = \gamma \vec{M} \times \vec{B} + D \cdot \Delta \vec{M} \quad (2.11)$$

with  $D$  the self-diffusion coefficient of water in the order of 1 - 2.5  $\mu\text{m}^2/\text{ms}$  [34, 35] and  $\Delta$  the Laplace operator. However, since the intra-voxel field distribution is commonly unknown, a phenomenological description of the apparent  $T_2'$  contrast was first developed by Gillis and Koenig [36] commonly known as *Motional Narrowing*. It was further extended by Yablonskiy and Haacke [34, 37] for structures with very high paramagnetic moments known as *Static Dephasing Regime*. Among other tissue types, Yablonskiy and Haacke applied their theory on red blood cells by modeling them as paramagnetic spheres. Considering the paramagnetic property of deoxygenated hemoglobin within red blood cells, these cells are comparable to cells labeled with superparamagnetic iron oxides. Bowen et al. [35] first showed the application of the the *Static Dephasing*

*Regime* to iron oxide labeled cells which is nowadays the gold standard in quantitative cell tracking with MRI.

**Motional Narrowing Regime** If the water molecules' position is thought to be fixed over time, a spin refocusing pulse is able to reverse the phase dispersion caused by static heterogeneous magnetic fields. However, if Brownian motion is present, molecules interchange their positions, and hence, change their precessional frequency over time resulting in a reduced phase dispersion than expected for a static, motionless, spin ensemble. This behavior is commonly known as motional narrowing [36]. A consequential result is that refocusing with a  $\pi$ -RF pulse cannot resolve the accumulated phases. Hence, a  $T_2'$  driven signal decay is observed even for spin echo sequences. The motional narrowing regime is valid for

$$\delta\omega \cdot \tau_D \ll 1 \tag{2.12}$$

with  $\delta\omega$  the frequency offset at the equator of a field-generating particle and  $\tau_D$  the characteristic diffusional time.  $\tau_D$  is defined as the time, necessary for water to diffuse a distance comparable with the field-generating objects radius  $R$  and is calculated as [36]

$$\tau_D = R^2/D. \tag{2.13}$$

**Static Dephasing Regime** The major assumption of the static dephasing regime is that NMR signal dephasing due to susceptibility induced inhomogeneities should occur before molecular diffusion averages out the phase coherence given by the RF-excitation [37]. Within that regime, diffusion effects become unimportant if

$$\delta\omega \cdot \tau_D \gg 1 \tag{2.14}$$

is valid. In literature, this relaxation regime is sometimes known as the slow motion regime. Instead of dealing with a reduced diffusional time, the static dephasing regime is given by paramagnetic structures with a critical susceptibility and/or size. The model of

## 2. BASIC PRINCIPLES OF MR GUIDED CELL TRACKING

---

Yablonskiy and Haacke [34]<sup>1</sup> is based on a compartment of paramagnetic material with a magnetic susceptibility of  $\chi_c$  and surrounding tissue of magnetic susceptibility  $\chi_0$ . The magnetic subsystem occupies a total volume fraction of  $f_v$  and has a susceptibility difference to the major tissue compartment of

$$\Delta\chi = \chi_c - \chi_0. \quad (2.15)$$

The field distribution  $\omega_n(\vec{r})$  caused by one paramagnetically loaded cell of radius  $R_n$  is

$$\omega_n(\vec{r}) = \delta\omega_c \left(\frac{R_n}{r}\right)^3 (3 \cos^2 \Theta - 1) \quad (2.16)$$

with  $\Theta$  the angle between the direction of the polarizing field and vector  $\vec{r}$ , and  $\delta\omega_c$  the characteristic equatorial field offset of

$$\delta\omega_c = \frac{\gamma \cdot B_0}{3} \Delta\chi. \quad (2.17)$$

Given the above definitions and a known distribution of the single cells of volume  $v_n$  dispersed in the total volume  $V$ , the NMR signal is calculated as

$$S(t) = \rho \cdot (1 - f_v) \prod_{n=1}^N \frac{1}{V - v_n} \cdot \int_{V-v_n} e^{-i \cdot \omega_n(\vec{r}) \cdot t}. \quad (2.18)$$

Haacke and Yablonskiy [34] showed that for a cellular volume fraction  $f_v \ll 1$ , the resulting signal depends only on the volume fraction, but not on the underlying distribution of the cells. For

$$R_c^2 \gg \frac{6D}{\delta\omega_c \cdot f_v^{1/3}} \quad (2.19)$$

which is an adopted form of their equation 2.14 for a dilution of paramagnetic spheres

---

<sup>1</sup>Until the end of this section equations are converted from cgs into SI units. In order to be comparable with literature, especially with the static dephasing regime applied to iron oxide labeled cells published by Bowen et al. [35], magnetic flux  $B_0$  of the polarizing field and the magnetization are given in units of mG =  $1 \cdot 10^{-7}$ T and the gyromagnetic ratio is defined as  $\gamma = 26.752 \text{ rad mG}^{-1} \text{ s}^{-1}$ .

## 2.1 Contrasts for cellular imaging

---

with an average radius of  $R_c$ , they predicted that the magnitude within a specified time frame (normally the echo time, TE, of the sequence) can be described by a single exponential of the form

$$|S(t)| = |S(0)| \cdot e^{-R2' \cdot t} \quad (2.20)$$

with the relaxation rate  $R2'$

$$R2' = \gamma \frac{2\pi}{9\sqrt{3}} \cdot LMD \quad (2.21)$$

or

$$R2' = \gamma \cdot K_{fsl} \cdot LMD \quad (2.22)$$

with  $K_{fsl} = 0.403$  the gradient echo specific fractional signal loss to iron loaded cells and  $LMD$  the local magnetic dose as defined by Yablonski and Haacke

$$LMD = f_v \cdot M_c \quad (2.23)$$

with  $M_c$  the magnetization (magnetic moment/volume) of the paramagnetic particles.

### 2.2 Cell labeling and contrast agent quantification

#### 2.2.1 Contrast agents used for cellular labeling

Within the recent years, many MR contrast agents have been evaluated for cellular imaging based on the key requirements: labeling efficiency, biocompatibility and high relaxivity. They consist of paramagnetic iron oxides, MR reporter genes expressing (metallo-) proteins or simple chelators containing a single paramagnetic ion.

Augmenting cellular contrast by internalization of paramagnetic ions like Gd(III) appeared to be the method of choice encouraged by the widely spread applications of Gd contrast enhanced MRI in sensing tumor diseases. However, the relaxivity values of gadolinium chelates ranging from 3 to 8 mM<sup>-1</sup>s<sup>-1</sup> for both  $r_1$  and  $r_2$  [38, 39] are generally not high enough to visualize small numbers of cells. The common approach to increase detectability of Gd(III) labeled cells is to increase the cellular agent concentration [40]. Ahrens et al. [41] found in a tissue contrast model that if  $\mu\text{m}$  resolutions allow for single cell imaging, a detectable image contrast of a single cell is produced if 4 - 5 · 10<sup>7</sup> Gd-complexes are internalized. On the contrary the intracellular dosage should be minimized since long term studies on biocompatibility are not available [42]. The design rationale of current FDA approved lanthanide contrast agents implies a rapid and substantial clearance to prevent depositions and dissociated free metal ions within organs [43]. A rationale, which can not be guaranteed, even contraindicates the goal in cell tracking which is to follow the cells fate over the cells entire life cycle.

Next to gadolinium, manganese is the second most sensitive  $T_1$  contrast label based on a single paramagnetic iron. As manganese salt ( $MnCl_2$ ) efficient cell labeling was demonstrated in vitro on lymphocytes [44] and in an oxidated form of manganese ( $MnO$ ), first reports on in vivo cell imaging were reported on a glioma cell line in rats [45]. As observed for Gd(III) chelates, the sensitivity issue hinders the detection of single labeled cells, and a dosage dependent toxicity was observed for both, the  $MnCl_2$  and the  $MnO$  label.

MR reporter genes are promising candidates for longitudinal imaging of cell populations without the use of exogenous contrast agents within the cells. These reporter genes express either an enzyme/protein product or receptor that alters the  $T_1/T_2$  properties in the cells' vicinity [46, 47, 48, 49]. If the introduced reporter gene expression is stable, the labeled cell can be observed over the entire lifetime. As the reporter gene is usually

## 2.2 Cell labeling and contrast agent quantification

---

passed on to its progeny cells, it is possible to image expanding cell populations longitudinally. Reporter genes can alter longitudinal relaxivity by transcription of enzymes which bind to extracellular gadolinium chelates to change the rotational correlation time resulting in a manyfold higher  $r_1$  relaxivity [50, 51]. Another approach is to enhance the expression of the transferrin receptor (TfR) on the cellular membrane which internalizes iron loaded transferrin proteins leading to a fast iron accumulation within the cell, resulting in a shorter  $T_2'$  value. Early studies showed that within modified fibroblasts the iron uptake was threefold higher compared to non-transfected controls [52]. Further progress in the investigations on metalloproteins showed that ferritin, a metalloprotein able to store up to 4,000 Fe atoms [46], can be structurally adopted to enhance the proteins magnetic moment to the range of ultrasmall (U)SPIOs [53, 54, 55]. However, compared to chelated Gd(III), the relaxation enhancement through reporter genes is fairly low, and large populations of genetically modified cells are needed in order to gain a reasonable change in image contrast. Other limitations are gene silencing owing to DNA methylation or histone modification which affects transcription and can suppresses the reporter signal [46], and the strict evaluations such genetic modifications have to undergo in order to avoid objectionable cell behavior.

Given the aforementioned aspects on detectability and biocompatibility, cell internalized iron oxides dominate the field of cell tracking because of their following advantages [56]:

- Most signal change per unit of metal
- Their size can be adopted to allow for higher relaxation rates and/or optimal labeling properties
- Enhanced biocompatibility and biodegradability compared to lanthanide based agents
- Their coating can be used for linkage to targeting ligands
- They can be detected by optical and electron microscopy

Despite their dominant (hypointense)  $T_2'$  contrast, leading to a signal reduction rather than amplification, they allowed for the detection of single labeled cells in the first place [57, 58]. FDA approved iron oxides like Feridex (AMAG Pharmaceuticals, Inc.) and Resovist (Bayer HealthCare Pharmaceuticals Inc.) facilitate a fast transition of preclinical results into clinical practice [12] and motivated the present work to focus on superparamagnetic iron oxides.

## 2. BASIC PRINCIPLES OF MR GUIDED CELL TRACKING

---

### 2.2.2 Cell labeling

The process of active incorporation of a label when cells are cultured in vitro is referred to as *cell labeling*. Cellular labeling can be direct (non-specific) or receptor mediated (specific). Within this work the focus is on direct labeling methods since in most progenitor cell lines specific surface antigens (e.g. for internalizing monoclonal antibodies) for receptor mediated techniques are missing [59].

Direct labeling is a simple and quite straight-forward approach. A cell population is labeled by incubating a confluent monolayer of cells with the contrast agent of interest. After a certain incubation time, the non-incorporated extracellular contrast agent is removed by washing the culture dish with phosphate-buffered saline (PBS) and the labeled cells are harvested by adding trypsin.

Several aspects modulate the cellular uptake of exogeneous contrast agents. If a cell is phagocytotically active, such as for example cells of the immune system like macrophages, T-cells and monocytes, contrast agents are taken up directly through phagocytosis. For other cell types, such as stem and progenitor cells, the path of endocytosis is commonly used as an cellular uptake mechanism. Endocytosis is the absorbance of large molecules (e.g. proteins) from the extracellular space which cannot pass the cell membrane directly. The molecules are entrapped into vesicles coated by a lipid-layer, comparable to the cellular membrane. Endosomal uptake can be initiated by molecules with ligands causing receptor-mediated endocytosis. For non-receptor driven endocytosis, the size of a particle determines its uptake efficiency. As a consequence, nano-particles with mean hydrated diameters of  $<50$  nm are hardly taken up by most of the non-phagocytic cells. Whereas a number of sites reported efficient direct uptake of micrometer-sized iron oxides for stem and progenitor cells [60, 61], efficient uptake of nanometer-sized iron oxides is still a topic under investigation. Several studies indicated that intra-cellular labeling efficiency for USPIOs (mean hydrated diameters of  $\leq 30$  nm) is very limited compared to their larger counterparts, SPIOs, with diameters ranging between 50 to 150 nm [62, 63]. Since smaller iron oxides with a reduced  $r_2/r_1$  ratio are promised to give a high  $r_1$  relaxivity with moderate  $T_2'$  dispersion, they are very attractive for hyperintense  $T_1$ -weighted cellular imaging. Given this motivation, several strategies have been developed to amplify their uptake into cells [59, 64]. The aim of these approaches is to support the contrast agent passage from extracellular

## 2.2 Cell labeling and contrast agent quantification

---

space to cytoplasm through the cellular membrane.

The double lipid layer of the cell membrane is a mechanical as well as an electrical barrier. The electrical charge of the membrane, important for the cells' exchange mechanisms with the environment, hinders contrast agent entrapment if the particles are equally charged, or may guide contrast agent uptake if the agent possesses a shell charged with opposite polarity. FDA-approved iron oxides are coated by dextran or carboxy-dextran, polysaccharides made of many glucose molecules, which charge the particles' surface to prevent nanoparticle aggregation. Although their electrical behavior does not significantly alter cellular uptake, dextran coatings present a platform to bind *transfection agents* consisting of highly charged macromolecules to aid the formation of endosomes on the anionic cellular membrane [65, 66]. Widely used transfection agents are polyamine (poly-L-lysine, PLL) and protamine-sulfate (PS). These transfection agents are toxic at higher concentrations, and only protamine-sulfate is clinically approved as an antidote to heparin overdose [67]. The transfection agents and contrast agents assemble via electrostatic interactions. Every (U)SPIO and transfection agent combination has to be optimized carefully. Lower concentrations lead to insufficient uptake of particles, whereas higher concentrations may result in an enhanced production of reactive oxygen species and, hence be toxic to the cells [66].

Another approach to efficient (U)SPIO labeling is by *electroporation* (EP). Pulsed voltages are used in order to induce electrochemical permeability changes in cell membranes which lead to an enhanced endosomal activity [64, 68]. A direct comparison of EP and the transfection agents PLL and PS on embryonic stem cell lines showed that EP reduced the differentiation capability of the investigated cells, and an improved uptake of SPIOs was reported with protamine-sulfate [69].

*Liposomes*, artificially generated nanocarriers (size 200 - 1000 nm) composed of a double-lipid layer, might be used to entrap contrast agents [70, 71, 72, 73] to transfect the cellular membrane. Their cationic shell and enlarged size improve endosomal uptake at minimum cytotoxicity [74]. Liposomes have already been analyzed as transfection agents for SPIO labeling of pancreatic islet cells without affecting the function or viability of the cells [75], and high concentrations of SPIOs entrapped into micrometer-sized liposomes allowed for single cell imaging of fish embryos [76]. Their uptake efficiency is further improved by using transactivating transcriptional activator (Tat) peptides [77]

## 2. BASIC PRINCIPLES OF MR GUIDED CELL TRACKING

---

bound to their outer surface, resulting in excellent labeling properties for nonphagocytic progenitors [78].

### 2.2.2.1 Cellular labeling and contrast agent efficiency

Endosomal uptake of contrast agents is accompanied by very desirable properties for  $T_2'$  weighted imaging but is a major problem if  $T_1$  is to be exploited. For the transversal relaxation, cellular endosomes act as a secondary contrast agent. Compartmentalization of the agent within confined endosomal vesicles leads to an enhanced magnetization, producing a heterogeneous mesoscopic field perturbation largely exceeding the cell. As a result, a vast pool of protons is affected by the cell extending heterogeneous field and relaxation can be described by the static dephasing regime.

For  $T_1$  relaxation on the other hand, protons need to be in the microscopic environment of the paramagnetic molecule in order to relaxate by inner sphere and outer sphere mechanisms. The exchange rate between free water and the paramagnetic core determines the apparent  $r_1$  relaxivity [79]. In the case of endosomally entrapped agents, the water exchange rate of the free pool of protons (outside the cell) to the paramagnetic compound is restricted by the cellular membrane and, additionally by the membrane of the endosomal vesicles. Terreno et al. [80] investigated the relaxivity differences of  $T_1$  contrast agents (Gd-HPDO3A) internalized directly into the cytoplasm (through electroporation) and by endocytosis into small vesicles. They reported an upper limit of the relaxation enhancement for the vesicle internalized particles which was not observed for Gd-complexes internalized within the cytoplasm only. This "quenching" is caused by the restricted water diffusion between the cytosol and the vesicles, thus explaining the inefficiency of endosomal internalized  $T_1$  contrast agents observed in many studies [81, 82, 83].

Another inherent limitation of the direct labeling method is that the label dilutes during cell division, resulting in a decreased amount of label per cell with time. It was reported that in rapidly dividing cells, intracellular iron disappeared by five to eight cell divisions [66]. In addition, the label can be distributed asymmetrically to progeny cells or the label can even get lost and taken up by phagocytic cells, which greatly reduces contrast specificity.

Sensing magnetically labeled stem and progenitor cells in vivo bears the jeopardy of false positive interpretation of the label-induced hypointensities to originate from the

## 2.2 Cell labeling and contrast agent quantification

---

targeted cells. Some studies showed that macrophages engulfing non-viable labeled cells produce the same MRI signal and can not be distinguished from their therapeutic counterparts [84, 85, 86, 87]. Therefore, co-labeling of magnetically labeled cells with a fluorescent dye and faithful histological investigations in preclinical trials are crucial to prevent misinterpretations.

### 2.2.2.2 Biocompatibility of MR contrast agents

The cellular incorporation of Gd-complexes, even if densely packed into long-term stable macrocyclic chelators such as DOTA or DO3A, implies the risk of losing the toxic Gd ion. Even if the chelator stays stable, there is a risk of transmetallation [88] where the toxic lanthanide ion is exchanged with other endogenous metals (most relevant is  $Zn^{2+}$ ) and released from the chelator. Nephrogenic systemic fibrosis (NSF), a pathologic proliferation of fibrocytes of the skin, has already been reported to be linked to the administration of Gd-chelates in patients with renal dysfunction [89, 90]. High levels of Gd-induced intracellular reactive oxygen species (ROS) lead to mitochondrial dysfunction [91] and toxic effects on the central nervous system [92, 93]. Therefore, using Gd-chelates for therapeutic stem cell therapies is highly questionable.

SPIO nanoparticles coated by dextran or carboxy-dextran are Food and Drug Administration (FDA)- approved for the use in liver (hepatic) imaging (with hydrated diameters of  $\approx 60$  nm) and under the label ultrasmall (U)SPIOs as a blood pool agent with diameters of about  $\approx 10$  nm. Following the ingestion of SPIO into endosomal vesicles, the SPIO coat is degraded by lysosomes and iron is metabolized as a hemoglobin component [56, 94, 95]. Despite iron being in principle biodegradable, an SPIO core consists of thousands of iron atoms which lead to a 10-fold enhanced intracellular iron concentration [82]. High concentration levels of intracellular Fe are known to be harmful by catalyzing the generation of ROS by a reaction of hydrogen peroxide (Fenton reaction) [96, 97]. As a result, increased apoptosis and DNA fragmentation had been reported [98, 99] at very high iron deposits. However, at iron concentrations applicable for magnetical labeling of cells, long-term viability, growth rate and apoptotic indexes were reported to be unaffected [66].

Concerning highly magnetized cells, the question remains if the cellular biodistribution is effected during the MR scan. Wilhelm et al. [100, 101] reported endosomal deformations caused by the interaction of the endosomes' magnetization with the main

## 2. BASIC PRINCIPLES OF MR GUIDED CELL TRACKING

---

static magnetic field. This effect is thought to be minor since it is limited to the time of MR-investigation. However, the question about cellular function during that time period is still an open one.

### 2.2.3 Quantification of cellular iron label

#### 2.2.3.1 Transmission electron microscopy

The analysis of transmission electron microscopic (TEM) images allows for the documentation of existence of intra-cellular iron and its distribution within the cell. From these images, important insight into the incorporation (cytoplasmatic or vesicular) and the apparent agglomeration of nanoparticles can be gained. However, TEM images do not allow for quantitative analysis of total cellular iron uptake. Furthermore, at TEM imaging, snapshots of single individual cells are taken, and therefore, assumptions based on the images have limited validity for the total cell population.

The labeled cells have to be prepared in a standardized four-step procedure prior to TEM visualization. First, the cells are suspended in agarose gel and dehydrated with alcohol propylene oxide. A fixation step follows where the dried pellet is infiltrated with epon and hardened over 48 hours. Third, the sample is sectioned by a microtome and finally, a negative staining is performed with uranyl acetate and lead citrate. Examples of TEM images acquired of uranyl stained mesenchymal stem cells labeled with superparamagnetic iron oxides are given in figure 2.1. Figure 2.1a shows the process of endosomal uptake of the contrast agent (arrow). These endosomes transport the nano-particles into the cytoplasm. Figure 2.1b&c give insight into the clustering of the 60 nm particles entrapped into  $\approx 1 \mu\text{m}$  sized endosomal vesicles (yellow selection).

#### 2.2.3.2 ICP-MS & AAS

*Inductively coupled plasma mass spectroscopy* (ICP-MS) is the most sensitive technique in measuring the total iron content for low iron concentrations of pgFe/cell reached with common labeling techniques. The sample is ionized at a temperature of 10,000 K by a plasma of inductively heated argon gas. The sample plasma is then further analyzed by a mass-spectrometer separating ions by their mass-to-charge ratio. The total iron content is measured regardless of the oxidation state or the molecular structure. Hence, no information on the actual magnetization of the iron label/cell is given [102].

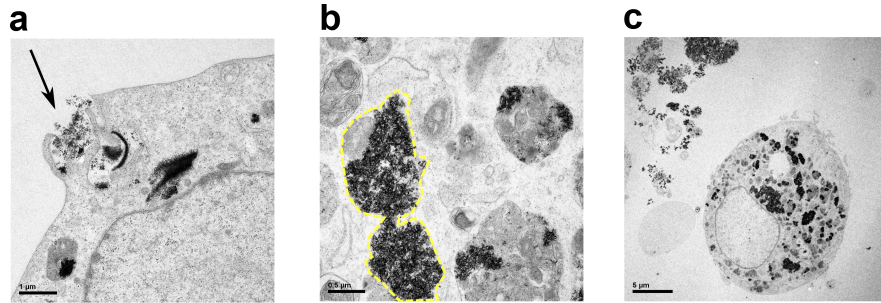


**Figure 2.1:** Transmission electron microscopy of iron oxide labeled mesenchymal stromal cells. The dark strands are an SPIO with mean hydrated diameter of  $\approx 60$  nm in size. **a** is a snapshot of the endosomal uptake process on the cellular membrane (arrow). **b** gives insight to the endosomal vesicle size of  $\approx 0.5$ - $1 \mu\text{m}$  diameter. **c** is a representative image showing the distribution of SPIO labeled endosomes within the cell cytoplasm.

Another technique called *atomic absorption spectroscopy* (AAS) assesses an optical absorption measurement on the atomized sample. The absorption (difference in radiation flux with/without the sample) is analyzed by burning the sample with a flame of air-acetylene (F-AAS) or electrothermally (EL-AAS) at about 2,500 K. It relies on given standards to gain absolute values of the final iron content.

Despite the fast and accurate measurements ICP-MS and AAS provide, they are often not available in a standard laboratory setup. Hence, measurements have to be carried out by core facilities, making these techniques more time consuming and cost-intensive.

### 2.2.3.3 Histochemical detection of iron

Under a standard laboratory setup, cellular iron uptake can be investigated by either Prussian blue staining and optical validation or by spectrophotometric detection of ferrozine (colorimetric ferrozine-based assay).

*Prussian blue* is a pigment formed by ferrocyanide bound to any ferric ion (Fe(III)) present resulting in a blue-green color visible under the microscope. In order to get ferrocyanide into the cell, the cellular membrane is first dispersed by hydrochloric acid. The method is very sensitive to small amounts of ferric ion although no quantitative iron information can be acquired. Prussian blue staining is known to be one of the most sensitive stain in histology used as a visualization of free iron within the cells cytoplasm.

## 2. BASIC PRINCIPLES OF MR GUIDED CELL TRACKING

---

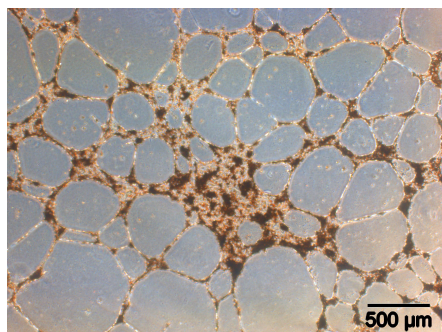


**Figure 2.2:** Microscopy of Prussian blue stained EPC network.

The *ferrozine-based assay* [103, 104] is a colorimetric test which allows to quantify iron in ferric and ferrous (Fe(II)) form. It is based on ferrozine, a chelator of ferrous iron which absorbs light at a wavelength of 550 nm [103]. Hydrochloric acid is used in order to dissolve the entrapped iron and reduce ferric to ferrous iron. Subsequently, an absorbance measurement is performed and a comparison to a standard calibration line of known iron content gives information on the total amount of cellular iron. Riemer et al. [103] reported that the numbers of total iron content within cells of the ferrozine-based assay equals the numbers acquired by the AAS technique. However, the detection limit of iron in the final solution is 3  $\mu\text{g}/\text{ml}$  [104].

### 2.2.3.4 Susceptometry

The aforementioned quantitative methods (excluding TEM) do not give any insights on the apparent physiochemical structure and distribution of the iron deposition. As addressed earlier, the MR relaxation properties of iron oxides depend on their crystalline structure and their compartmentalization within the cells. Therefore, susceptometric measurements are needed to exploit further the magnetic properties of the labeled cells. Susceptometry measures the magnetization of a suspension of cells at a given field strength. This property appears in theoretical treatments of susceptibility-induced NMR signal response and allows for an estimate of the apparent relaxation rate  $R_2$  given a certain density of the labeled cells [35]. The magnetic moment of a single iron oxide core is known to be saturated at fields larger than 1T [105, 106]. However, at high concentrations of paramagnetic iron oxides, the actual magnetization enlarges due to the cooperative behavior of their magnetic moments with the main magnetic

## 2.2 Cell labeling and contrast agent quantification

---

field, yielding a field dependency which is not described by quantum solutions [35]. Investigations on the relaxation rates of iron oxides in aqueous solution for different field strengths indicate that their  $r_2$  values scale linearly with the field above 1T [107]. It is expected that cooperative effects of iron oxides confined within cells rather than uniformly suspended further enhance their total magnetic moment [35]. Therefore, measuring the actual susceptibility of the labeled cell suspension at the exact MR fieldstrength is mandatory to give estimates of the impact on their MR contrast.

**Measuring cellular iron load through MR susceptometry** Since this method was used throughout the presented work to determine cellular iron deposition after labeling, a more detailed description follows.

The global magnetic susceptibility of a sample is often termed bulk magnetic susceptibility or BMS. The BMS can be measured directly (at the MR relevant fieldstrength) by measuring the NMR frequency shift within the sample under investigation at different positioning of the sample to the polarizing field  $B_0$ . This method, often referred to as the Reilly-McConnell-Meisenheimer (RRM) method [108], is based on the change of the magnetic flux within a non spherical sample of known geometric shape at different sample orientations relative to the main magnetic field. The magnetic susceptibility for an observed frequency shift given a known geometric shape can be calculated with the formulas given in Chu et al. [109]. This method is somewhat cumbersome for measuring the BMS of iron oxide labeled cell suspensions since high iron payloads result in a fast  $T_2'$  decay which precludes exact spectroscopic measurements within the sample. Bowen et al. [35] introduced a susceptometric measurement based on a multi-echo gradient echo technique which measures the BMS value on the basis of the field heterogeneity pattern outside the sample. Given an ideal nonfinite cylinder containing the sample to be measured (e.g. the cellular suspension), orientated orthogonally to the main magnetic field  $B_0$ , the frequency offset  $\Delta f$  outside that cylinder is given by the equation

$$\Delta f(r) = \frac{\gamma B_0 R^2 \cos(2\Theta)}{r^2} \left[ -\frac{1}{2} \left( 1 + \frac{\chi_1}{3} \right) (\chi_0 - \chi_1) \right] \quad (2.24)$$

where  $\chi_0$  is the magnetic susceptibility of the outer medium e.g. agarose gel with a known value of  $\chi_0 \approx -9.06 \cdot 10^{-6}$  ppm and  $\chi_1$  the unknown BMS. The frequency offset

## 2. BASIC PRINCIPLES OF MR GUIDED CELL TRACKING

---

is measured at a distance from the center of the cylinder  $r$  with  $R$  the outer radius of the infinite cylinder and  $r \geq R$ .  $\Theta$  is the angle between the main magnetic field  $B_0$  and the vector to the position of interest at a distance  $r$ . The frequency shift is measured through a multi-echo gradient echo train where the complex-valued signal intensity of the images in dependence of the echo-time TE is

$$S(\text{TE}) = S_0 e^{\text{TE}(-1/T_2^* + j2\pi\Delta f)}. \quad (2.25)$$

A Fourier transform of the acquired multi echo images over TE results in spectroscopic information for each image voxel. The so gained voxel-wise NMR spectra have a maximum peak value at the voxel off-center frequency shift  $\Delta f$ . The BMS is fitted from  $\Delta f$  in Eq. 2.24 over the radial distance  $r$  at four different angles  $\Theta$  ( $\Theta = 0/\pi/2/\pi/3\pi/2$ ). An example of the procedure is sketched in figure 2.3. The phantom for the susceptometric measurement consists of a 7 cm diameter 1% agarose sphere wherein the cylindrical cell sample has been cast in. A spherical background phantom is chosen in order to avoid global susceptibility induced frequency shifts. The preparation is performed as follows: First, a 7 cm diameter half shell made of polycarbonate is filled with a 1% agarose gel. During the gel's liquid phase, cylindrical stamps of 3.5 mm in diameter and 3 cm in length are immersed into the gel. After the gel has polymerized, the stamps are removed in order to provide small cylindrical cavities for subsequently placing the labeled cells (again mixed with 1% agarose) at known cellular densities. After fitting on the second polycarbonate half-shell to the bottom part, the upper half of the sphere is filled again with 1% agarose. The whole procedure results in  $\varnothing 3.5$  mm cylindrical cell samples with a length of at least 2.5 cm. Since the sample lengths are longer than 5 times their cylindric diameter, the magnetic field pattern of an infinite cylinder as in Eq.2.24 is assumed. Because residual global inhomogeneities of the  $B_0$  field modulate the resultant susceptometric results, the BMS  $\chi_1$  is gained through averaging the results evaluated at the four different angles  $\Theta$ .

With known BMS, Bowen et al. [35] showed that based on the theory of the static dephasing regime the cellular iron concentration can be estimated by

$$m_c = \frac{LMD}{K_{Fe}n_c} \quad (2.26)$$

## 2.2 Cell labeling and contrast agent quantification

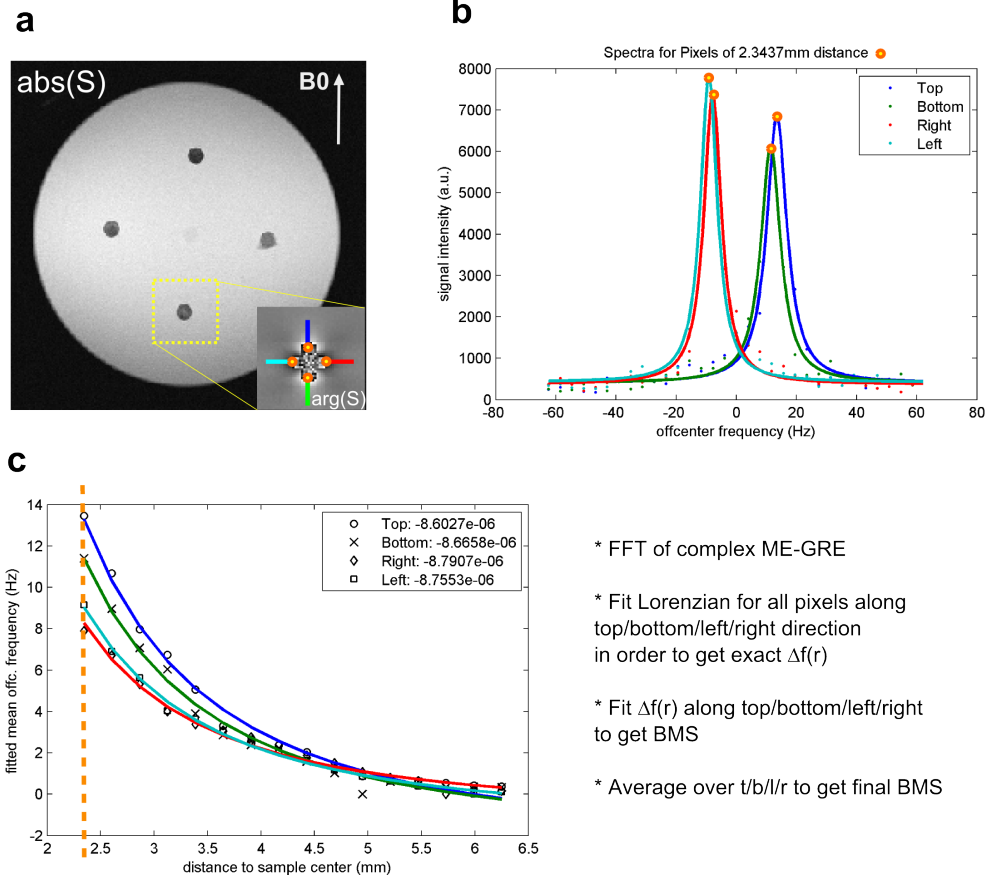


**Figure 2.3:** Susceptometric measurement of cellular BMS based on multi echo gradient echo images. **a:** Magnitude image of the measurement phantom. The detail shows the corresponding phase image. **b:** A fast Fourier transform of the complex multi echo images results in a frequency spectrum for each image voxel. The spectra are evaluated for their off-center frequency at the maximum peak value which corresponds to the mean voxel off-resonance. The frequency offsets along the blue, red, green and cyan lines in (a) are plotted in c. These functions are fitted to equation 2.24 to calculate the bulk magnetic susceptibility  $\chi_1$ .

## 2. BASIC PRINCIPLES OF MR GUIDED CELL TRACKING

---

with  $K_{Fe}$  a calibration coefficient of  $K_{Fe} = 1.34 \cdot 10^{-3}$  mG/(pg/mm<sup>3</sup>) connecting cellular iron load to the effective magnetization (local magnetic dose LMD [34] in mG), the average cellular iron load  $m_c$  in pg and  $n_c$  the cellular density in 1/mm<sup>3</sup>. LMD is calculated from the BMS as

$$LMD = (BMS - \chi_0) B_0 \quad (2.27)$$

with  $B_0$  in mG.

### 2.3 Acquisition strategies for cell tracking with MRI

The high relaxation rates of iron oxide based CAs are thought to be the key to MRI guided cellular imaging in the near future [56]. The following review on acquisition methods towards cell tracking focuses on this very promising class of imaging agents and the possible contrasts they provide.

Ex vivo labeling of cells with paramagnetic iron oxides allows for in vivo tracking with MRI employing mainly the magnetic field perturbations produced by the intra-cellular SPIO. The occurring  $B_0$  inhomogeneities are much larger than the actual cellular size and, with sufficiently high intra-cellular concentrations of iron oxides, even exceed the cell containing image voxel.

A consequence of the heterogeneous  $B_0$  field is a signal degradation in gradient recalled echo (GRE) [35] as well as in balanced steady state free precession (bSSFP) [110] sequences. While in the past years both methods have been successfully applied for cell tracking, their in vivo application bears a profound challenge. Several studies identified two major requirements for in vivo single cell detection. First, high spatial imaging resolutions in the range of  $(100 - 200 \mu\text{m})^3$  are required while echo times should be kept short in order to gain high background signal [11, 61, 111, 112]. Second, a high intra-cellular iron payload is mandatory in order to reach a sufficient level of signal degradation [102, 113].

The following sections present an overview on standard negative contrast techniques based on spoiled gradient echo and fully balanced steady state acquisitions. These techniques are available for all vendors and through all fieldstrengths, their contrast behavior is well described, and their imaging contrast, despite the inherent dark representation of the cells, can be comfortably optimized.

#### 2.3.1 Gradient Echo Sequences

Gradient echo pulse sequences, sometimes termed *gradient refocused echo* or *field echo* acquire the free induction decay by de- and re-phasing of the frequency encoding readout gradient. After a small portion of the longitudinal magnetization  $M_0$  was tilted to the transversal plane, the resultant transversal component  $M_{xy}$  is acquired at the echo time TE. The duration and amplitude of the excitation pulse define the actual flip angle  $\alpha$

## 2. BASIC PRINCIPLES OF MR GUIDED CELL TRACKING

---

and therefore the fraction of transversal magnetization. The transversal component acquired at TE can be described as

$$M_{xy} = M_0 \sin(\alpha) e^{i(\Delta\omega TE + \Phi)} e^{-TE/T_2}. \quad (2.28)$$

$\Delta\omega = 2\pi\Delta f$  is the precessional frequency offset of magnetization and  $\Phi$  a constant phase angle connecting the excitation phase to the received signal. If a train of excitation pulses is applied, the amount of available longitudinal magnetization is reduced depending on the time interval between the RF-pulses, the repetition time TR, and the longitudinal relaxation time constant  $T_1$  of the tissue of interest. After a sufficient number of excitation pulses, the longitudinal component of the thermal equilibrium  $M_0$  is reduced to a steady state value  $M_z$ . For small tip angles  $\alpha$ , the produced transverse magnetization  $M_{xy}$  is much bigger than the longitudinal component spent (because of  $\sin(\alpha)$  in Eq.2.28). Additionally, by reducing the flip angle  $\alpha$ , the time period for a full longitudinal recovery is remarkably shortened resulting in a higher steady state component  $M_z$ . GRE with small tip angles are meaningfully named *Fast Low-Angle Shot* (FLASH) [114] and are frequently used for fast  $T_1$ - and  $T_2^*$ -weighted imaging. The repetition time is often much shorter than the transversal decay time  $T_2$  and hence, transversal magnetization is left at the end of TR. For FLASH sequences, this residual  $M_{xy}$  is destroyed (spoiled) and the resultant signal of the steady state is described as

$$M_{xy} = M_0 \sin(\alpha) \left[ \frac{1 - E_1}{1 - E_1 \cos(\alpha)} \right] e^{i(\Delta\omega TE + \Phi)} e^{-TE/T_2} \quad (2.29)$$

with

$$E_1 = e^{-TR/T_1}. \quad (2.30)$$

If background  $T_1$  is known, the excitation angle can be chosen in order to give maximum background signal at

$$\alpha_E = \arccos(e^{-TR/T_1}). \quad (2.31)$$

This angle is the solution of Eq. 2.29 for  $\frac{dM_{xy}}{d\alpha} \stackrel{!}{=} 0$  and  $\frac{d^2M_{xy}}{d\alpha^2} \stackrel{!}{>} 0$  and is called the *Ernst angle*.

### 2.3.1.1 $T_2^*$ contrast of GRE acquisitions

The phase term in Eq. 2.29 causes a magnitude signal degradation if many different spin isochromats (off-resonances  $\Delta\omega$ ) are confined within a voxel. A voxel containing magnetically labeled cells owes a huge fraction of off-resonant spins, resulting in a de-phasing, and hence, hypointense voxel signal. A phenomenologic description of the decrease in magnitude caused by intra-voxel de-phasing is presented within the theory of the *static dephasing regime* as presented in section 2.1.3.2. The static dephasing regime introduces an exponential decay rate  $T_2'$  (Eq. 2.20) which accounts for intra-voxel field heterogeneities

$$M_{xy\text{Voxel}} = M_0 \sin(\alpha) \left[ \frac{1 - E_1}{1 - E_1 \cos(\alpha)} \right] e^{i(\Delta\omega_0 TE + \Phi)} e^{-TE/T_2} e^{-TE/T_2'} \quad (2.32)$$

where  $\Delta\omega_0$  describes an global  $B_0$  offset while intra-voxel field heterogeneities are addressed by the dissipative term  $T_2'$ . More common for GRE acquisitions,  $T_2$  and  $T_2'$  are condensed to the effective transversal relaxation time  $T_2^*$  (Eq. 2.3):

$$M_{xy\text{Voxel}} = M_0 \sin(\alpha) \left[ \frac{1 - E_1}{1 - E_1 \cos(\alpha)} \right] e^{i(\Delta\omega_0 TE + \Phi)} e^{-TE/T_2^*} \quad (2.33)$$

The sensitivity of GRE to off-resonances is comfortably controlled by choosing the echo time, often referred to as  $T_2^*$ -weighting, since the phase dispersion in Eq. 2.29, hence  $T_2'$  magnitude reduction scales with TE. For the detection of cells, a trade-off in  $T_2^*$  weighting is important for distinguishing the cellular signal voids from the background. A special issue for GRE acquisitions is to detect cells close to borders of tissues with differences in their magnetic susceptibility. In such areas, background signal is degraded by global field inhomogeneities and cellular contrast is degraded.

Therefore, the success of cell tracking with MRI strongly depends on the targeted tissue. Bone marrow and lung parenchyma, both of high importance in basic medical research,

## 2. BASIC PRINCIPLES OF MR GUIDED CELL TRACKING

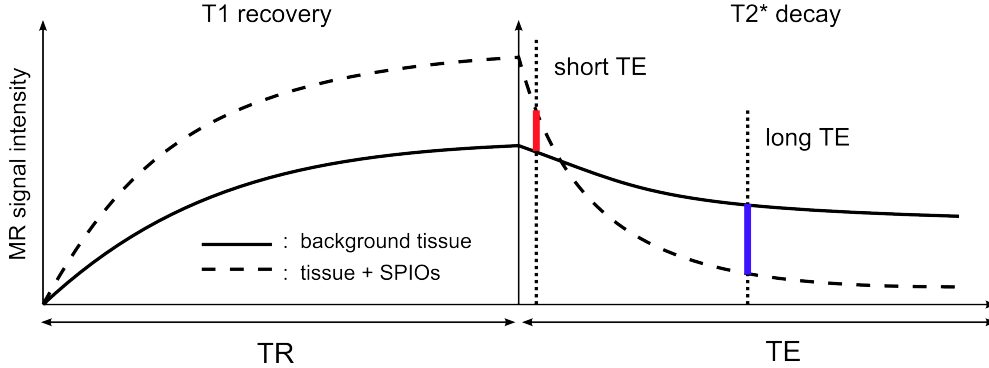


**Figure 2.4:**  $T_1$  and  $T_2^*$  contrast regime of SPIOs. The  $r_1$  relaxivity of SPIOs allow for a  $T_1$  associated positive contrast (red) at ultra-short time to echo (TE) and a  $r_2$  associated negative contrast ( $T_2^*$ ) at later TE. Both acquisitions can be merged by subtraction resulting in an enhanced iron oxide contrast.

are known to be most unfavorable biologic tissues in terms of background signal for MRI guided cell tracking.

### 2.3.1.2 Synergistic $T_1$ - $T_2^*$ contrast

The primarily high  $r_1$  relaxivity of SPIOs undergoes a reduction if internalized into cells known as the  $T_1$  quenching effect (discussed in section 2.2.2.1). The reduction of  $r_1$  yields a further boost in  $r_2^*/r_1$ , and hence, a pronounced  $T_2^*$  contrast of labeled cells. However, the remaining  $r_1$  actually shortens the background  $T_1$  which can be used to gain  $T_1$  positive contrast images if the time to echo chosen is short enough. The contrast in dependence of TE is sketched in figure 2.4<sup>1</sup>. Signal contrast between background and SPIOs is either positive (marked with the red bar) or negative (blue) depending on the chosen TE. The amount of positive contrast is determined by the used TR and flip angle  $\alpha$ , the so called  $T_1$ -weighting of the GRE sequence (square brackets in Eq.2.29).

Girard et al. investigated the dominant contrast mechanism ( $T_1$  vs.  $T_2^*$ ) depending on background  $T_1$  and  $T_2^*$  values [115]. They reported that, especially in tissues with relatively short  $T_2^*$  such as within bone marrow, the contrast efficiency given as  $\Delta T_2^*/T_2^*$  and  $\Delta T_1/T_1$  for  $T_2^*$  and  $T_1$  contrast, respectively, is much higher for  $T_1$  than for  $T_2^*$  if an echo is produced directly after excitation preserving the  $T_1$  contrast before destructive

<sup>1</sup>Figure is recreated from Girard et al. [115]

## 2.3 Acquisition strategies for cell tracking with MRI

---

$T_2^*$  dephasing destroys this signal gain. A second echo acquired at later TE can be used to further increase the contrast by suppressing non- $T_2^*$ -enhanced background tissue by subtraction ( $T_1$ - $T_2^*$  contrast). However, GRE sequences with ultra-short echo times are not standard imaging protocols and their technical implementation is challenging. A detailed description of such sequences can be found in sections 4.1.1 and 4.2.

### 2.3.1.3 Cell tracking studies based on GRE

In the early 1990ies, first feasibility studies on MRI guided imaging of iron loaded cells were reported [116, 117, 118, 119]. Some years later, successful tracking of labeled cells was presented by Bulte et al. [120]. Within their work they showed that magnetically labeled oligodendrocyte progenitors moved up to 10 mm away from the injection site within 10 to 14 days post transplantation. Those progenitors produced intact layers of myelin in a myelin deficient rat model confirmed by histology. Although in this study the gradient echo images were acquired after removal of the spinal cord ex vivo, it was one of the first studies presenting intact stem cell homing to the foci of disease with a successful co-registration of hypointense MR contrast originating from the labeled cells.

From that point on, many MRI based stem cell tracking studies confirmed the potential of this non-invasive imaging methodology to detect intact functional cells [84, 87, 121, 122, 123, 124, 125, 126, 127]. These studies were carried out mainly on disease models of the central nervous system and the heart. Cerebral applications especially benefit from very desirable properties of the background tissue: Almost no motion can be expected and, despite the areas being located next to the auditory canal, the minor susceptibility differences within the brain allow for gradient echo acquisitions with a high sensitivity to the cellular signal. Those optimal imaging conditions allowed for early (2002) reports on successful in vivo MRI guided cell trafficking within rat brains [121]. They transplanted an amount as little as 30,000 embryonic stem cells labeled with SPIOs between the cortex and corpus collosum contralaterally to a focal ischemic area. While using a 7 T dedicated animal scanner able to produce a GRE image at a resolution of  $78 \times 49 \times 78 \mu\text{m}^3$ , spatial dynamics of the transplanted labeled cells were observed from the injection site towards the site of infarction. Comparable in vivo tracking studies followed based on other neurologic disease models and fieldstrengths [122, 123].

## 2. BASIC PRINCIPLES OF MR GUIDED CELL TRACKING

---

Almost in parallel to the development of cell tracking studies in the brain, the field of cardiac research made use of non-invasive imaging of stem cell homing. Motivated by the vast growth of cardiac related diseases and the highly promising potential of cell-based therapies in this field [125], numerous scientific groups committed themselves to the complex task of imaging the moving heart of rodents. Cardiac triggering and gating in conjunction with high gradient inserts of dedicated preclinical systems allow for the detection of minor amounts of iron oxide labeled stem and progenitor cells in the beating heart. Epicardium-derived cells labeled with SPIOs could be detected at a concentration of  $2 \times 10^4/\mu\text{l}$  at  $100 \times 100 \times 500 \mu\text{m}^3$  and 9.4 T after direct transplantation into the myocardium of rats [87]. Another direct transplantation study showed in vivo cellular imaging within the mouse myocardium [127] where SPIO labeled EPCs at a cellular density of 10,000 cells/ $\mu\text{l}$  had been transplanted. Imaging at 4.7 T (ECG gated GRE at  $(230 \mu\text{m})^3$ ) showed excellent agreement with ex vivo histology performed after scanning. An important gain in detectability was reached by administering Gd-DTPA to enhance the myocardial background signal.

Trafficking of endothelial progenitors involved in tumor regression was shown at 7 T with a gradient echo sequence of  $70 \times 70 \times 500 \mu\text{m}^3$  [124]. The SPIO marked cells were injected intravenously and clearly detected 7 - 21 days after transplantation. Histology confirmed the contribution of the systemically injected cells to functional neovasculation.

The availability of clinical machines continued to further feasibility studies for cellular imaging on lower field strengths. The limitations that come with the gradient performance of such systems changed the strategy of high imaging resolutions towards a maximum of cellular iron payload. In vitro single cell detection at 1.5 T was reported by Foster-Gareau et al. ( $100 \times 100 \times 200 \mu\text{m}^3$ ) [58] and Hsiao et al. ( $60 \times 60 \times 700 \mu\text{m}^3$ ) [128], achieved by increasing the cellular iron content to 27.8 pg Fe/cell and 23.4 pg Fe/cell respectively. At 3 T and a GRE resolution of  $20 \times 33 \times 1500 \mu\text{m}^3$ , SPIO labeled mesenchymal stem cells (MSC) were tracked after intraaortal injection into a model of akute kidney injury in rats [126]. MSC engraftment of single labeled cells (a cellular concentration of 1.5 cells/ $\mu\text{l}$  was estimated) in the kidneys was visible 14 days after systemic injection of  $1.5 \cdot 10^6$  MSCs. Even though a high cellular concentration ( $2 \cdot 10^6$ ) and a direct application technique were employed, Amsalem et al. [84] were able to perform cardiac imaging in rats at 0.5 T with a high contrast of the SPIO

labeled MSCs.

These examples demonstrate that MRI guided cell tracking through gradient echo imaging has a high potential to satisfy the needs of longitudinal trafficking studies in rodents.

The key-requirements for success can be condensed to the following:

- A well-defined amount of iron oxides per cell is needed (depending on imaging resolution)
- Dedicated coils have to be employed to allow for acceptable SNR at the desired resolutions
- A bright (tissue) background signal is mandatory
- The background tissue should be free of susceptibility artifacts which may misinterpreted as cellular contrast

### 2.3.2 Fully Balanced Steady State Sequences

In comparison to customary spoiled GRE sequences, fully balanced steady state sequences (bSSFP or True FISP) do not destroy the transversal magnetization at the end of TR. Quite the contrary is the case. Transversal magnetization is preserved yielding very high tissue SNR per unit measurement time. By changing the phase of excitation (phase-cycling) from TR to TR by  $180^\circ$  the residual transversal magnetization is flipped back, and the coherent transverse magnetization continues to contribute to the signal in successive repetition intervals [129]. To preserve phase coherence of the stimulated echos through successive TRs, the gradients played on all three axes have to be rewinded. "Rewinding" means that the accumulated gradient moments ( $M_G = G \cdot t_G$ ) have to be zero at the end of TR. This is why bSSFP is called a balanced pulse sequence. The transversal signal without any off-resonances is given by [130]

$$M_{xy} = M_0 \sin(\alpha) \left[ \frac{1 - E_1}{1 - (E_1 - E_2) \cos(\alpha) - E_1 E_2} \right] e^{-TE/T_2} \quad (2.34)$$

with

$$E_1 = e^{-TR/T_1} \quad \text{and} \quad E_2 = e^{-TR/T_2}. \quad (2.35)$$

## 2. BASIC PRINCIPLES OF MR GUIDED CELL TRACKING

---

In contrast to spoiled GRE sequences, the steady state magnetization depends on  $T_2$ . The sequence contrast of bSSFP can not be chosen to be  $T_1$ - or  $T_2$ -weighted, but represents a ratio of both. At short TR and  $TR \ll T_2$  equation 2.34 reduces to [131]:

$$M_{xy} = M_0 \sin(\alpha) \left[ \frac{1}{T_1/T_2 (1 - \cos(\alpha)) + (1 + \cos(\alpha))} \right] e^{-TE/T_2}. \quad (2.36)$$

Because of  $T_1/T_2$  in the denominator, the bSSFP contrast is often understood as " $T_2/T_1$ "-weighted. As for spoiled GRE, an optimal flip angle for maximal signal can be calculated if background  $T_1$  and  $T_2$  are known [131]:

$$\alpha_{max} = \arccos \left( \frac{T_1 - T_2}{T_1 + T_2} \right). \quad (2.37)$$

### 2.3.2.1 $T_2^*$ contrast in the steady state

The bSSFP signal gets even more complex to conceive if spin isochromats with resonant offset frequencies have to be assumed. In the worst case, the frequency offsets cause the transversal magnetization to rotate about  $180^\circ$  until the next RF excitation. While playing the next negative-phased RF pulse, the magnetization is not flipped back but starts to cycle around the origin which yields a steady state value of zero. Therefore, the steady state magnetization depends on the accumulated phase angle  $\theta$  between successive excitations defined as [130]:

$$\theta = \gamma \cdot \Delta B_0 \cdot TR. \quad (2.38)$$

The transversal magnetization is usually described by its orthogonal components  $M_x^+$  and  $M_y^+$  with  $M_{xy} = M_x^+ + iM_y^+$  rotating with the same precessional direction as the RF excitation around the polarizing field  $B_0$  (denoted with  $^+$ ). Given this definition, the transversal magnetization of bSSFP is calculated for the timepoint directly after excitation [130]

$$\begin{aligned} M_x^+(\theta) &= M_0 (1 - E_1) (E_2 \sin \alpha \sin \theta) / D \\ M_y^+(\theta) &= M_0 (1 - E_1) ((1 + E_2 \cos \theta) \sin \alpha) / D \end{aligned} \quad (2.39)$$

with

$$E_1 = e^{-TR/T_1} \quad (2.40)$$

$$E_2 = e^{-TR/T_2} \quad (2.41)$$

$$D = (1 - E_1 \cos \alpha) (1 + E_2 \cos \theta) - (E_1 - \cos \alpha) (E_2 + \cos \theta) E_2. \quad (2.42)$$

At timepoint TE after excitation, equation 2.39 is expanded by an additional phase and dissipative term [132]:

$$M_{xy} = (M_x^+(\theta) + iM_y^+(\theta)) e^{i\theta TE/TR} e^{-TE/T_2}. \quad (2.43)$$

Simulations on the transversal bSSFP magnetization  $M_{xy}$  in equation 2.43 for different resonant offsets (hence accumulated phase over TR =  $\theta$ ) plotted in figure 2.5 show a strong off-resonant frequency dependent magnitude and phase modulation (simulated parameters:  $T_1 = 3500$  ms,  $T_2 = 250$ , TR = 6.5 ms, TE = TR/2,  $\alpha = 25^\circ$ ,  $M_0 = 1$ ). Depending on the success of smoothing the polarizing  $B_0$  field through shimming, the magnetic field across the FOV varies as a function of position. At voxels where a field-offset in  $B_0$  causes a rotation of the magnetization by  $\theta = \pm(1+2n)\pi$  within TR, where  $n$  is an integer, the measured signal gets zero (see figure 2.5). This undesirable signal cancellation at these so called bands become a problem especially at long repetition times TR. Therefore, bSSFP acquisitions are known to be challenging in terms of  $B_0$  homogeneity and gradient system performance, where latter limits the shortest possible TR. Since global  $B_0$  inhomogeneities are of large scale compared to the voxel dimensions, the intra-voxel magnetic field is generally considered as to be constant over the voxel extent. Hence, one isochromat per voxel can be assumed. However, if iron loaded cells with strong magnetic dipole fields are present, the intra-voxel magnetic field is modulated over a wide range. An exemplary dipole-field for a cell loaded with 25 pg Fe SPIO is shown in figure 2.6a. Figures 2.6b and 2.6c give insight to the intra-voxel bSSFP signal response to these off-resonances as calculated with Eq. 2.43 (simulated

## 2. BASIC PRINCIPLES OF MR GUIDED CELL TRACKING

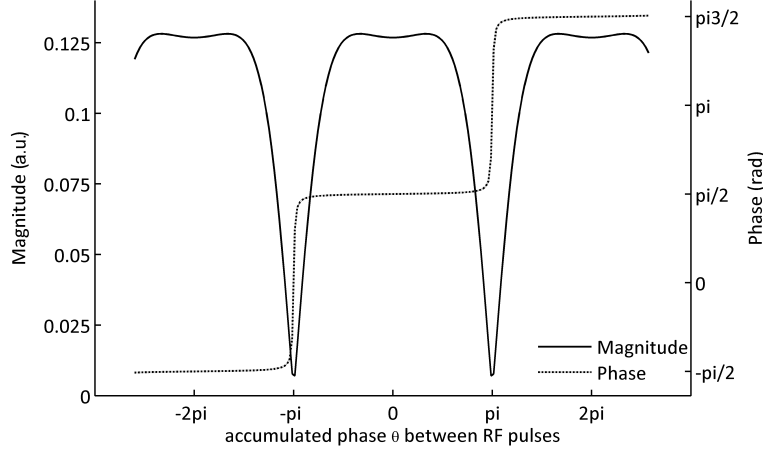


**Figure 2.5:** bSSFP signal response to off-resonances. Depending on the accumulated phase  $\theta$  during successive excitation pulses, the transversal bSSFP magnetization undergoes a magnitude signal drop at  $\theta$  equal to multiples of  $(1+2n)\pi$ . The spectral distance, or bands, between these signal gaps depends on TR ( $\Delta\theta = 2\pi \hat{=} 1/TR$ ).

parameters:  $T_1 = 3500$  ms,  $T_2 = 250$ , TR = 6.5 ms, TE = TR/2,  $\alpha = 25^\circ$ ,  $M_0 = 1$ ; the dipolar field was calculated and intra-voxel simulations were carried out as described in section 5.2.3). Within the shown  $(200 \mu\text{m})^3$  voxel, many bands are present which give rise to two dissipative mechanisms: First, multiple bSSFP-banding signal drops are present (fig. 2.6c&f), and second, even more important for voxel signal degradation and apparent  $T_2^*$  contrast, multiple bands within that voxel have opposed phases (phase jumps of  $\pi$  in fig. 2.6b&e).

Lebel et al. [110] investigated the impact of intra-voxel opposed phase conditions as presented in figure 2.6 on the total image voxel contrast of iron labeled cells. They showed on the bases of intra-voxel signal calculations that the phase reversals contribute to the highest extent to the bSSFP  $T_2^*$  contrast. If optimal SNR flip-angle,  $TR \ll T_2$  and long  $T_1$  ( $T_1 \gg T_2$ ) are assumed, about 89% of the voxel signal degradation is caused by the phase-reversals of bands whereas magnitude banding is accountable for the remaining 11% of signal loss. Within their study, Lebel et al. substantiated that the cellular bSSFP contrast is quantitative in the sense of a well-defined relation between relative MR signal loss  $\Delta S/S_0$  (with  $\Delta S = S_{cell} - S_0$  the absolute signal change in the presence of an iron loaded cell and  $S_0$  the background signal) and local magnetic dose

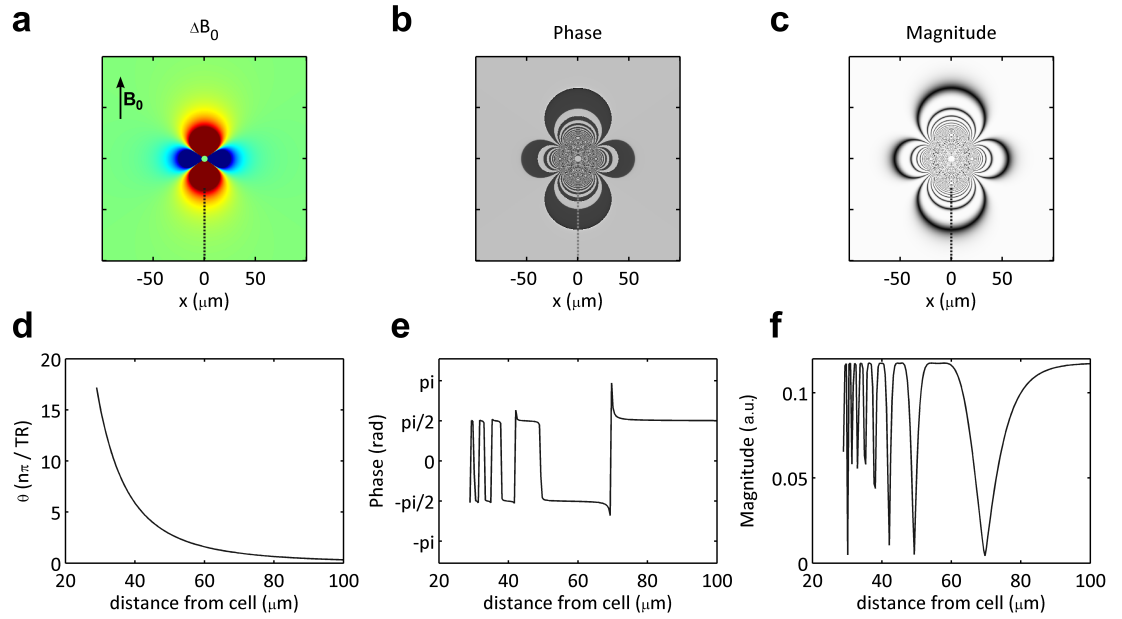


**Figure 2.6:** **a:** Simulated magnetic dipole field from a cell loaded with 25 pg Fe. Phase (**b**) and magnitude (**c**) response of the transversal magnetization to a bSSFP experiment with  $TR = 6.5$  ms and a flip angle of  $25^\circ$ . **d:** Accumulated signal phase per TR  $\theta$  along the dashed line in (**a**). The same radial profile is presented for the resultant bSSFP phase (**e**) and magnitude (**f**). For bSSFP imaging of iron loaded cells, the phase alteration about  $180^\circ$  between successive off-resonant bands in addition to the magnitude drop at  $\theta = \pm(1+2n)\pi$  causes intra-voxel signal degradation. The sign alterations about  $\pi$  between neighbored bands of off-resonances yields intra-voxel signal cancellation and is the dominant contrast mechanism in bSSFP imaging of iron loaded cells.

## 2. BASIC PRINCIPLES OF MR GUIDED CELL TRACKING

---

*LMD* of the iron loaded cells (see section 2.1.3.2) linked through the fractional signal loss  $K_{fsl}$ :

$$\frac{\Delta S}{S_0} = K_{fsl} \cdot LMD. \quad (2.44)$$

They determined for bSSFP a value of  $K_{fsl} = 4.12$  which is comparable to that of spoiled GRE acquisitions ( $K_{fsl} = 4.03$ ). Another assumption from their work and Heyn et al. [102] is that bSSFP even exceeds the cellular detection limit of conventional spoiled GRE acquisitions since next to the high fractional signal loss  $K_{fsl}$  the gained cellular contrast-to-noise (CNR) figure

$$CNR = \frac{\Delta S}{S_0} \cdot SNR = K_{fsl} \cdot LMD \cdot SNR \quad (2.45)$$

of bSSFP is much higher compared to GRE if acquisition time is taken into account [58]. Heyn et al. calculated that 25 pg Fe per cell are sufficient to reach the detection limit for a single labeled cell at a resolution of  $(200 \mu\text{m})^3$  and an image SNR of 25.

### 2.3.2.2 Cell tracking studies based on bSSFP

In vitro studies on a 1.5 T wide-bore system equipped with a high-power (600 mT/m) gradient system showed the feasibility of bSSFP imaging of single labeled cells at low fieldstrength and at moderate cellular iron dosages of 9 pgFe/cell [58]. It was the same group that presented the contrast regime of iron labeled cells in the fully balanced steady state [102], and some years later an in vivo cell tracking study presenting single retained macrophages in mouse brains after a left ventricular delivery of 10,000 labeled (60.9 pgFe/cell) individuals [112]. At 3 T, labeled glioma cells imaged 18 days after direct injection into the brain showed up as single dark spots within a bSSFP acquisition with  $100 \times 100 \times 100 \mu\text{m}^3$  (dedicated gradient coil insert 500 mT/m, slew rate 3200 T/m/s) [133]. Later on, the same group presented bSSFP based tracking of single labeled immune cells [134] and mesenchymal stromal cells [135].

The strikingly small amount of published work on bSSFP based cell tracking is most likely due to the more complex steady-state signal behavior to global off-resonances. The drawbacks of banding-artifacts that came with bSSFP exceed the contrast gain

compared to spoiled GRE imaging if SNR at the required resolutions is not a limiting factor. Dedicated preclinical high-field systems are much more prone to global  $B_0$  inhomogeneities, and the dedicated coils in combination with the high main magnetic field strengths deliver the required SNR for high-resolution GRE images. However, in low-field systems, SNR gets important and bSSFP acquisitions become more attractive. Of course, global banding is an issue even for low-field systems, and the published work made use of high power gradient inserts to keep TR below 10 ms at the high resolutions acquired.

### 2.3.3 Sequences producing positive cellular contrast

Despite the high sensitivity of spoiled GRE and bSSFP images to iron loaded cells, the specificity of the contrast is quite low. Differentiation of cellular signal voids from a heterogeneous or low background signal is challenging.

To improve this, several positive contrast methods have been proposed. The main goal herein is to saturate the background while producing a signal enhancement in close proximity to the cell containing voxel. This can be achieved by mapping the cell associated off-resonance frequency shift with a positive signal via saturation of the on-resonant, non disturbed water protons [136], or by excitation of the off-resonant water [137]. Mapping  $B_0$ -field offsets was shown with bSSFP by exploiting the signal enhancement next to the off-resonant singularity point of low tip angle bSSFP [138, 139]. Other methods use imaging gradients for field-compensation, and hence acquire positive signal in voxels with high  $B_0$  gradients applied to gradient echo [140, 141, 142] and bSSFP acquisitions [143]. A method obtaining positive contrast that does not need a pulse sequence adaption is based on the off-resonant associated echo-shift in k-space which is mapped to a positive contrast employing standard GRE [144] or adaptations of susceptibility weighted imaging which exploit the phase information of GRE acquisitions [145]. All these methods have in common that they produce signal enhancement which is spatially displaced from the cell. They need either a certain linear field gradient or a non de-phased voxel with a distinct frequency offset for contrast generation. None of these requirements are met in the cell-containing voxel. The intra-voxel field distortions lead to a complete loss of phase coherence which cannot even be re-phased by gradient compensation techniques [140, 141, 142]. As a consequence, positive contrast techniques generate hyperintensities in neighboring image pixels where

## 2. BASIC PRINCIPLES OF MR GUIDED CELL TRACKING

---

the needed phase and frequency conditions are met. However, many labeled cells are required to gain a magnetic field pattern exceeding the cell containing voxel which in turn contradicts single cell detection required for in vivo cell migration studies [56, 120, 146].

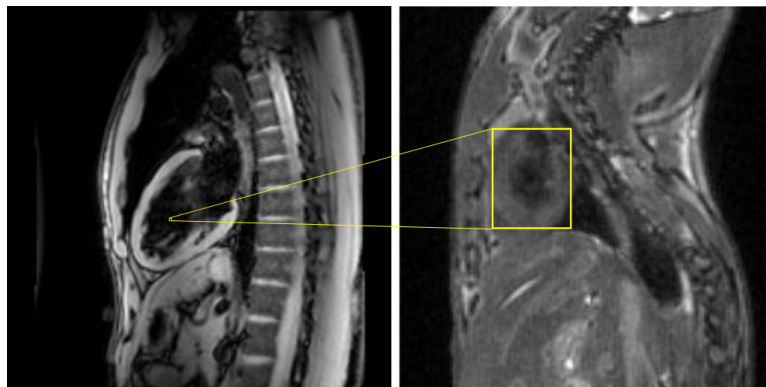
### 2.3.3.1 Cell tracking studies based on positive contrast techniques

Stuber et al. showed an in vivo application of their inversion recovery sequence with on-resonant water suppression (IRON) [136] on the basis of direct injection sites within the hindlimb of rabbits at 3 T. The course resolution of the 2D experiment with 3 mm slice thickness and  $(450 \mu\text{m})^2$  inplane resolution showed positive contrast from 125,000 cells (1000 cells/ $\mu\text{l}$ ). The spectral selective excitation approach published by Cunningham et al. [137] showed successful in vivo cellular imaging at a density of 10,000 cells/ $\mu\text{l}$  within the hindlimb of a mouse at 2 mm slice thickness and  $\approx 300 \mu\text{m} \times 400 \mu\text{m}$  resolution and 1.5 T. Again on comparable low fieldstrength of 1.5 T, the bSSFP small tip-angle approach PARTS showed positive contrast for 500 cells/ $\mu\text{l}$  [139]. In vivo demonstrations for the field-compensation method were carried out in pigs, even though endovascular paramagnetic markers, not labeled cells, were in the focus of this research [140]. The most sensitive approach is based on calculating positive contrast images out of phase information of GRE datasets [145] even though this technique is quite limited since a very homogeneous background field is mandatory. However, this work presented single cell detection with positive contrast in vivo within a murine traumatic brain injury at 7 T and  $58 \mu\text{m} \times 79 \mu\text{m} \times 79 \mu\text{m}$  resolution.

## 2.4 Technical considerations at imaging sub-millimeter resolutions on clinical MRI hardware

Most preclinical studies are based on mice and rats. In order to produce reasonable MR images, the field-of-view (FOV) has to be adapted to match the morphologic structures of those animals. The MR images in figure 2.7 give an example for the scale between human and preclinical MRI. The need for high image resolutions is accompanied with a low signal-to-noise ratio (SNR) and high demands on the magnetic field gradients used for spatial encoding [147, 148]. To give a better understanding of the difficulties in imaging sub-millimetre resolutions, issues on SNR and spatial encoding are discussed within this section.

**Figure 2.7:** MR images acquired through gradient echo sequences at 3T. The scale between human and preclinical MRI exemplified for a sagittal view of a human (left) and a mouse (right) thorax. The huge difference in size is shown for the region of interest of the left ventricle.



### 2.4.1 SNR

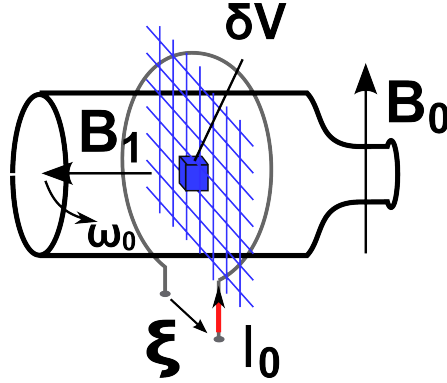
The signal-to-noise ratio provides a fundamental limitation to resolution in MRI since the signal available from each volume element (voxel) decreases as the voxel size is reduced [149, 150, 151]. In order to optimize and improve image acquisition to achieve high-resolution images it is mandatory to know the main parameters which can be tuned by the experimenter.

An important role in the subject of NMR receptivity has the type of nucleus to be imaged. The  $^1H$  nuclei with the natural abundance of 99.9885% and the gyromagnetic

## 2. BASIC PRINCIPLES OF MR GUIDED CELL TRACKING

---

**Figure 2.8:** Principle of NMR signal reception. A receive coil is placed orthogonal to the polarizing field  $B_0$ . The magnetization in  $\delta V$  rotates with  $\omega_0$  and produces a time-varying  $B_1$ -field inducing a voltage  $\xi$  into the receive coil.  $\delta V$ , the volume of a single pixel (voxel-volume), depends on the chosen resolution of the imaging grid (blue).



ratio of  $\gamma = 42.58$  MHz/T has the highest NMR sensitivity of all biologic relevant spin 1/2 nuclei [150]. In addition to the high NMR sensitivity, the average water fraction in humans by weight is estimated to be 53% [152] which explains the importance of proton MRI over all other nuclei in clinical applications. The thermal equilibrium magnetization  $M_0$  depends on the gyromagnetic ratio  $\gamma$  and the quantum number  $I$  of the nuclei to be measured given as [153]

$$M_0 = \rho_0 \frac{\gamma^2 \hbar^2 I(I+1)}{3k_B T_s} B_0. \quad (2.46)$$

With  $\rho_0$  the density of spins per unit volume,  $\hbar$  the reduced Planck constant,  $k_B$  the Boltzmann constant and  $T_s$  the sample temperature. Within the NMR experiment, this magnetization is measured through a coil which is inductively coupled to the rotating spin-system as presented in figure 2.8. The induced voltage  $\xi$  is calculated according to the law of reciprocity by

$$\xi = -\frac{\delta}{\delta t} (\vec{B}_1 \cdot \vec{m}) \quad (2.47)$$

with

$$\vec{B}_1 = \frac{\vec{B}_1}{I_0} \quad (2.48)$$

## 2.4 Technical considerations at imaging sub-millimeter resolutions on clinical MRI hardware

---

the produced  $B_1$  field per unit current  $I_0$  in the coil and  $\vec{m}$  the magnetization rotating in the transversal plane of the volume  $\delta V$ :

$$\vec{m} = M_0 \delta V \sin(\omega_0 t) \vec{e}_m. \quad (2.49)$$

This finally leads to the formula for the induced voltage:

$$\xi = B_0^2 \delta V \frac{B_1}{I_0} \rho_0 \frac{\gamma^3 \hbar^2 I(I+1)}{3k_B T_s} \cos \omega_0 t. \quad (2.50)$$

Signal to noise ratio (SNR) is defined as the received signal over the root mean square amplitude of the received noise  $\sigma_n$

$$SNR = \frac{\xi}{\sigma_n} \quad (2.51)$$

and with  $k_B$  the Boltzmann constant,  $T$  the absolute temperature and  $\Delta f$  the equivalent noise bandwidth the noise is

$$\sigma_n = \sqrt{4k_B T r \Delta f}. \quad (2.52)$$

Herein, the equivalent noise resistance  $r$  consists of Joule losses within the receiving coil, magnetic losses within the imaging volume (eddy currents) and dielectric losses of the RF-field [154]. Considering clinical field strengths, the magnetic losses  $r_M$  within the tissue with a resistivity  $\rho$  are most dominant [150, 154] and related to the frequency  $\omega_0$  of the  $B_1$  field:

$$r_M \approx \rho \omega_0^2. \quad (2.53)$$

The final SNR is

$$\frac{\xi}{\sigma_n} = B_0^2 \delta V \frac{B_1}{I_0} \frac{\cos \omega_0 t}{\sqrt{4k_B T r \Delta f}} k \quad (2.54)$$

## 2. BASIC PRINCIPLES OF MR GUIDED CELL TRACKING

---

with  $k$  being a proportionality constant depending on the type and density of the imaged nucleus. The induced voltage in Eq.2.50 shows a quadratic dependence to the main magnetic field  $B_0$  while the equivalent noise scales linearly (square root of Eq.2.52 and  $\omega_0 = \gamma B_0$ ), resulting in a linear dependence of SNR with  $B_0$ .

All components that have an impact on SNR can be condensed to:

- $B_0$   
signal  $\approx B_0^2$ , noise  $\approx B_0$
- $\delta V$   
image voxel volume
- $B_1/I_0$   
coil efficiency
- $1/\sqrt{T}$   
Joule losses within the receiver path
- $1/\sqrt{\Delta f}$   
receiver bandwidth
- $k \equiv \textit{nucleus}$   
density and NMR receptivity

Following these assumptions, the intrinsic SNR can be improved either by investments in imaging hardware through high-field systems and dedicated coils, or by the acquisition of enlarged voxel dimensions ( $\delta V$ ) and a lower imaging bandwidth.

Considering the example of the murine heart in figure 2.7, the volume of interest is reduced by a factor of 1000 resulting in 1000 times lower SNR if no adaptations in the acquisition or imaging hardware are made.

### 2.4.2 Main magnetic fieldstrength

Following the assumptions of Eq. 2.54, SNR scales with the main magnetic fieldstrength  $B_0$ . However, an increase in the polarizing fieldstrength  $B_0$  is coupled to a

## 2.4 Technical considerations at imaging sub-millimeter resolutions on clinical MRI hardware

---

weak shortening of  $T_2$  and a pronounced lengthening of the spin-lattice relaxation time  $T_1$  [155, 156, 157]. The latter leads to a prolonged experimental repetition time for the same magnitude of steady state magnetization as compared to experiments at low magnetic fieldstrengths. Hence, for the apparent performance in the sense of image SNR efficiency the needed measurement time has to be taken into account. SNR scales with the number of averages used (see section 2.4.4). Therefore, SNR efficiency is frequently defined as the SNR per square root of total acquisition time [129].

Boef et al. [158] presented SNR numbers acquired at preclinical MRI studies and compared them between 1.5 T and 7 T. They identified the enhanced  $T_2$  contrast as a valuable benefit in imaging the brain, whereas the increase in  $T_1$  represents a major limiting factor for high-field in vivo SNR. On phantoms consisting of non-conducting fluids (where conductive field-dependent losses can be neglected) and equal  $T_1$  times for 1.5 T and 7 T, respectively, the authors showed that experimentally determined numbers for the high field system were far below theoretical estimations. Despite the use of RF-coils with the same geometrical dimensions, the SNR efficiency values deviated in the order of 2 to 3 times from the ones expected. Boef et al. argued that preamplifier noise figures at high frequencies and transmit/receive coil coupling account for the observed SNR at 7 T.

Further limitations of high-field imaging are an enhanced sensitivity to susceptibility artifacts and a reduced contrast agent relaxivity  $r_1$ . The scaling of susceptibility-induced field-heterogeneity (Eq. 2.7) with  $B_0$  aggravates the application of fully balanced sequences which are degraded at high-field systems by banding artifacts. For molecular imaging applications, the loss in relaxivity  $r_1$  of magnetic nanoparticles used as  $T_1$  imaging probes, known as the nuclear magnetic resonance dispersion (NMRD), states a major problem at high fieldstrengths [105].

### 2.4.3 RF-coils

There are two major groups of RF-coils used in MRI: Surface coils which are directly applied to the subject's skin, and volume coils that surround the whole subject under investigation.

The majority of volume coils are made of an arrangement of copper rods placed along a ring which gives this type of coil the characteristic name *birdcage* [159]. Birdcage coils have the advantage of a very homogeneous  $B_1$  field within the "cage" covering the

## 2. BASIC PRINCIPLES OF MR GUIDED CELL TRACKING

---

whole imaging FOV. The cylindrical symmetry allows for a quadrature mode which increases SNR by a factor of 1.4 compared to linear driven surface coils, since both orthogonal components of the magnetization vector are received [159]. Despite this valuable gain in SNR, the fixed arrangement of the coil elements lead to an increased distance between the conductors and the object to be imaged, reducing the coil's efficiency. Therefore, the inner diameter of volume coils is an indicator of the inherent SNR of the coil. For example, a dedicated volume coil for rats (7 cm diameter) delivers 1.7 times the SNR of a human wrist coil (8.5 cm i.d.) and a dedicated mouse coil (3.5 cm i.d.) is able to improve the SNR of the wrist coil by a factor of 5.3 (measured values at 3 T on a spherical 3 cm diameter agarose-phantom). Therefore, adapting the coil dimensions to the desired object of interest is a comfortable and mandatory step to improve SNR for high resolution imaging.

A step further in matching the receive coil to the FOV can be made with surface coils. If the FOV is situated next to the skin, planar coils ensure an optimal linkage of the magnetic flux with the tissue magnetization and therefore, the SNR of the coil is maximized. While  $B_1$  field penetration of one coil is very limited and inhomogeneous, multiple surface coils can be used to enlarge the FOV and improve the low  $B_1$  homogeneity of a single loop. The individual signals are combined to form a single image of the complete FOV. These coils, also known as *phased arrays*, are widely used in clinical MRI investigations since they provide a large FOV coverage with the SNR and therefore, resolution capabilities of a small surface coil [160]. However, the main advantage of phased array coils in clinical practice is that the intrinsic spatial information of each surface coil given by its position can be used to accelerate imaging. With dedicated parallel image reconstruction techniques (e.g. SENSE [161] or GRAPPA [162]) the used number of acquisitions for spatial encoding is reduced by a factor of  $R$  (acceleration factor) depending on the number of independent receive channels available. The downside that comes with a boost in acquisition time is a reduced image SNR [161]:

$$SNR_{acc} \propto \frac{SNR_{full}}{g\sqrt{R}}. \quad (2.55)$$

Eq. 2.55 states that for parallel MRI, SNR is degraded by the square root of the acceleration  $R$  in addition to a spatially dependent noise amplification  $g$  in areas where coils have a significant overlap of their sensitivities. Hence, for SNR demanding preclinical

## 2.4 Technical considerations at imaging sub-millimeter resolutions on clinical MRI hardware

---

MRI applications, the benefit of phased arrays is to extend the FOV at the high SNR of a small surface coil rather than accelerating image acquisition.

### 2.4.4 Signal averaging

By summing up images from successive experiments, a technique known as averaging, the intrinsic imaging SNR can be improved [150]. Noise adds with random phase while the signal adds coherently. Since noise power  $\sigma^2$  is additive, its root-mean-squared amplitude scales with  $\sqrt{N}$  over successive averages  $N$  which results in a total SNR improvement with the square root of the number of experiments. A limitation of averaging is the time required for a full longitudinal recovery between successive experimental repetitions. However, for fast gradient echo imaging the repetition time is always smaller than  $T_1$ . In that case, assuming the use of the optimal Ernst angle (eq. 2.31), the received signal enhances roughly with the square root of TR [163]. This means that the signal gain by choosing a longer TR for magnetization recovery is almost equal to the gain achieved by averaging during the same acquisition time using a reduced TR. The benefit of signal averaging in that case is that motion-induced view-to-view inconsistencies during data acquisition are suppressed [164].

### 2.4.5 Gradient performance

Gradient fields are used to encode the protons' positions by modulating the resonant frequency linearly with spatial location. This concept is realized by applying magnetic field gradients  $G$  which are superimposed to the polarizing field  $B_0$  and vary the magnetic field amplitude in  $\vec{e}_z$ , the direction of the main magnetic field, linearly with the spatial position  $\mathbf{r} = x\vec{e}_x + y\vec{e}_y + z\vec{e}_z$ :

$$B_z(\mathbf{r}) = B_0 + G_x x + G_y y + G_z z. \quad (2.56)$$

The gradient coils of clinical MRI's are optimized to match the required resolution and imaging speed for human applications. For example, the voxel size for standard human MR imaging is in the millimeter range and limited by the SNR gained with the used RF-coils. The focus in optimizing gradient coils for human MRI is on gradient homogeneity within the large FOV and eddy current reduction in order to achieve a fast

## 2. BASIC PRINCIPLES OF MR GUIDED CELL TRACKING

---

distortion-free acquisition [165, 166]. Besides these technical challenges, there are major constraints to gradient speed originating from the high  $dB/dt$  values while rapidly switching the gradients polarity. The voltages induced into the patient are in the frequency range between 1 - 10 kHz [167] and cause a depolarization of nerve fibers known as peripheral nerve stimulation (PNS) which has to be considered for reasons of patient safety. Given the aforementioned constraints, state of the art wide-bore gradient systems deliver a gradient strength of 40 mT/m at a maximum slew rate of 200 T/m/s. In comparison, dedicated preclinical scanners are supplied with gradient systems from 400 up to 1000 mT/m and slew rates of 3500 up to 9000 T/m/s. This comparison is of course flawed since the preclinical FOV's are limited to a few centimeters and PNS is not a problem for anesthetized animals. However, it emphasizes the challenges in the implementation of preclinical studies on hardware conceived for imaging at 10-fold lower imaging resolutions.

In general, the gradient performance determines the speed of the imaging experiment. While resolution is technically not limited by the available gradient strength, a reduction of voxel dimensions prolongs the shortest possible time to echo TE and the duration of the sampling interval. For gradient recalled echo acquisitions, the sequence timing and imaging resolution is connected with the echo time dependent signal loss caused by  $T_2^*$ . As a consequence of  $T_2^*$ , the possible resolution is degraded since first, a reduced signal at time point TE reduces the measured SNR and second, the  $T_2^*$  decay during the readout causes a spectral, hence spatial, broadening of the originally single isochromat at location  $\mathbf{r}$ . To avoid spatial broadening, the readout time is kept as short as possible by enlarging the readout bandwidth. With the Rayleigh criterion [168] on the separability of two neighbored pixels, a  $T_2^*$  dependent minimum imaging bandwidth can be found to be  $N/(\pi T_2^*)$  [150].

Figure 2.9 shows how the timing of the pulse sequence is changed upon increasing image resolution. This is exemplified on the basis of a 2D gradient echo experiment, but the underlying principle is the same for every 2D sequence, e.g. a spin-echo where center k-space is acquired at the center of the readout gradient (often called a centered echo, or full echo sampling).

Neglecting  $T_2^*$  blurring, spatial resolution depends on the readout gradient strength

## 2.4 Technical considerations at imaging sub-millimeter resolutions on clinical MRI hardware

---

$G_{RO}$  and imaging bandwidth  $BW$ :

$$\Delta x = \frac{BW}{G_{RO} \cdot \gamma}. \quad (2.57)$$

For a reduction of the voxel size  $\Delta x$ , either the gradient strength has to be increased (fig. 2.9a→b) or the imaging bandwidth is reduced (fig. 2.9b→c). A higher gradient amplitude  $G_{RO}$  tends to result in a prolonged echo time since the readout pre-phasing gradient -half of the readout gradient moment in size executed before the readout- has to be enlarged (yellow area in fig. 2.9b). In addition to that echo time elongation, a reduced bandwidth yields an increased sampling duration  $T_s$ :

$$T_s = \frac{N}{BW}. \quad (2.58)$$

Thus the echo time is additionally extended by half of the readout lengthening, plus additional time needed for the pre-phasing gradient (blue area in fig. 2.9c). Consequentially imaging at small voxel dimensions lead to a prolonged TE and lengthened readout, hence, a decrease in separability caused by  $T_2^*$ , which have to be balanced to the gain in spatial information by the experimenter.

## 2. BASIC PRINCIPLES OF MR GUIDED CELL TRACKING

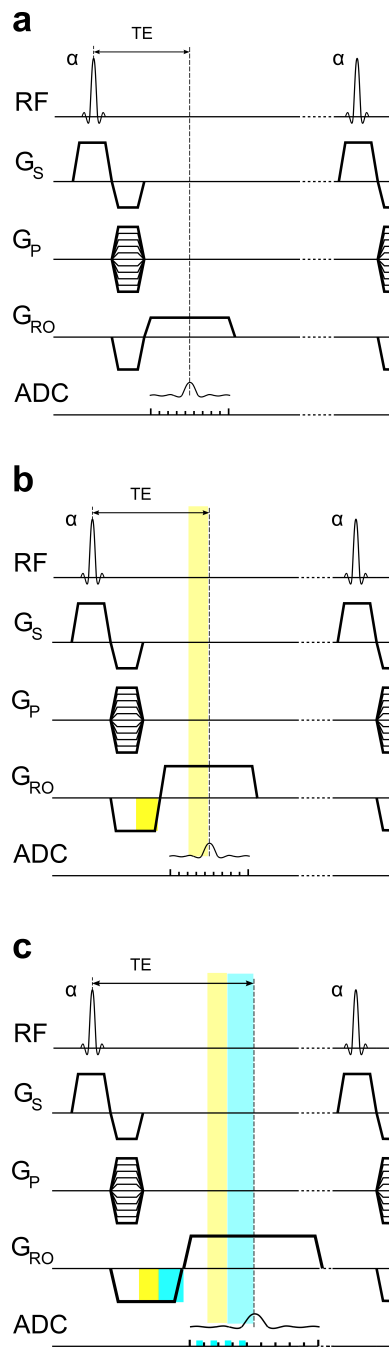


**Figure 2.9:** **a:** 2D gradient echo sequence diagram. **b:** Enhancing imaging resolution by enlarging the readout gradient strength leads to a longer echo time caused by an enlarged pre-phaser gradient moment (yellow). **c:** If imaging bandwidth is reduced to gain smaller imaging voxels, the readout gradient in addition to the pre-phaser is adapted (blue) and prolongs TE.

**3**

## **Amplification strategies for cell tracking with Cartesian trajectories**

### 3. AMPLIFICATION STRATEGIES FOR CELL TRACKING WITH CARTESIAN TRAJECTORIES

---

## 3.1 Enhanced contrast of single cells through zero-padding

### 3.1.1 Introduction

The presented study deals with an amplification strategy for single cell detection of iron oxide labeled cells imaged with gradient echo sequences.

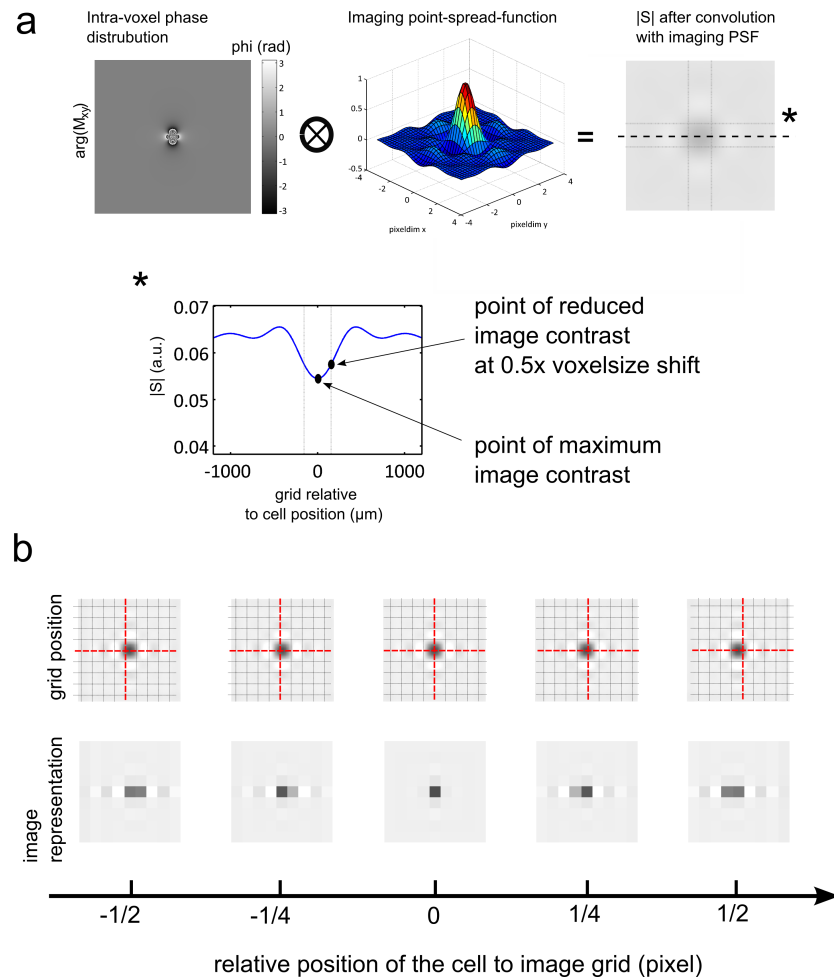
As a rule of thumb the achievable in vivo resolution for GRE images are about  $(100 \mu\text{m})^3$  at standard preclinical scanners and  $(200 \mu\text{m})^3$  on clinical MR hardware if dedicated preclinical RF-coils are used. The relatively large (with respect to the cellular size) voxel volume allows a great margin for the positioning of a cell within a voxel. Preliminary work [61, 102] identified that intra-voxel cellular positioning has a remarkable, even if not quantified by the authors, impact on the voxel contrast. This effect is often referred to as *partial volume effect*. The term *partial volume* may be misleading since - even if single labeled entities and their induced field inhomogeneity are fully entrapped within a particular voxel volume - an intra-voxel position-dependent contrast modulation is observed. Cells located centrally with respect to the discrete imaging grid show maximum contrast while cells spatially placed in between the grid show a reduced contrast. The cellular positioning within a voxel cannot be determined a priori and is principally arbitrary. Therefore, the acquired signal intensities may vary even if the same amount of cells with an equal paramagnetic load are imaged, which constitutes a major problem for cellular quantification.

Within this study it was investigated:

- The cellular partial volume effect with the aid of numerical simulations.
- The sensitivity of the contrast change with respect to different cellular iron payloads.
- A new reconstruction approach based on the theory of zero-padded Fourier transform in order to amplify the contrast of cells which are non-centered with respect to the imaging grid. This technique is able to exploit the initial, non-displaced cellular contrast.
- The new technique in vitro and show cellular contrast not visible with the standard reconstruction before. High resolution images are used to identify and confirm the origin of the new contrast from displaced cellular identities.

### 3.1 Enhanced contrast of single cells through zero-padding

**Figure 3.1:** (a, top) The punctuate magnetic dipole moment of a paramagnetically loaded cell induces an intra-voxel phase dispersion. Finite sampling yields a convolution of the point-spread-function with the spatial continuous magnetization. (a, bottom) Numerical intra-voxel simulations (50 pg Fe, PSF corresponding to  $(300 \mu\text{m})^3$  sampling) predict a maximum cellular contrast if the cell is placed centrally to the imaging grid and reduced contrast for a cell displaced by half the voxel dimension. This is further exemplified by shifting the grid about  $-1/2$  up to  $1/2$  of the voxel width (b).



### 3. AMPLIFICATION STRATEGIES FOR CELL TRACKING WITH CARTESIAN TRAJECTORIES

---

#### 3.1.2 Theory

##### 3.1.2.1 Cellular contrast and the image point spread function

Image formation, and hence voxel intensity, is a result of the Fourier transform of time discrete data points acquired with a dwell time  $DT$  over a finite sampling duration  $T$ . Finite sampling is associated with truncating a signal over time. This truncation is mathematically described by multiplying the time infinite data with a rectangular window of duration  $T$ . The Fourier transform of this window is the *point spread function* (PSF) and with the convolution theorem of Fourier transform, the spatial continuous information is mapped to the image by a convolution with the PSF [169].

Accordingly, voxel intensity  $S(\vec{x})$  is not a simple sum of the complex magnetization confined by the voxel volume, but results from a convolution ( $\star$ ) of the continuous transversal magnetization  $M_{xy}(\vec{x})$  with the imaging PSF:

$$S(\vec{x}) = M_{xy}(\vec{x}) \star PSF(\vec{x}). \quad (3.1)$$

If structures smaller than the discretization grid are of interest, the PSF introduces a contrast dependency on the intra-voxel position. For example, within a uniform background, there is about a 36% difference in contrast of a given ideal point source between when the object is placed exactly on the spatial position of the image grid and when it is placed in between two image points (a *sinc* shaped PSF assumed [153]). For 3D imaging, the contrast difference may be even more severe, since a displacement of half the voxel width in all 3 dimensions causes a relative contrast degradation of 74% already.

Iron labeled cells produce microscopic field perturbances which cause a phase dispersion across the voxel. Therefore, their contrast mechanism is not directly comparable with the point-like magnitude modulation given in the aforementioned example. Neglecting diffusion and assuming gradient echo acquisitions, the magnitude degradation of the acquired voxel is purely a result of the convolution of the PSF with magnetization of same magnitude but different phase angles (visualized in figure 3.1a).

The intra-voxel signal in figure 3.1 indicates that, despite the differences between the point-like object and the apparent phase dispersion pattern of labeled cells, the intra-voxel magnitude  $|S(\vec{x})|$  caused by a cellular perturber follows a course comparable to

### 3.1 Enhanced contrast of single cells through zero-padding

---

that of a point object convolved with the PSF. Consequentially, a dependence of the cellular contrast on the intra-voxel position of the cell is observed (figure 3.1b).

#### 3.1.2.2 Zero-padding

The spatial information contained in  $S(\vec{x})$  is limited by the blurring of the PSF which is fixed by the length of the sampling window  $T = N \cdot DT$  [169]. For standard image reconstruction employing a discrete Fourier transform (DFT) directly on the acquired  $N$  data samples,  $N$  voxels with a inter-voxel distance of  $\Delta x = FOV/N$  are the result. The central datapoint of the intra-voxel course of  $S(\vec{x})$  represents the voxel intensity. By zero-padding (ZP, zero-filling, sinc-interpolation), the spatial intra-voxel course of  $S(\vec{x})$  can be acquired by adding additional sampling points to  $S(\vec{x})$ . Zero-padding is performed by adding zeros at the end of k-space before applying the DFT. For example, appending  $N/2$  zeros to the negative and  $N/2$  zeros to the positive k-space sample points refines the sampling of  $S(\vec{x})$  to an inter-voxel spacing of  $\Delta x/2$ . Following the arguments about the PSF mentioned above, no additional spatial information is gained through zero-padding. However, by incorporation of a priori knowledge about the cell, namely to search for the minimum of  $S(\vec{x})$  within a voxel, zero-padded images provide the information necessary to overcome the contrast reduction of the partial volume effect. If the grid is refined to an extent so that the cellular position matches the zero-filled image grid, the maximum contrast is sensed in the same way as if the cell was positioned directly on the native grid.

The approach followed by the presented work was:

- To refine the sampling grid up to the memory limits given by the reconstruction hardware.
- To search within the refined grid for the magnitude minimum within the native voxel volume.
- This signal intensity was chosen as the new voxel intensity of the native grid (= minimum intensity projection, MIP), therefore enhancing the negative contrast for deplaced single labeled cells.

### 3. AMPLIFICATION STRATEGIES FOR CELL TRACKING WITH CARTESIAN TRAJECTORIES

---

#### 3.1.3 Methods

##### 3.1.3.1 Simulations

Intra-voxel grid simulations were carried out as described by Lebel et al. [110] in order to simulate  $S(\vec{x})$  for different cellular iron loads. In detail, the transverse magnetization of  $7 \times 7 \times 7$  voxels with a voxel volume of  $(300 \mu\text{m})^3$  each and a total discretization of  $351^3$  sub-voxels were calculated based on equation 2.29. The local frequency offset  $\Delta\omega_{\vec{r}} = 2\pi\Delta f_{\vec{r}}$  for each sub-voxel at grid position  $\vec{r}$  was evaluated in dependence of the cellular load  $m_c$  (pg) of a single cellular perturber placed at the center of the simulation grid:

$$\Delta f_{\vec{r}} = \frac{\gamma}{4\pi} \frac{K_{Fe} m_c}{r^3} (3 \cos^2 \Theta - 1). \quad (3.2)$$

In the above equation,  $\gamma$  is the gyromagnetic ratio (MHz/T),  $K_{Fe} = 1.34 \cdot 10^{-19}$  T/(pg/m<sup>3</sup>) a calibration coefficient between iron load and effective magnetization [35],  $\Theta$  the polar angle relative to the direction of the main magnetic field  $B_0$  and  $r$  the distance from the center of the cell (m). The PSF was calculated given an unapodized, rectangular window in 3D [169] which results in a separable sinc-shaped PSF given at the sub-voxel positions  $(n_x, n_y, n_z)$  as  $PSF_{n_x, n_y, n_z} = \frac{\sin(\pi n_x / N_{sub})}{\pi n_x / N_{sub}} \cdot \frac{\sin(\pi n_y / N_{sub})}{\pi n_y / N_{sub}} \cdot \frac{\sin(\pi n_z / N_{sub})}{\pi n_z / N_{sub}}$  with  $N_{sub} = 25$  the total number of sub-voxels per voxel. In addition, the simulations performed accounted for off-resonant displacements in readout direction by shifting sub-voxel magnetization according to the local field-offset and readout bandwidth (320 Hz/pixel). Other simulation parameters were adapted to match the conditions of the in vitro experiment described next: TR = 11 ms, TE = 4.76 ms,  $T_1 = 1200$  ms,  $T_2 = 80$  ms,  $\alpha = 8^\circ$ ,  $M_0 = 1$ .

##### 3.1.3.2 In vitro experiments

Cells loaded with an average of 80 pg Fe (SPIO: Resovist) were diluted within 0.5 % agarose to reach a final concentration of 10 cells/ $\mu\text{l}$  and filled into a cylindrical 5 mm diameter cavity of a 50 ml agarose-filled tube. Cellular iron load was first determined with the susceptometric method described in [35] and section 2.2.3.4 on cellular samples taken from the same cellular patch. Isotropic 3D GRE datasets of the phantom were acquired on a 3 T clinical system using a volume coil for mice. A low-res  $(310 \mu\text{m})^3$

### 3.1 Enhanced contrast of single cells through zero-padding

---

scan (TA  $\approx$  5 min) with slab-selective excitation and TR = 11 ms,  $\alpha = 8^\circ$ , TE = 4.76 ms, matrix =  $160^3$ , 320 Hz/pixel and a high-res ( $148 \mu\text{m}$ )<sup>3</sup> scan (TA  $\approx$  48 min) with TR = 22 ms,  $\alpha = 12^\circ$ , TE = 9.06 ms, matrix =  $256^3$ , 320 Hz/pixel were acquired.

#### 3.1.3.3 Reconstruction

The rawdata of the 3D gradient echo acquisition (low-res) was processed in MATLAB (MathWorks Inc., Natick, MA, USA). Oversampling in readout direction was removed prior to data processing since the FOV covered the whole agarose-phantom. The final  $160^3$  point k-space was padded with zeros to reach a final matrix size of  $640^3$  (about 2 GB of memory in single precision) followed by a 3D FFT. Through zero-padding, a 4-fold refined imaging grid was therefore calculated and a minimum intensity projection of the gained 4 x 4 x 4 sample points per native voxel was calculated.

#### 3.1.4 Results

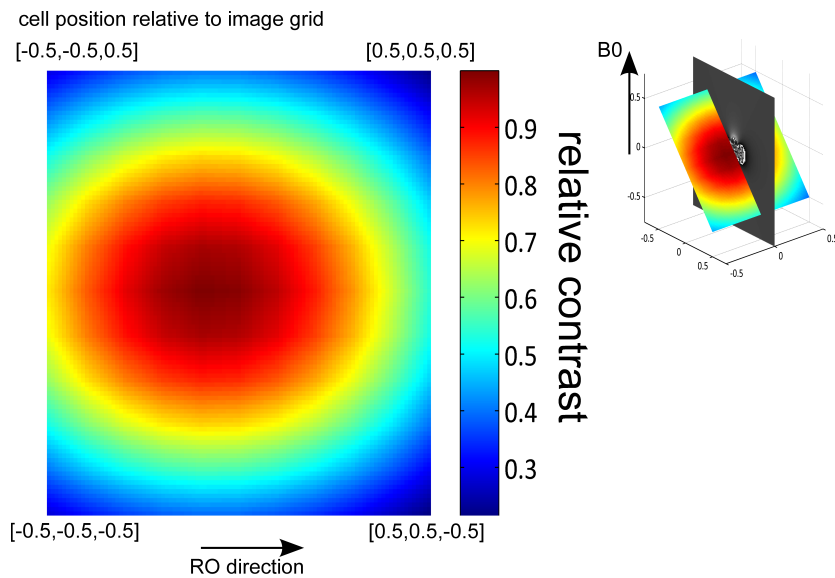
Figure 3.2 shows a loss in contrast in dependence of intra-voxel positioning of a 50 pg Fe loaded cell. The relative contrast depicted is defined as the fraction  $\Delta S/\Delta S_{max}$ , where  $\Delta S = S_{cell} - S_0$  is the absolute signal change to  $S_0$  (the background) in the presence of an iron loaded cell at a certain intra-voxel position of the cell and  $\Delta S_{max}$  is the maximum value of  $\Delta S$  within a voxel. Cellular displacements by 0.5 the voxel dimension within all 3 spatial directions  $[0.5, 0.5, 0.5]$  reduce the voxel contrast by up to 76 %. Apparently the contrast modulation additionally depends on the readout direction and the cellular intra-voxel shift along this direction. The different microscopic field offsets cause a displacement of the magnetization along the direction of the readout gradient depending on the used imaging bandwidth. Additionally, the sign and amplitude of off-resonances are linked to the direction of the main magnetic field  $B_0$  (equation 3.2). Therefore, slice orientation (orientational relation to the spatial field-pattern), readout direction (shift direction) and the chosen readout bandwidth (amount of shift to off-center frequency) contribute to the intra-voxel contrast course.

In order to simplify considerations on the effect of cellular mismatch with the grid, the analysis emphasized on the difference of the contrast maximum  $\Delta S_{max}/S_0$  and minimum  $\Delta S_{min}/S_0$  within a voxel irrespective of the exact locations. Figure 3.3a shows  $\Delta S_{max}/S_0$  and  $\Delta S_{min}/S_0$  for a range of intra-cellular iron concentrations. Figure 3.3b compares the gain in relative contrast  $(\Delta S_{max} - \Delta S_{min})/\Delta S_{min}$  if a cell at location

### 3. AMPLIFICATION STRATEGIES FOR CELL TRACKING WITH CARTESIAN TRAJECTORIES

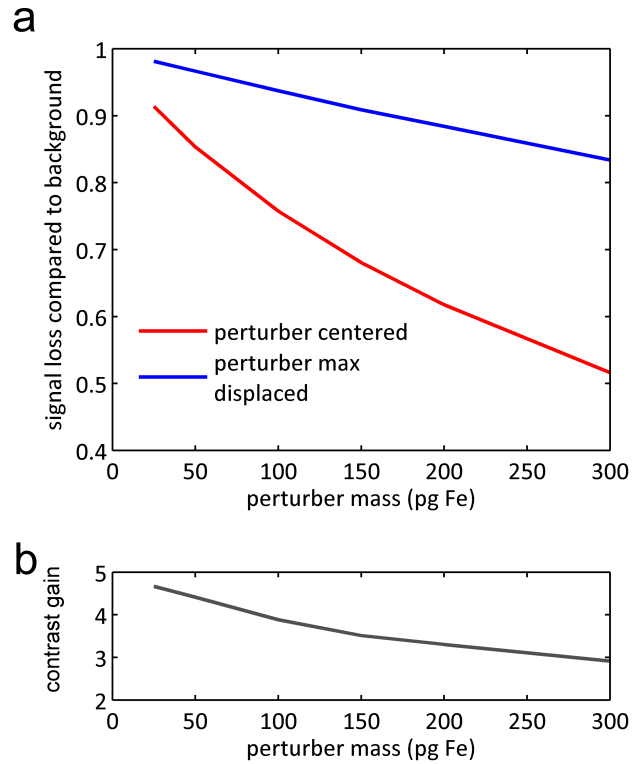
---

**Figure 3.2:** The relative cellular contrast  $\Delta S/\Delta S_{max}$  ( $\Delta S = S_{cell} - S_0$ ) calculated at different intra-voxel positions with respect to the highest cellular contrast  $\Delta S_{max}$  (perturber placed centered with respect to the imaging grid). The dipolar field of a 50 pg Fe loaded cell was used for simulation. The plot was made diagonal through the voxel in order to catch the points of maximum contrast loss for a displacement within all 3 directions of 0.5 times the voxel dimension (blue areas).



### 3.1 Enhanced contrast of single cells through zero-padding

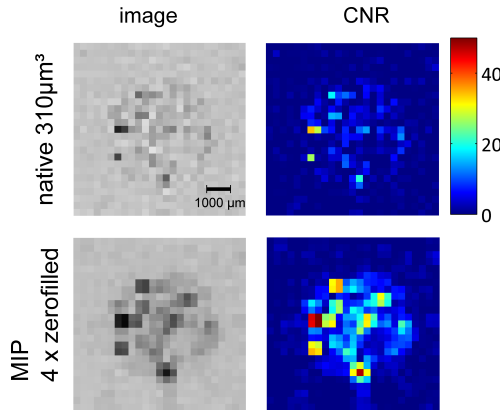
**Figure 3.3:** Simulated contrast for different intra-cellular iron oxide concentrations. **(a)** Relative signal decrease to background  $\Delta S/S_0$  for a voxel entrapping an iron oxide labeled cell positioned on the imaging grid (red) and for the case that the cell is placed exactly in between the grid (all 3 directions). **(b)** Relative contrast enhancement  $(\Delta S_{max} - \Delta S_{min})/\Delta S_{min}$  if a maximum displaced cell is imaged on the grid.



### 3. AMPLIFICATION STRATEGIES FOR CELL TRACKING WITH CARTESIAN TRAJECTORIES

---

**Figure 3.4:** top: original  $(310 \mu\text{m})^3$  GRE image and CNR plot; bottom: image + CNR values after minimum intensity projection of the zero-filled refined grid presenting enhanced perturber contrast.



with minimal contrast is matched to the imaging grid. The simulations reveal that the gain in contrast is best for small iron concentrations.

The ZP reconstruction delivers sampling points which are closer to the actual cellular position, therefore avoiding contrast loss. Figure 3.4 compares the gradient echo acquisition with a native resolution of  $(310 \mu\text{m})^3$  to a voxel-wise minimum intensity projection of the 4-fold ZP reconstruction. The ZP method shows cellular contrast not visible with the initial native reconstruction before.

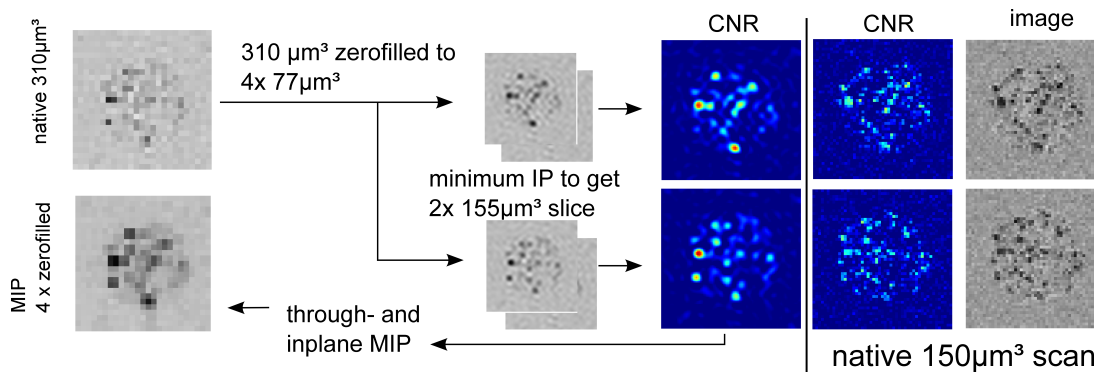
To substantiate the hypothesis that the new contrast originates from displaced perturbers, a comparison with a native 3D GRE with 2-fold higher resolution is shown in figure 3.5. Since the 4-fold ZP reconstruction of the  $(310 \mu\text{m})^3$  dataset consists of an interpolated grid with the spatial resolution of  $(\approx 77 \mu\text{m})^3$  the high-res zero-padded images were projected to  $155 \mu\text{m}$  slices by minimum intensity in order to make them comparable with the native  $(148 \mu\text{m})^3$  scan. The CNR maps of the gained two slices compared with the native  $148 \mu\text{m}$  slices show an excellent match of contrast.

#### 3.1.5 Discussion

Although no further gain in image information is provided by zero-padding, additional sample points allow for the detection of the voxel signal minimum caused by paramagnetic structures. A high contrast gain is predicted by simulations for perturbers with a low iron content. This observation is of major importance, since for in vivo appli-

### 3.1 Enhanced contrast of single cells through zero-padding

**Figure 3.5:** Comparison between the zero-filled MIP and a native  $(148 \mu\text{m})^3$  scan confirms the origin of the contrast enhancement from punctuate perturbers which had not been visible with the standard  $(310 \mu\text{m})^3$  reconstruction before.



cations the displacement may reduce the signal decrease of small particles below the noise-dictated detection threshold. The loss of contrast can be completely recovered by ZP reconstructions.

In addition, the simulations emphasized that the intra-voxel contrast course shows a dependency on the chosen imaging bandwidth visible by the smearing of contrast along the readout direction as shown in figure 3.2. This effect is known for strong magnetic dipoles like interventional devices [150, 170] where macroscopic field offsets modulate the contrast of neighboring voxels in readout direction. The same effect may have a significant relevance for the available contrast for small magnetic perturbers like cells. A purely hypothetical assumption based on this observation is that by using a higher image bandwidth a more concentrated (less shifted) intra-voxel phase dispersion may be produced which results in a higher absolute magnitude loss.

The in vitro data presented in this study tested the feasibility of cellular contrast enhancement analysing ZP images. A minimum intensity projection over  $4 \times 4 \times 4$  sample points of the 4-fold refined sampling grid enhanced the contrast for labeled cells remarkably. Cellular hypointensities invisible within the original  $(310 \mu\text{m})^3$  reconstruction but within the MIP of the 4-fold zero-filled dataset are clearly depicted within a native high resolution scan, indicating that many perturbers are far displaced from the original  $(310 \mu\text{m})^3$  grid. This result is further remarkable considering the 10-fold longer acquisition time for the high resolution scan and the comparable cellular detection capabilities both images deliver.

### 3. AMPLIFICATION STRATEGIES FOR CELL TRACKING WITH CARTESIAN TRAJECTORIES

---

## 3.2 Mapping field perturbations for cell tracking with positive contrast

### 3.2.1 Introduction

The aim of this study was to monitor iron oxide labeled progenitor cells within the target tissue of bone marrow. The bone marrow consists of trabecular boney structures with a very short intrinsic  $T_2^*$  which confine a dense network of blood vessels (which again amplifies  $R_2^*$ ), intra-trabecular water and a high concentration of fatty acids [171]. The heterogeneous structure of these components, each of them having a distinct magnetic susceptibility, give rise to an inhomogeneous static magnetic field environment [34, 37, 171, 172]. This results in an increase of the apparent relaxation rate  $R_2^*$  and a corresponding decrease in signal intensity in gradient echo imaging. While the signal decay originating from susceptibility differences may be used as a source of information for bone structure evaluation [37, 173, 174] it reduces background signal for cell tracking. Since the inhomogeneities are of static nature, the rephasing properties of the spin echo technique [26] allow for a comparable high background signal. However, rephasing local  $B_0$  inhomogeneities and sensing  $T_2$  rather than  $T_2^*$  reduces the sensitivity to signal degradation from small paramagnetic objects about 70-fold [35]. Therefore, new contrast mechanisms have to be employed which allow for a sensing of iron oxide labeled cells within bone marrow.

As mentioned in section 2.3.3, sequences producing positive contrast from paramagnetic particles help to overcome the specificity issues in cell tracking within target tissues of heterogeneous or low background signal.

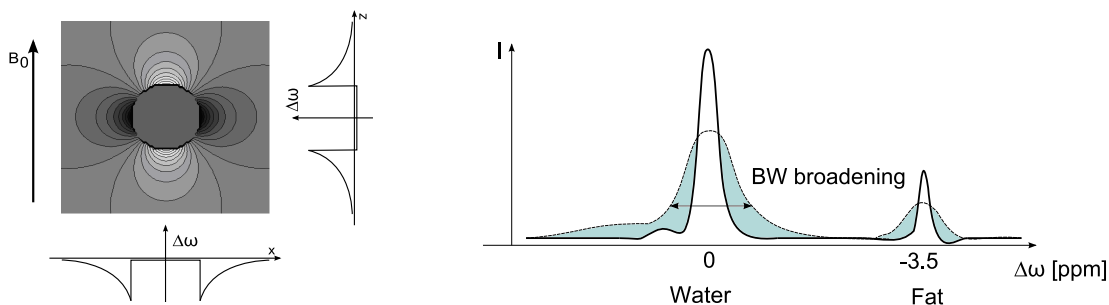
In this study, a novel approach for positive contrast, suggested by Stuber et al. [136], was adapted for the application in bone marrow and validated within an in vitro model of the ilium.

### 3.2.2 Theory

Imaging of iron oxides is based on their perturbation of the homogeneous main magnetic field  $B_0$ . Magnetization in close proximity to the cell experience a frequency offset  $\Delta\omega$  as schematically illustrated on the left in figure 3.6. As a result, the initial sharp lines of the NMR proton spectrum (solid line in figure 3.6 right) of surrounding tissue

### 3.2 Mapping field perturbations for cell tracking with positive contrast

**Figure 3.6:** Field map to the left and resultant proton spectrum to the right. The spherical structure in the left image causes field perturbations  $\Delta\omega$  which enlarge the half width at full maximum (BW broadening) of the proton NMR peaks of free and lipid bound protons.



experience a broadening visualized in blue in figure 3.6. This allows to differentiate between tissues free of any paramagnetic objects and off-resonant protons next to labeled cells by their spectral bandwidth (BW).

Stuber et al. introduced the idea of visualizing cells with positive contrast by adding on-resonant, spectrally selective radiofrequency pulses with limited bandwidth in advance to an imaging readout. These saturation pulses suppress on-resonant magnetization while off-resonant magnetization linked to the spectral broadening of labeled entities remains unaffected. The procedure creates a positive contrast in regions close to the cellular perturber as labeled in blue in figure 3.7 where the area of positive contrast can be controlled through the width  $BW_{sat}$  of the saturation. The main advantage of this technique over other positive contrast approaches is that the cellular contrast is produced by adding simple preparation pulses independent from the used imaging sequence. That implies the applicability to fast gradient echo techniques, spin echo or even time efficient turbo spin echo (TSE) readouts in 2D as well as in 3D [136].

The NMR spectrum of bone marrow contains a high fraction of lipid bound protons in the methylene groups ( $CH_2$ ) of fatty acids. The chemical environment of these protons shifts their appearance within the  $^1H$  spectrum about 3.5 ppm (with respect to the larmor frequency  $\gamma B_0$ ) upfield (towards a lower center frequency). If an NMR spectrum is acquired within bone marrow, a second peak visible on the right of figure 3.6 and 3.7 appears which originates from lipid bound protons.

The initial approach of Stuber et al. (IRON) intended to saturate on-resonant free unbound water while completely suppressing signal originating from lipid bound protons.

### 3. AMPLIFICATION STRATEGIES FOR CELL TRACKING WITH CARTESIAN TRAJECTORIES

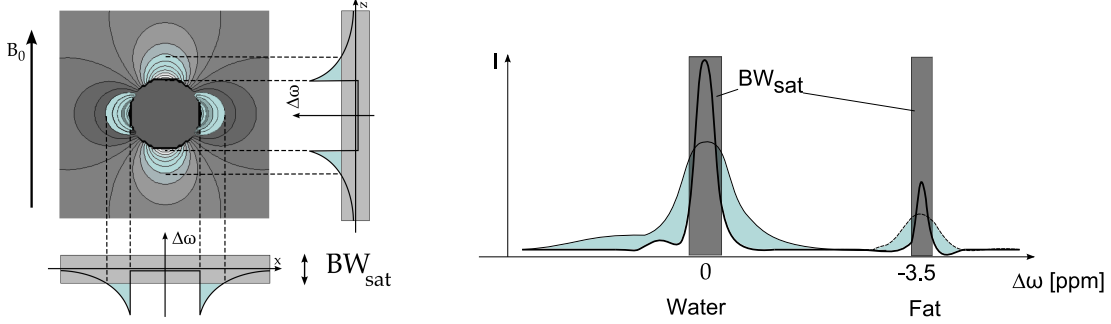


**Figure 3.7:** While saturating the on-resonant lipid and water bound protons by narrow bandwidth RF pulses with a bandwidth of  $BW_{sat}$ , the protons close to a paramagnetic perturber (blue) remain unaffected and can be used for positive contrast imaging.

Within this study, a second saturation pulse was applied for on-resonant protons at - 3.5 ppm which accounted for the high fraction of lipid bound protons in marrow. Therefore, protons in close proximity to paramagnetically loaded cells are imaged with positive contrast irrespective of their chemical bound. A fast spin echo, or RARE sequence, was selected for image readout based on the intrinsic advantage in imaging bone marrow concerning the available tissue background signal.

#### 3.2.3 Sequence development

##### 3.2.3.1 Saturation by inversion recovery

A  $180^\circ$  inversion pulse followed by a time delay  $TI$  can be proposed to an excitation pulse, known as inversion recovery experiment, to nullify a specific tissue with a distinct  $T_1$  relaxation time [131] if  $TI$  is set to

$$TI = T_1 \ln 2 = T_1 \cdot 0.693 \quad (3.3)$$

which is the solution of the equation describing longitudinal magnetization recovery

$$M_z(t) = M_0 \left[ 1 - 2e^{-t/T_1} \right] \quad (3.4)$$

for  $M_z(TI) = 0$  and  $M_z(0) = -M_0$ , the condition that the preceding inversion pulse has flipped the longitudinal magnetization from the  $+z$  axis to the  $-z$  axis. The inversion

### 3.2 Mapping field perturbations for cell tracking with positive contrast

---

recovery experiment of free protons within tissue is rather time consuming since  $T_1$  varies from  $\approx 800$  ms (liver) up to  $\approx 2000$  ms (blood) (numbers given for 3 T [156]). To nullify one of these components, several hundreds of milliseconds have to be reserved for magnetization preparation which accordingly prolongs TR. Lipid bound protons have a rather short  $T_1$  ( $\approx 380$  ms, 3 T [155]). Therefore, signal nulling of fat is quite popular with intermediate long inversion times, e.g. of 262 ms. The sequence timing may be further optimized if the flip angle of the spectral selective inversion is reduced from  $180^\circ$  to  $\theta_{inv}$ . The longitudinal  $M_z$  and transverse  $M_\perp$  magnetization after the inversion pulse is

$$\begin{aligned} M_z &= M_0 \cos \theta_{inv} \\ M_\perp &= M_0 \sin \theta_{inv} \end{aligned} \tag{3.5}$$

which reduces the time for longitudinal recovery

$$M_z(t) = M_0 \left[ 1 - (1 - \cos \theta_{inv}) e^{-t/T_1} \right] \tag{3.6}$$

and shortens the time delay  $TI$

$$TI = T_1 \ln(1 - \cos \theta_{inv}) \tag{3.7}$$

which nullifies the longitudinal component  $M_z(TI) = 0$ . To avoid interferences from stimulated echos [131] from  $M_\perp$ , additional spoiler gradients have to be applied.

The given formulas assume a total longitudinal recovery between the experiments. Hence, repetition time has to fulfill  $TR \gg T_1$ . Since spectral selective inversion pulses act on the whole imaging object, multiple slices have to be acquired in a sequential order to reach total proton relaxation for the inversion which results in a tremendously long scan time.

For slice interleaved data acquisition, where preparation pulses have to be played in front of the excitation of each slice, the actual repetition time for the inversion recovery is reduced to the length of the imaging readout plus the time for inversion  $TI$ . For a turbo spin echo experiment, the readout time corresponds to the inter echo time

### 3. AMPLIFICATION STRATEGIES FOR CELL TRACKING WITH CARTESIAN TRAJECTORIES

---

$TE_{int}$  multiplied with the turbo factor  $TF$ . This time period is denoted as  $T_{RO}$  with  $T_{RO} = TE_{int} \cdot TF$ . For fixed  $TI$ ,  $T_{RO}$ ,  $T_1$  and  $TI < T_{RO} < T_1$ ,  $\theta_{inv}$  for  $M_z(TI) = 0$  can be calculated:

$$\theta_{inv} = \arccos\left(\frac{1 - e^{TI/T_1}}{1 - e^{-T_{RO}/T_1}}\right). \quad (3.8)$$

A second method for spectrally selective signal nulling was used for the study: A saturation of protons with arbitrary  $T_1$  times can be achieved by a spectrally selective  $90^\circ$  (saturation-) pulse followed directly by the  $90^\circ$  excitation of the spin echo experiment (or fast turbo spin echo). At his approach it is assumed that both successively played  $90^\circ$  pulses flip the net magnetization within the saturation band back to  $M_z$ , and therefore, no transversal magnetization is produced.

#### 3.2.3.2 Narrow bandwidth inversion pulses

The RF pulses used within this study focus on chemical shift (CS) selective excitation. For CS RF selection,  $\Delta\omega$  is a function of the protons microscopic environment in their chemical compounds, for example the difference in resonant frequency of protons within the water molecule ( $H_2O$ ) to protons of the methylene groups ( $CH_2$ ) found within triglycerides (blood lipid). Due to dissipative mechanisms (spin-spin relaxation and local  $B_0$  field gradients), these resonant singlets have a certain bandwidth even if no magnetic particles are present. Hence, manipulating protons of a certain species requires an RF excitation pulse with a certain frequency response, most commonly a bandpass behavior with a desired spectral bandwidth  $BW_{sat}$ . To gain a distinct  $M_\perp$  and  $M_z$  state at a well defined frequency response is topic of RF pulse design and a brief overview is given next.

**Radiofrequency excitation - general issues** The goal of excitation is to flip the net stationary magnetization  $M_0$  into the  $B_0$  orthogonal transversal plane to get  $M_\perp = M_x + iM_y$ , or to a desired non equilibrium state of  $M_z$ . Within the following section, the direction of the polarizing field  $B_0$  is heading into  $\vec{e}_z$  and the RF excitation is chosen to be short in order that longitudinal as well as transversal relaxation during the time period of excitation can be neglected.

### 3.2 Mapping field perturbations for cell tracking with positive contrast

---

Assuming no initial transversal magnetization  $M_{\perp} = 0$  at the start of RF excitation and  $M_z = M_0$ , the resultant transversal magnetization over time if a RF pulse with magnitude  $B_1$  and the carrier frequency  $\omega_{RF} = \omega_0 = 2\pi\gamma B_0$  is switched on is described by [131, 175]

$$M_{\perp}(t) = i\gamma e^{-i\Delta\omega t} \int_0^t M_z(t') B_1(t') e^{i\Delta\omega t'} dt'. \quad (3.9)$$

The spectral response of  $M_{\perp}$  can be calculated as the Fourier transform of the envelope of the RF pulse  $B_1(t)$  if  $M_z$  is thought to be constant over time. This is a valid assumption for small tip angles where  $M_z(t) \approx M_0$ , but since the z component is reduced with the sine of the actual flip angle, the spectral response of an RF pulse with angles  $> 30^\circ$  can no longer be calculated with the Fourier transform. The aforementioned approximation is therefore called small-tip angle or linear approximation. For tip-angles larger than  $30^\circ$ , the spectral profile of a given envelope of RF excitation has to be calculated by the Bloch equations. Expressed in vector-matrix form

$$\frac{d\vec{M}}{dt} = R_{ex}\vec{M} \quad R_{ex} = \begin{bmatrix} 0 & \Delta\omega & 0 \\ -\Delta\omega & 0 & \gamma B_1(t) \\ 0 & -\gamma B_1(t) & 0 \end{bmatrix} \quad (3.10)$$

the solution is

$$\vec{M}(t) = e^{R_{ex}t} \vec{M}(t=0) \quad (3.11)$$

$$e^{R_{ex}t} = \mathbb{I} + R_{ex}t + \frac{1}{2}R_{ex}^2 t^2 + \dots$$

and can be calculated numerically if the final pulse shape is known and the spectral excitation profile is of interest. The opposite is called the inverse problem and is of non-trivial nature as discussed next.

**Shinnar-Le Roux selective excitation pulse design (SLR)** For flip angles much larger than  $30^\circ$  the inverse problem is much more difficult to solve. The applications of large flip angle excitation are wide-spread and the most prominent examples are the

### 3. AMPLIFICATION STRATEGIES FOR CELL TRACKING WITH CARTESIAN TRAJECTORIES

---

slice selective excitation ( $90^\circ$ ) and refocusing ( $180^\circ$ ) pulses as used in spin echo or fast spin echo techniques. One approach to calculate pulses with larger tip angles is the Shinnar-Le Roux or SLR method [176, 177, 178] used in this study. Other techniques that need to be mentioned are based on optimal control theory [179, 180, 181, 182] or the inverse scattering transform [183].

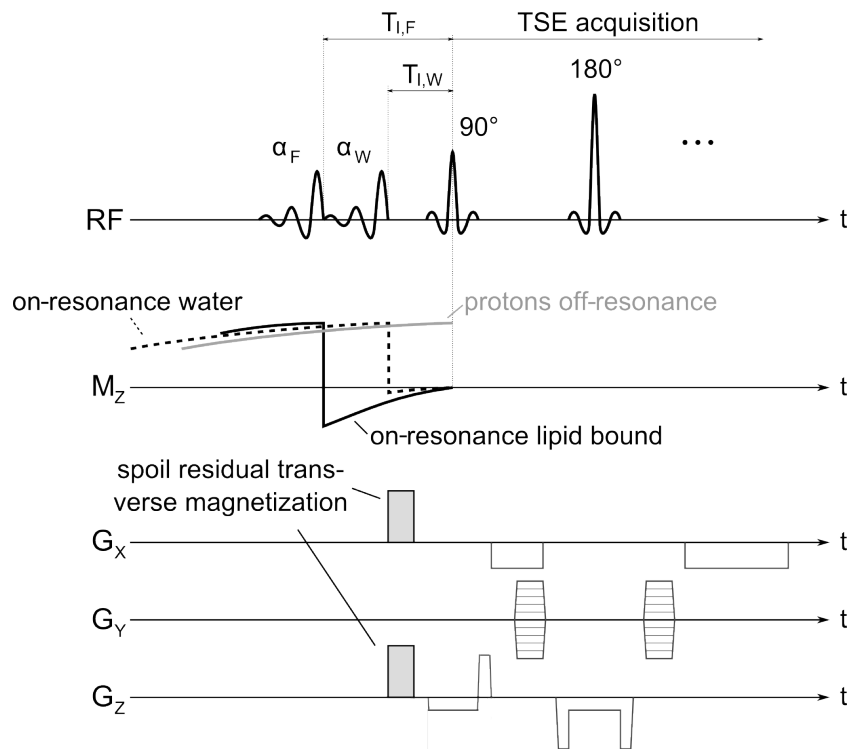
The principle idea of Shinnar and Le Roux is based on the hard pulse approximation where the RF pulse shape is discretized in a series of hard pulses (block-shaped RF pulse with constant magnitude). This condenses the design of the RF frequency response to well-established finite impulse response (FIR) filter design. The hard pulse sections are chosen to be as small as the small tip angle approximation  $\sin(\theta) \approx \theta$  is valid. For the time of these hard pulse sections, the nutation into the transversal plane as well as the rotation of the magnetization around the  $z$ -axis caused by  $\Delta\omega$  (free precession) are calculated. The SLR algorithm does not require the magnetization be fixed to a certain direction as is the case for equation 3.9 since the nutation and free precession for each hard pulse are expressed by rotation matrices. The SLR transform states that if a polynomial  $B_n(z)$  can be found which has a transfer function matching the desired spectral response of the RF pulse, the corresponding excitation pulse profile can be calculated by the inverse SLR transform. Thereby, a stepwise calculation of the RF properties (magnitude and phase) for each discretized segment is gained through a backward recursion of the polynomial  $B_n(z)$  defined by RF power and phase constraints. An exact description of the SLR transform and its inverse is given in the corresponding appendix A.1.

#### 3.2.3.3 Sequence timing

The new pulse sequence consists of two narrow bandwidth RF pulses to suppress water and fat followed by a turbo spin echo acquisition. A scheme of the pulse sequence is presented in figure 3.8. On-resonant (0 ppm) components usually occupy a broad range of  $T_1$  values, while lipid bound protons shifted by - 3.5 ppm are reported to have a rather well defined  $T_1$  value in the range of  $\approx 360 - 390$  ms (De Bazelaire et al.:  $382 \pm 13$  ms [155]; Gold et al.:  $371 \pm 8$  ms [184], all at 3 T). Hence, for the proposed saturation of two bands, a  $T_1$  selective approach based on equation 3.8 was used for fat whereas for free on-resonant protons a  $90^\circ$  saturation pulse without any time delay was implemented. The second row in figure 3.8 schematically describes the principle of

### 3.2 Mapping field perturbations for cell tracking with positive contrast

**Figure 3.8:** Dual band pulse sequence diagram including radiofrequency (RF) pulses, the longitudinal magnetization ( $M_z$ ) and gradients ( $G_x$ ,  $G_y$ ,  $G_z$ ). Preparation pulses  $\alpha_F$  and  $\alpha_W$  null longitudinal magnetization of on-resonance water and fat components, respectively, and leave the SPIO-induced off-resonant parts unaffected. These are consecutively imaged by a turbo spin echo readout.



### 3. AMPLIFICATION STRATEGIES FOR CELL TRACKING WITH CARTESIAN TRAJECTORIES

---

signal nulling of unperturbed (areas far away from paramagnetic structures, e.g. cells) free and lipid bound water components through inversion recovery and saturation respectively, supported by additional spoiling gradients which eliminate phase coherence of transverse components. Calculating  $\theta_{inv}$  for fat based on the readout timing  $T_{RO}$  allowed for a very efficient sampling scheme reducing  $TI$  and allowed for interleaved multi slice turbo spin echo readouts.  $T_{RO}$  of the turbo spin echo was fixed to 150 ms within the experiments and the turbofactor was adopted to match  $TF = T_{RO}/TE_{int}$  in order to provide flexibility for the resolution-dependent inter echo spacing  $TE_{int}$ .

#### 3.2.4 Methods

##### 3.2.4.1 RF pulse design

With MatPulse, a SLR RF pulse design tool based on MATLAB (Center for Imaging of Neurodegenerative Diseases, US, SF), pulses with bandwidths ranging from  $BW_{sat} = 75$  Hz to  $BW_{sat} = 375$  Hz were created with an inband/outband ripple of 1 % / 0.1 % and a pulse duration of  $T_{exc} = 100$  ms. The long pulse duration was required to match the spectral quality constraints (inband/outband ripple) which are inherently limited by the used time-bandwidth product  $T_{exc} \cdot BW_{sat}$  [185] of the pulse. In order to determine an effective inversion time, minimal phase pulses were designed where the majority of magnetization is flipped at the end of the excitation period. Hence, for the calculation of the inversion timing, the end of the saturation pulse was taken as the point of inversion. The flip angle for fat suppression  $\theta_{inv} = 170^\circ$  was gained through equation 3.8 according to the  $T_1$  relaxation time of 370 ms and the repetition time for the partial inversion  $T_{RO} = 150$  ms. The fat inversion time of  $TI = 105$  ms was mainly determined by the time of on-resonant water saturation which was played in between fat inversion and TSE excitation. The flip angle for water was set to  $92^\circ$  to account for the time delay between water saturation and the excitation center caused by gradient spoiling.

##### 3.2.4.2 RF excitation profile measurements

The quality of the spectral saturation profile was investigated within a uniform water phantom. The water saturation pulse and spoiler gradients were added preceding a spin-echo readout. During RF saturation a gradient field along the readout direction

## **3.2 Mapping field perturbations for cell tracking with positive contrast**

---

was switched on encoding 1500 Hz over 15 cm. With the scan parameters TR = 10,000 ms, matrix = 512, TE = 10 ms and a FOV of 15 cm the spectral saturation was determined by measuring the intensity profile in readout direction at a resultant spectral discretization of 2.9 Hz.

### **3.2.4.3 NMR of the ilium**

To quantify the needed linewidths for on-resonant suppression,  $^1\text{H}$  single voxel spectra were acquired within four different regions of the iliac crest of a human pelvis in vivo. 10 averages of the  $10 \times 10 \times 10 \text{ mm}^3$  voxels were acquired without any preceding suppression pulses. TR was set to 10,000 ms. The fraction between free and fat associated signal was analyzed by the integral over a bandwidth of  $\pm 123 \text{ Hz}$  ( $\pm 1 \text{ ppm}$  of the water larmor frequency) at 0 Hz (free water at a chemical shift offset of 4.7 ppm) and - 420 Hz (methylene at 1.2 ppm).

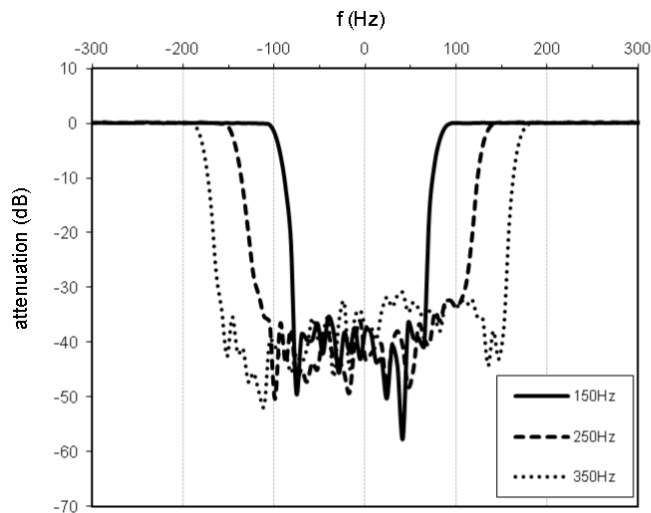
### **3.2.4.4 In vitro measurements**

The dual saturation TSE sequence was implemented on a 3 T clinical scanner and the scans were performed using a human wrist coil. A freshly isolated ilium of a pig was used for in vitro validation. After labeling endothelial progenitor cells over 24 hours within a 0.3 mg Fe/ml SPIO (Resovist) solvent, different cellular concentrations (0/5000/10000/20000/40000) were suspended in phosphate buffered saline (PBS) and injected into  $10 \mu\text{l}$  (2 mm diameter) drill holes. A baseline for the detection limit was determined by the signal of pure PBS and the positive contrast produced by the field-inhomogeneities of the drill hole. The on-resonant saturation bandwidth was chosen to be 250 Hz and 150 Hz for on-resonant water and fat respectively. Other scan parameters were: TR = 1210 ms; TE = 11 ms; turbo factor (TF) = 14; 3 slices of thickness = 2 mm; FOV =  $108 \times 108 \text{ mm}^2$ ; matrix =  $256^2$ ; acquisition time = 20.8 s. For a comparison to the IRON sequence, the spectral selective pulse was interchanged by a non-spectral selective Gaussian inversion pulse of fat, while all other sequence parameters remained unchanged. In order to provide comparability with the cell tracking gold standard of negative contrast GRE, a 2D GRE multi-echo acquisition was performed with the parameters: TR = 100; TE = 4.92 ms, 12 echos with an inter-echo spacing of 7 ms, three slices of thickness = 2 mm; FOV =  $135 \times 180 \text{ mm}^2$ ; matrix =  $154 \times 256$ ; Acquisition time = 41.2 s.

### 3. AMPLIFICATION STRATEGIES FOR CELL TRACKING WITH CARTESIAN TRAJECTORIES

---

**Figure 3.9:** Measured signal attenuation gained by saturation with narrow bandwidth SLR pulses. Within the desired RF pulse transition band of 150/250/350 Hz, background signal is suppressed by -40 dB.



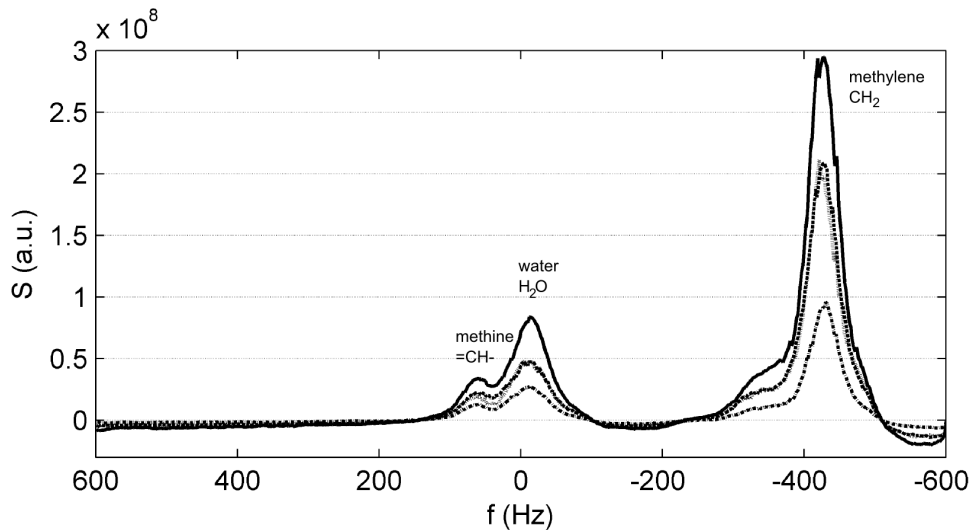
#### 3.2.5 Results

**Saturation efficacy** Measurements of the spectral profiles presented in figure 3.9 gained by saturating a uniform water phantom with the implemented SLR saturation pulses show an excellent suppression of on-resonant components and a steep transition band between the saturated and non-saturated spectral bands.

**$^1\text{H}$  spectroscopy in bone marrow**  $^1\text{H}$  single voxel spectroscopy of four representative areas within a human iliac crest were acquired. The analyzed voxels show a high amount of lipid bound protons with a mean of  $68\% \pm 2.3$ . The high fat-fraction causes an enlargement of the 0 Hz (4.7 ppm) peak, since about 10% of fat-associated protons are bound to methine ( $=\text{CH}-$ ) with a chemical shift offset next to free water at 5.3 ppm [186]. The resultant broadening of the on-resonant water peak is reflected in the calculated half-width at full maximum of the 0 Hz line with  $64.5 \pm 3.3$  ppm in comparison to  $44.5 \pm 2.1$  ppm (at -420 Hz, resp. 2.1 ppm chemical shift) of fat. The bandwidth for the on-resonant saturation pulse of water was therefore chosen to be larger than the fat saturation bandwidth. According to the half-width measurements given above, the ratio between fat- and water-associated protons was determined as

### 3.2 Mapping field perturbations for cell tracking with positive contrast

**Figure 3.10:**  $^1\text{H}$  in vivo spectra acquired in four different regions of a human pelvis reveal a high fraction of lipid bound protons. Protons bound to methine considerably enlarge the water NMR peak.



1.5:1.

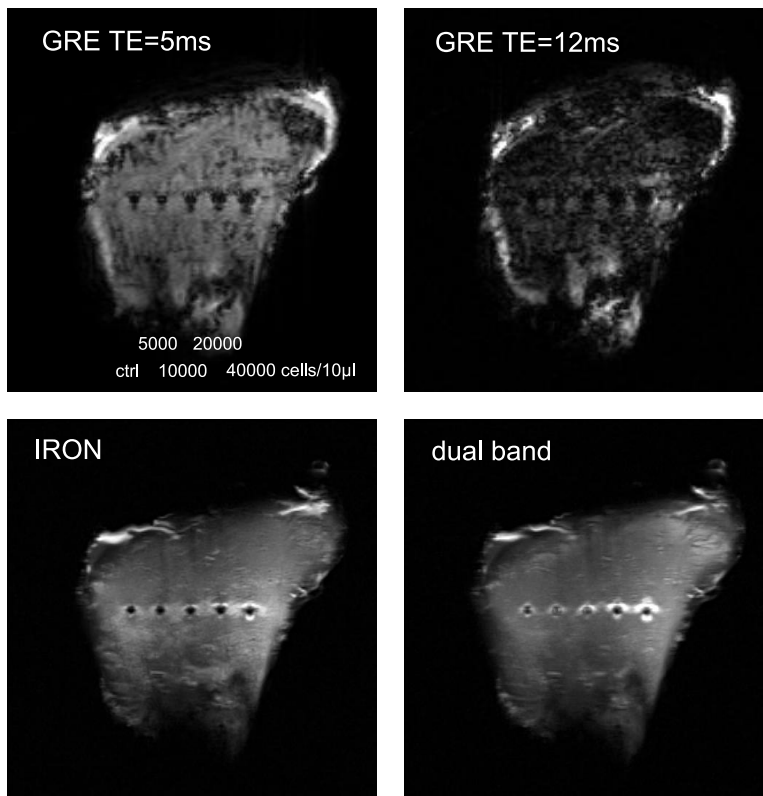
**In vitro measurements** Figure 3.11 shows a comparison of the acquired images through gradient echo, IRON and the proposed dual band positive contrast technique. The drawbacks of negative contrast in red marrow visible in the two images in the top row are clearly visible. The background signal decreases dramatically with increasing TE while it is difficult to differentiate between dark structures in bone marrow and the negative contrast of labeled cells. An apparently better discrimination of cellular contrast to tissue background is delivered by the new dual band approach compared to the negative contrast of GRE. Despite a positive contrast enhancement that is already visible with the IRON technique, more hyperintense contrast is gained with the dual band sequence by adding additional signal from protons bound to fat.

Evaluating the mean signal around the cellular samples within a  $10 \times 10$  pixel region of interest (figure 3.12) consolidates the observations from the images. The sensitivity over cell concentration is considerably higher for the two positive contrast techniques compared to GRE. While IRON and the novel technique show a comparable sensitivity to iron concentration, their detection limits differ. The dual band technique already allowed to encode a sample of 5000 cells with positive contrast, while IRON first exhibited

### 3. AMPLIFICATION STRATEGIES FOR CELL TRACKING WITH CARTESIAN TRAJECTORIES

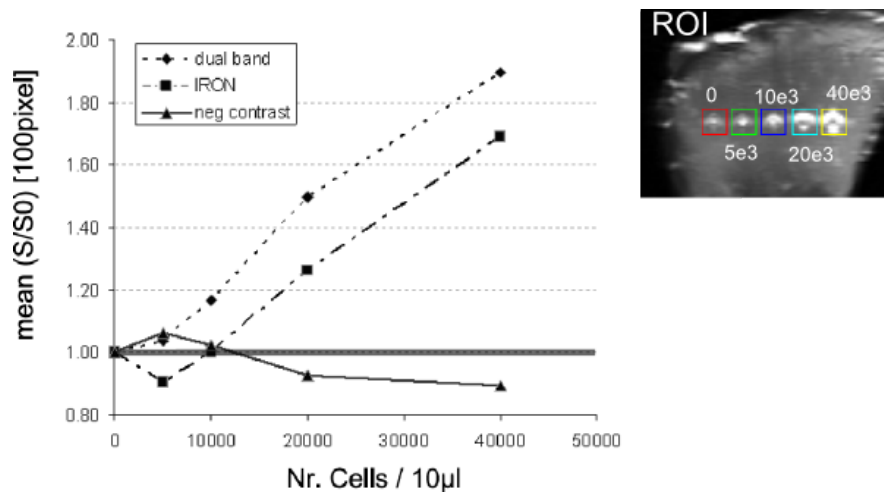
---

**Figure 3.11:** Comparison of the cellular contrast of GRE, IRON and the proposed dual band saturation technique within bone marrow of an isolated ilium of a pig. Central to the ilium, five 2 mm diameter cavities have been filled with 0/5000/10,000/20,000/40,000 SPIO labeled endothelial progenitors. The negative contrast of the labeled cells gained through standard spoiled GRE imaging become undistinguishable from the heterogeneous marrow background at later echo times TE. The IRON sequence, which is based on a turbo spin echo readout, delivers a homogeneous background signal throughout the ilium. Voxels close to the cell containing drill holes gain hyperintense contrast at the IRON sequence. In contrast to the new dual band technique, lipid bound protons are saturated and not used for the generation of cellular contrast. Utilizing the high concentration of lipid bound protons in marrow for positive contrast generation through the dual band technique leads to an additional gain in cellular signal.



### 3.2 Mapping field perturbations for cell tracking with positive contrast

**Figure 3.12:** Contrast quantification of GRE acquisition (negative contrast), positive contrast IRON technique and the proposed dual band saturation sequence. The background  $S_0$  for calculating the relative signal change plotted ( $S/S_0$ ) is determined by the 10 x 10 pixel ROI centered to the cavity containing PBS buffer only (red box labeled with 0). Comparable cellular contrast sensitivity (slope of relative signal change vs. cellular concentration) is gained by the two positive contrast techniques, albeit the dual band technique allowed to identify a lower amount of labeled cells (5000) through hyperintense contrast.



### 3. AMPLIFICATION STRATEGIES FOR CELL TRACKING WITH CARTESIAN TRAJECTORIES

---

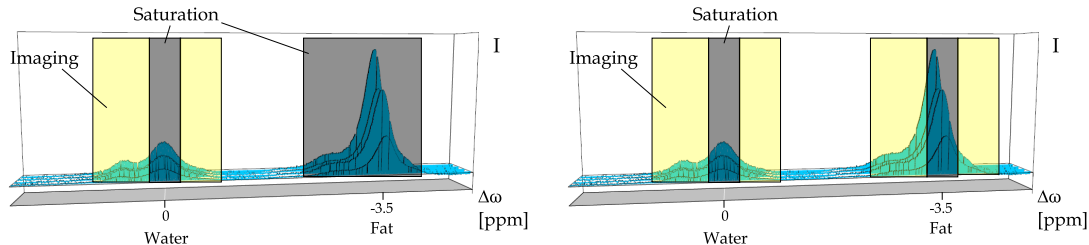


**Figure 3.13:**  $^1\text{H}$  spectra within the ilium and spectral bands saturated by IRON (left) and the proposed dual band technique (right) shaded in gray. Saturation of the lipid bound protons as in IRON would discard valuable signal for positive contrast imaging in comparison to the dual band technique.

positive contrast for a sample containing 10000 labeled cells.

#### 3.2.6 Discussion

The implemented MR sequence depicts areas in close proximity to iron oxide-labeled cells with bright signal, facilitating a well distinguishable positive cellular contrast. Instead of saturating fat as done by the IRON sequence [136], the implemented technique additionally utilizes the high concentration of lipid bound protons in bone marrow (figure 3.13) via two minimal phase SLR pulses, one for on-resonant water and one for on-resonant fat. Following this approach, the detection limit is reduced to a lower number of iron loaded cells required for detection.

However, there are issues concerning the specificity of the sequence originating from the inherent high sensitivity of non-iron related global  $B_0$  shifts. An example is given by the contrast of the first drill hole containing the unlabeled control in figure 3.11 which exhibits more positive contrast than the labeled 5000 cells sample. This contrast most likely originates from an additional global frequency shift caused by the the proximity of the border to air combined with the hole's intrinsic susceptibility difference to marrow. While this observation is related to the design of the phantom it manifests  $B_0$ -related problems which may occur in vivo, for example for areas next to the lungs or for subcutaneous applications.

While the background suppression delivers satisfactory results in well shimmed regions, the background at the border of the ilium is not completely suppressed and gives false

### **3.2 Mapping field perturbations for cell tracking with positive contrast**

positive contrast. This appears to be due to a global shift in resonant frequency, excluding some of the water/fat protons from saturation by the narrow bandwidths of the pulses.

In summary, the aforementioned limitations of the saturation techniques are opposed by their very short acquisition times ( $\approx 20$  s vs.  $\approx 40$  s of 2D GRE) and their desirable positive contrast in bone marrow compared to 2D gradient echo acquisitions. However, they are not able to produce positive contrast directly at the cellular injection site and detection limits are far above the single cell level.

### **3. AMPLIFICATION STRATEGIES FOR CELL TRACKING WITH CARTESIAN TRAJECTORIES**

---

4

## Cell tracking with 3D radial UTE

### 4.1 Introduction to radial MRI

The radial image readout, or projection acquisition (PA), was the core of Paul C. Lauterbur's invention [187] about the zeugmatography technique which is nowadays known as the foundation of MRI. Radial acquisitions fill k-space with radial spokes rather than with a rectilinear grid as known from *Cartesian sampling* [131]. The acquired lines are Fourier transformed spin-density projections of the object in the direction of the magnetic field gradient used for readout. Despite the historical importance, PA was quite soon replaced by Cartesian 2D and 3D *Fourier imaging* or *spin-warp* technique by Richard R. Ernst [188]. Rectilinear or Cartesian sampling has some intrinsic advantages over radial acquisitions due to the mathematical simplification of image reconstruction through the fast Fourier transform (FFT) of k-space (Richard S. Likes [189]) and the stability to gradient imperfections. However, there are desirable advantages of PA compared to FT imaging:

- superior stability against motional artifacts
- potential for extremely short echo times
- intrinsic averaging through oversampling of low spatial frequencies

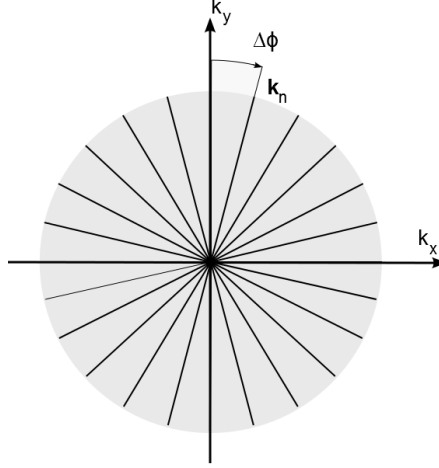
The aforementioned aspects, highly appreciated for ultra-fast imaging techniques [190, 191] and uprising MR applications at rapidly decaying environments [192, 193, 194], fast rectilinear regridding procedures and improvements in the accuracy of state of the art gradient systems led to a growing interest in radial MRI over the past decade.

#### 4.1.1 Acquisition of radial data

Radial projection acquisition gathers data along polar spokes where each spoke passes through, or starts, at the k-space origin and traverses radially through k-space to the outermost radius  $k_{max} = N/(2FOV)$ , determining the chosen FOV and desired resolution  $N$ . For 2D PA, the direction of the readout gradient  $G_{RO}$  in  $\vec{e}_x$  and  $\vec{e}_y$  is changed by each TR to acquire full k-space coverage

$$\begin{aligned} G_x &= G_{RO} \sin \phi_n \\ G_y &= G_{RO} \cos \phi_n \end{aligned} \tag{4.1}$$

**Figure 4.1:** 2D k-space of radial projection acquisition.



with  $\phi_n$  the polar angle at acquisition  $n$

$$\phi_n = n\Delta\phi \quad |_{n=0..N_S-1} \quad (4.2)$$

and the polar angle increment

$$\Delta\phi = 2\pi/(N_S - 1) \quad (4.3)$$

where  $N_S$  is the total number of radial spokes or projections and half-echo acquisition assumed. There is no need for phase encoding since the continuous change in readout direction with each TR

$$\vec{e}_{k_n} = \begin{bmatrix} \sin \phi_n \\ \cos \phi_n \end{bmatrix} \quad (4.4)$$

encodes  $k_x$  and  $k_y$  by the readout gradient itself as depicted in the k-space sampling trajectory in figure 4.1. This specific feature gives rise to the popularity of radial acquisitions for ultra-short TE imaging further described in section 4.2.

A 3D radial trajectory is designed in a similar manner, but in addition,  $G_{RO}$  has to trace projections in  $\vec{e}_z$ . The 3D spokes are equally distributed over 3D k-space, and

#### 4. CELL TRACKING WITH 3D RADIAL UTE

---

solutions for choosing polar ( $\phi$ ) and azimuthal ( $\theta$ ) projection angles fulfilling equidistant sampling on a spheres' surface are described by Glover et al. [195] (for the acquisition of concentric rings around  $\vec{e}_z$ ) and by Wong and Roos [196] (spiral-like sampling).

##### 4.1.2 Nyquist criterium in radial MRI and the effect of undersampling

For radial imaging, the acquisition time is determined by a desired degree of artifact-free reconstruction and the amount of radial spokes required to accomplish the latter. The full nyquist sampling of k-space defines the distortion-free case where no aliasing artifacts occur. To fulfill nyquist, the distance in between the most distant k-space points have to satisfy the criterion [131]

$$k_{max}\Delta\phi \leq \frac{1}{FOV} \quad (4.5)$$

in 2D and

$$k_{max}^2\Delta\Omega \leq \frac{1}{FOV^2} \quad \text{with} \quad \Delta\Omega = \sin\theta\Delta\theta\Delta\phi \quad (4.6)$$

in 3D. Out of that, the needed radial spokes  $N_{Sn}$  for full nyquist sampling can be calculated as

$$N_{Sn} = \pi N \quad (4.7)$$

for 2D and

$$N_{Sn} = \pi N^2 \quad (4.8)$$

for 3D trajectories [131], half-echo and equal-solid-angle sampling [197]. If the number of radial spokes  $N_S$  is reduced below the nyquist limit, frequently referred to as angular undersampling, aliasing in the form of streaks across the image occur. It is important to keep in mind that angular undersampling does not reduce the final image resolution as long as the extent of k-space  $k_{max}$  is not reduced. Compared to Cartesian sampling, where undersampling yields shifted replicas (nyquist ghosts) of the image along the

phase encoding direction, aliasing streaking artefacts (azimuthal aliasing) of radial MRI are often hard to identify through visual inspection and aggravate image interpretation. At constant angle radial MRI, the artifact-free representation of an object depends on its spatial extent. If the ratio between its size and the FOV is not larger than the k-space extent fulfilling the nyquist criterium in equations 4.5 and 4.6 to  $k_{max}$ , no aliasing within the object will occur [198]. The artifact-free distance is calculated as

$$r_{max} = FOV \cdot \frac{N_S}{N_{Sn}}. \quad (4.9)$$

This certainly does not imply that objects smaller than  $r_{max}$  do not cause azimuthal aliasing, but rather do the produced streaks appear at a distance of ( $r_{max}$ ) from the signals generating the streak. A popular application to radial undersampling is aneography [198], where subtraction images from a time series are used to eliminate streaking artifacts from static background, while vessel information, much smaller than the sampled nyquist limit, are free from artifacts.

### 4.1.3 Reconstruction

With the central slice theorem, the radial projections can be reconstructed either by filtered back-projection as described in CT literature (e.g. [199]) or through gridding [200] to a rectilinear grid preposed to an inverse FFT (IFFT). The approach of re-gridding allows for the reconstruction of arbitrary placed k-space points, and hence arbitrary k-space trajectories, which makes the technique more flexible compared to back-projection. Another difference between the techniques is their computational efficiency. The reconstruction time for a 2D PA with matrix size  $N$ ,  $N_S$  spokes and an oversampling factor of 2 is  $N_S N 2w$  for regridding with  $w$  the gridding kernel width (usually 2..4), compared to  $N_S N^2$  for filtered backprojection [131]. A comprehensive comparison of the PSF and SNR of both techniques can be found in [201].

At gridding, the arbitrarily placed k-space points are mapped to an equidistant grid through a convolution with a kernel  $W$ . Subsequently, the regridded Cartesian k-space dataset is transformed to image space with the inverse Fourier transform. Although for unapodized finite sampled rawdata the ideal convolution kernel would be an infi-

## 4. CELL TRACKING WITH 3D RADIAL UTE

---

nite sinc function, the best approximation through a wide extent is the Kaiser-Bessel window [202] as discussed in [203]:

$$W(k) = \frac{\sin \sqrt{\pi^2 w^2 k^2 - \beta^2}}{\sqrt{\pi^2 w^2 k^2 - \beta^2}}. \quad (4.10)$$

Within the above expression,  $\beta$  is a free design parameter chosen to minimize aliasing artifacts depending on the window width  $w$ . Best choices for  $w$  and  $\beta$  are given in [203].

An issue inherent to radial sampling is that the density of k-space points vary over k-space. A straightforward convolution with a kernel of constant shape over areas with different density yields an amplification of low spatial frequencies where the radial spokes cross at  $k = 0$ , as well as a reduced magnitude of high spatial frequency components where the spokes diverge. This results in a considerably blurred image. However, since the sample density is known, this unwanted scaling behavior can be undone through weighting the rawdata with their area density preceding the IFFT, first described by Jackson et al. [203]. The density compensation for equidistant sampled radial data is an unapodized linear ramp (2D) or quadratic (3D) filter:

$$\rho(k)_{2D} = |k| \Delta\phi \quad \text{and} \quad \rho(k)_{3D} = |k|^2 \Delta\Omega. \quad (4.11)$$

Finally, the reconstructed image  $S(x)$  of arbitrary sampled k-space points  $S(k)$  via gridding can be calculated as

$$S(x) = \text{IFFT} \{ (S(k)\rho(k)) \star W(k) \} \quad (4.12)$$

with  $\star$  the convolution.

### 4.1.4 Features of radial sampling for preclinical MRI

#### 4.1.4.1 Background SNR and SNR of reduced acquisitions

As mentioned before, projection acquisitions gather a high sampling density in the mid of k-space contrary to Cartesian acquisitions which fill k-space uniformly. Besides the

magnitude enhancement which is addressed by density compensation, radial sampling modifies the noise spatial-spectral density [197]. The crossing of radial spokes at the k-space origin lead to a  $1/|k|$  redundancy of 2D PA acquired samples. If each k-data includes an uncorrelated noise term with zero mean, averaging through the gridding function  $W(k)$  will tend to an increased image SNR of gross features encoded in the central k-space [197]. This results in an increased SNR for large-scaled organs which is very desirable for low-SNR preclinical MR imaging.

Fullfilling nyquist,  $N_{Sn}$  for polar sampling causes a factor of  $\pi$  prolonged acquisition time compared with Cartesian sampling. Therefore, angular undersampling is often desired, which gives rise to the question how reduced acquisitions scale SNR. For the SNR of 2D PA the following relation can be concluded [201]

$$SNR \simeq \frac{\sqrt{3T_{acq}NN_S}}{2\sigma} \quad (4.13)$$

if noise is equally distributed over the ADC sampling time  $T_{acq}$  and consists of Gaussian additive noise with a standard deviation of  $\sigma$ . Interpreting this formula, SNR scales with the square root of acquired spokes and bandwidth used, e.g. enlarging  $T_{acq}$  by using a higher image matrix  $N$  at the same gradient strength (enhancing the FOV) enhances SNR. However, as discussed earlier this introduces an additional grade of streaking artifacts since the undersampling ratio  $N_S/N_{Sn}$  decreases. If full projections are acquired, azimuthal aliasing can be reduced while keeping a high SNR (through enhancing  $N$  in parallel to a reduction in  $N_S$ ) by the use of a mixed gridding and back-projection reconstruction algorithm proposed by Lauzon and Rutt [201] or, more general and applicable to half-projections, by constrained iterative reconstruction frameworks [204].

#### 4.1.4.2 Image artifacts due to motion

Radial MRI has inherent advantages over Cartesian sampling with respect to inter- and intra-shot motion. The regime of intra-shot motion defines movements of the spin ensemble during the timeframe of excitation, encoding and readout of a single k-space line while inter-shot motion defines movements taking place over succeeding TR's, and hence, through the acquisition of different k-space lines. As a consequence, both regimes

#### 4. CELL TRACKING WITH 3D RADIAL UTE

---

differ in their timescales and sensitivity to different motional sources. As the inter-shot time is usually not larger than some milliseconds, only fast moving spins such as vessel blood flow give rise to artifacts. The inter-shot timescale spans throughout the whole acquisition of k-space, hence the inter-shot regime is most sensitive to large bulk motion such as respiratory or cardiac motion.

**Intra-shot motion** In general, the phase accrued by spins moving with a constant velocity is determined by the 1<sup>st</sup> order moment of the gradients (the integral over time of the product of the gradient and time) [197]. When the 1<sup>st</sup> order moment is non-zero, unwanted motion leads to phases that can cause signal loss and image ghosting. For sequences such as half-echo acquisitions, where the acquisition starts near or at the centre of k-space, there is relatively little gradient-on time before passing through the centre of k-space. Thus, the 1<sup>st</sup> order moment at this point in time is low, and flow-induced motion is suppressed [197].

**Inter-shot motion** Inter-shot motion give rise to inconsistencies between different k-space lines. While in fourier imaging this results in a dispersion of image information along the phase encoding direction, the oversampling of low-spatial frequencies in PA averages through inconsistencies and therefore reduces motional artifacts [197]. While motion in projection imaging propagates in parallel to the readout direction which changes from TR to TR, the energy of moving spins is spread out in all directions rather than one as in phase-encoded Fourier imaging.

## 4.2 3D UTE

### 4.2.1 Introduction

MRI of strong magnetic perturbers in the static dephasing regime causes a signal degradation of the imaging voxels as discussed in section 2.1.3.2. The trabecular bone structure of the marrow causes additional signal degrading as described in [34]. Compared to standard gradient echo based SPIO imaging, the paradigm changes to smaller echo times in order to gain a reasonable contrast-to-noise ratio. Figure 4.2 depicts the impact of different background scenarios on cell contrast. Figure 4.2f points out that echo times shorter than 1 ms are required in order to detect labeled cells within tissues with short  $T_2^*$ . Acquiring images with echo times below 1 ms is commonly known under the name of ultra-short TE (UTE) acquisition. Several technical implementations can be found in literature, and the ones most commonly used are zero TE imaging [205, 206], SWIFT [207] and radial ultra-short TE imaging with k-space sampling during gradient ramp-up [208, 209, 210, 211]. A comprehensive comparison of zero TE and SWIFT techniques can be found in [212, 213]. Clinical applications are wide spread and are found in imaging of cartilage, tendons, lung, breast and dental MRI.

The aims of this study were:

- To implement a gradient echo based ultra-short time to echo sequence on a clinical 3T MRI.
- Compare the UTE approach to gold-standard gradient echo techniques with respect to scan time and motional artifacts.
- Present an in vivo application to subcutaneously injected SPIO labeled cells.

### 4.2.2 Sequence development

#### 4.2.2.1 K-space trajectory

A center-out - center-in k-space trajectory as sketched in figure 4.3 was implemented on a 3T whole body scanner (MAGNETOM Skyra and Trio, Siemens Healthcare, Erlangen, Germany). Core of the sequence is a global (hard) RF excitation without any slice selective gradient. Therefore, after excitation, all spins are in-phase and data acquisition is started immediately. Global RF pulses excite all the magnetization accessible

#### 4. CELL TRACKING WITH 3D RADIAL UTE

**Figure 4.2:** Beads of 50,000, 10,000 and 1000 SPIO loaded cells in a homogeneous agarose gel background are imaged with a spoiled gradient echo acquisition at TE = 5 ms (a) and TE = 10 ms (b). The control consists of 50,000 unlabeled cells. The cellular contrast enhances for later echo formations and homogeneous (long  $T_2^*$ ) tissue background (c). The shaded area in (c) presents the contrast between labeled cells and background ( $T_{2\text{agar}}^* = 200$  ms,  $T_{2\text{cells}}^* = 5$  ms). Within the heterogeneous background of bone marrow (as an example, 10,000 labeled cells in the ilium of a pig are shown), the cellular contrast vanishes with late TEs (d,e). In order to enhance the contrast for cells in fast decaying background tissues such as bone marrow (simulated  $T_{2\text{marrow}}^* = 10$  ms in f), echo times below 1 ms are required (yellow line in f).

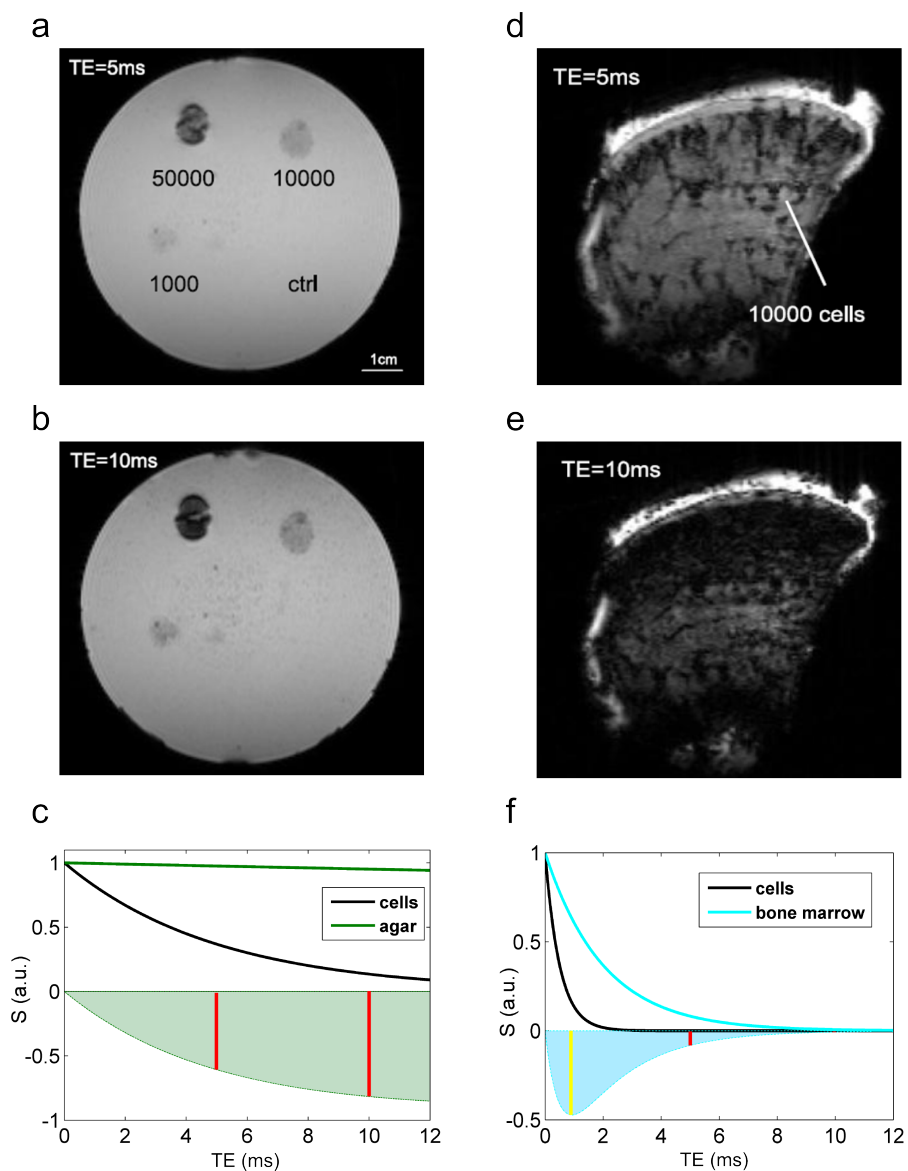
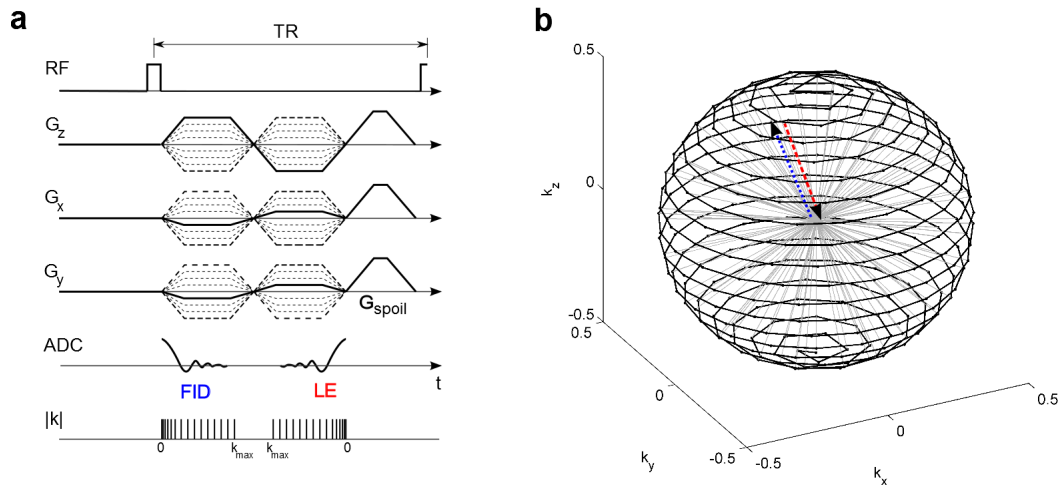


**Figure 4.3:** 3D UTE pulse sequence diagram (a) and k-space trajectory (b). Directly after a non-selective hard pulse excitation (first row in (a)), the readout gradient is ramped up and FID data acquisition starts (ADC in (a)). Sample points acquired at gradient ramp-up (200-300  $\mu$ s) show a higher sampling density in k-space (last row in (a)) due to a reduced gradient strength during that period of time. The projectional direction changes from TR to TR in order to cover k-space in a helical manner (black trace in (b)). In addition to RF-spoiling, a gradient spoiler in x, y and z is employed to destroy residual transverse magnetization. Following FID sampling, a second echo (late echo, LE) is generated by a reversed gradient following the FID acquisition.



#### 4. CELL TRACKING WITH 3D RADIAL UTE

---

by the transmit coil. Accordingly, spatial encoding is handled solely by the readout gradient. To enable 3D spatial encoding, the readout direction is changed from TR to TR. The actual readout direction is described by polar ( $\phi$ ) and azimuthal ( $\theta$ ) angles and a helical pathway (fig. 4.3b) which uniformly covers 3D space is given by [196]

$$\vec{e}_{k_n} = \begin{bmatrix} \sin \theta_n \cdot \cos \phi_n \\ \sin \theta_n \cdot \sin \phi_n \\ \cos \theta_n \end{bmatrix} \quad (4.14)$$

with

$$\begin{aligned} z_n &= \frac{2n - 1 - N_S}{N_S} \\ \theta_n &= \arccos z_n \\ \phi_n &= \left[ \phi_{n-1} + \pi / \sqrt{N_S/2 \cdot (1 - z_n^2)} \right] \pmod{2\pi}. \end{aligned} \quad (4.15)$$

Again,  $N_S$  is the total number of half-echos acquired and  $n$  the actual acquisition number.

##### 4.2.2.2 Non-uniform sampling during gradient ramp-up

The free induction decay (FID) originally describes the process of free precession and relaxation of the magnetization after excitation of the spins into the transversal plane. In UTE imaging, the acronym is used for the acquisition directly after excitation, even though the readout gradient is played out for image acquisition and therefore, the 'free precession' has already undergone a forced resonance shift corresponding to the spatial encoding. Since the abbreviation FID is generally used in literature for pulse sequences which acquire an image directly after excitation with k-space center-out trajectories, it is used further on in this work.

If ADC samples are acquired with a constant dwell time, sampling of the FID during gradient ramp-up results in a radial non-equidistant sampling of k-space. The spatial frequencies acquired are defined by the time integral of the gradient strength

$$k(t) = \gamma \int_0^t G_{RO}(\tau) d\tau \quad (4.16)$$

with  $G_{RO} = G_x + G_y + G_z$ . With the gradient ramp-up time  $t_{RU}$  defined by the slew-rate  $SR$  (in mT/m/ms) and the final readout gradient field strength  $G_0$

$$t_{RU} = \frac{G_0}{SR} \quad (4.17)$$

the gradient function is defined as

$$G(t) = \begin{cases} SRt & 0 \leq t \leq t_{RU} \\ G_0 & t_{RU} < t \end{cases} \quad (4.18)$$

resulting in the corresponding spatial frequencies  $k(t)$ :

$$k(t) = \begin{cases} \frac{1}{2}\gamma SRt^2 & 0 \leq t \leq t_{RU} \\ \gamma G_0 \left(t - \frac{t_{RU}}{2}\right) & t_{RU} < t \end{cases} . \quad (4.19)$$

Hence, k-space sample spacing during ramp-up follows a quadratic behavior. To avoid magnitude amplification at lower spatial frequencies, the a priori knowledge of the gradient waveshape has to be included in the density compensation discussed in the reconstruction section 4.1.3. A second observation of equation 4.19 is that in order to sample equal image resolution  $\Delta x = 1/k_{max}$  compared with constant gradient acquisitions at  $G_0$ , the sampling and gradient duration for ramp-up acquisitions have to be prolonged by  $t_{RU}/2$ . Sampling with different k-space velocities has an additional impact on the apparent acquisition SNR. Pipe and Duerk [214] showed that the noise variance for ramp-up sampling is slightly increased compared to constant gradient sampling. However, the authors stated that because of the additional sampling time ( $+t_{RU}/2$ ), the SNR drop is balanced by the additional acquisition time which increases SNR.

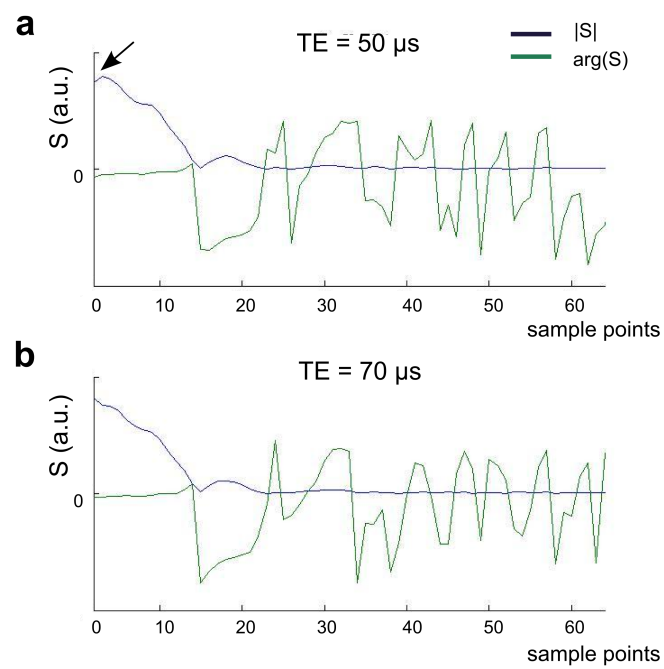
#### 4.2.2.3 Transmit/receive switching delay

The center-out k-space trajectory allows for an immediate data acquisition, and hence a TE of 0. Nonetheless, since the receive coils have to be decoupled from the transmit field during excitation, there is a switching delay between transmit and receive. The

#### 4. CELL TRACKING WITH 3D RADIAL UTE

---

**Figure 4.4:** Half echo acquired at time to echo of  $50 \mu\text{s}$  (a) and  $70 \mu\text{s}$  (b). The magnitude of the first ADC sample point at  $\text{TE} = 50 \mu\text{s}$  shows a signal degradation (arrow) compared to  $\text{TE} = 70 \mu\text{s}$  caused by an incomplete switching of the receive chain.



receive coils are decoupled through PIN diodes fed through an RF-blocked (inductance commonly  $> 10 \mu\text{H}$ ) DC path. Hence, to deliver the PIN diodes with the needed reverse voltage in order to switch into receive mode, some  $\mu\text{s}$  pass. State of the art MRI systems have transmit/receive dead-times of about 50 - 100  $\mu\text{s}$ . An example for an imperfect decoupled system and the data received is given in figure 4.4. A practical value for the time delay required to acquire the first undamped sample point was about 70  $\mu\text{s}$  at the wide-bore system used throughout the presented work.

Another time delay is introduced by the used digital bandpass filter limiting the received signal to the FOV used. For a given bandwidth, a minimum filter length is required which leads to a signal buildup duration which depends on the filter order while data passes through the digital filter. A more detailed insight on filter dependent receiver delays is given in [212]. According to the technical data provided by the vendor of the MRI machine (Siemens Healthcare, IDEA Discussion Board/Documents/Customer/07 Freiburg/Presentations/03 Radial Calibration Peter Speier), this time delay is calculated as

$$\Delta t = \frac{1}{BW \cdot f_{OS}} + b \quad (4.20)$$

with  $b = 0.8 \cdot 10^{-6}$  s, a system type dependent time delay,  $BW$  the total image bandwidth and  $f_{OS}$  the oversampling factor (for 3D radial imaging at least 2-fold). From this formula it follows that for most image bandwidths, the sampling dwell time  $1/BW$  is in general larger than  $\Delta t$ . Hence discarding the first sample point turned out to be a practical value for the system used throughout the presented work.

#### 4.2.2.4 Corrections for gradient imperfections

As discussed earlier, the trajectory in k-space is defined by the readout gradient field over time (Eq. 4.16). The exact knowledge of the gradient shape, and hence k-space position, for each ADC sample point allows for image reconstruction through regridding in the first place (Sec. 4.1.3). For a misaligned k-space trajectory, the positions of acquired data differ from the intended ones. This results in reconstruction errors and a blurred image representation. Most artifacts obtained with PR trajectories arise from discrepancies in k-space center between the acquired spokes [215], e.g. through

#### 4. CELL TRACKING WITH 3D RADIAL UTE

---

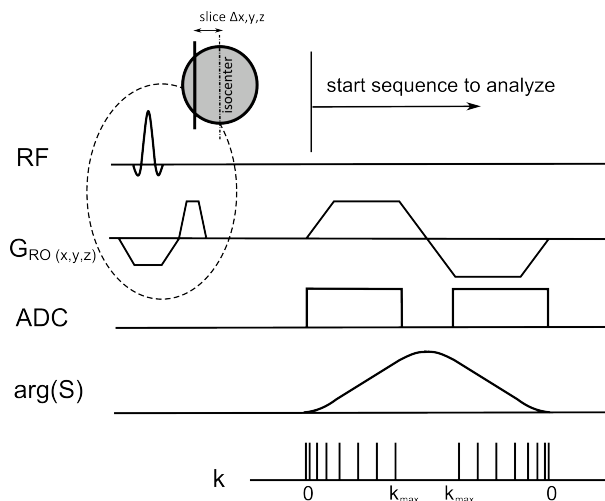
deviations between the actual and requested starting times of gradient waveforms [215], or from variations in gradient shape due to eddy currents [216].

Full-echo radial acquisitions can be corrected for gradient delays by measuring the difference in position of the maximum peak value from the intended center of k-space [215]. However, this cannot be performed for half-echo FID acquisitions which start sampling at  $G_{RO} = 0$ , and hence the first data point always yields maximum signal independent of any gradient delay.

Another challenge for center-out trajectories is that k-space center is acquired during gradient build-up rather than during a constant steady state of the gradient system. Switching magnetic field gradients induce eddy currents in conducting structures such as cryostat shields, Faraday screens and shim coils [217]. These currents will produce magnetic fields opposed to the gradient fields, unintentionally changing the predetermined gradient waveshape. For the most dominant conducting structures of an MR system, the multiexponential behavior of eddy currents is characterized during the construction of the system. This allows for an effective eddy current compensation by adding an overshoot to the waveform of the pulsed gradient, the so-called preemphasis. Since every conducting structure may lead to eddy current fields, the preemphasis cannot be unconditionally perfect. For example, different RF-coils will introduce different eddy current fields and even their positioning will influence eddy current behavior.

Gradient delays and eddy current related deviations of FID acquisitions can be determined either by performing separate measurements preceding the image sequence [216] or, as presented in a recent publication by Ianni et al. [218], through iterative joint estimation of images and k-space trajectory errors estimating trajectory errors by maximizing data consistency between k-space shots in regions where k-space is oversampled - as inherently done in the k-space center by the radial trajectory.

**k-space trajectory measurements** To correct for gradient imperfections, an approach by Duyn et al. [216] was followed. Hereby, k-space trajectory is measured directly through separate acquisitions presented in figure 4.5. For a given readout direction  $\vec{e}_n$  to be measured (where  $\vec{e}_n$  are the main gradient axes in  $\vec{e}_x$ ,  $\vec{e}_y$  and  $\vec{e}_z$ ), a thin slice with a known distance  $\Delta r$  away from the gradient iso-center is excited by a slice selective gradient in  $\vec{e}_n$  through a  $90^\circ$  RF pulse. Subsequently, this excited spin

**Figure 4.5:** Schematic of k-space measurement.

ensemble undergoes the readout gradient  $G_{RO_n} = G_{RO}\vec{e}_n$  from the sequence to be analyzed. During that period, the ADC is switched on and the phase is measured. For a distance  $\Delta r$  much larger than the excited slice thickness, the phase angle  $\phi_n$  has a direct relation to the actual sampled k-space position as

$$\phi_n(t) \hat{=} \gamma \cdot \Delta r \int_0^t G_{RO_n}(\tau) d\tau = \Delta r \cdot k_n(t) \quad (4.21)$$

with  $k_n = k \cdot \vec{e}_n$ . Rewriting equation 4.21 yields the true k-space evolution for the gradient encoding axis in  $\vec{e}_n$  determined through the measurement:

$$|k_n(t)| = \frac{\phi_n(t)}{\Delta r}. \quad (4.22)$$

A second slice selective scan with all the imaging gradients switched off eliminates for eddy current related effects from slice selection by the subtraction of both acquisitions. Depending on the slice position  $\Delta r$  and the readout gradient amplitude  $G_{RO}$ , phase wraps may occur but are easy to correct for as long as the slice is placed within the imaging FOV covered by the imaging bandwidth ( $\Delta\phi$  in between two sample points are then always smaller than  $\pi$ ). After determining  $k_n(t)$  for the three main readout axes (x, y, and z) it is assumed that for an arbitrary spoke  $i$  with polar and azimuth angles

## 4. CELL TRACKING WITH 3D RADIAL UTE

---

$\phi_i$  and  $\theta_i$  the resultant real k-space positions for the 3D k-space are given by a linear combination of  $k_x(t)$ ,  $k_y(t)$  and  $k_z(t)$ :

$$\vec{k}_i(t) = \begin{bmatrix} k_x(t) \cdot \sin \theta_i \cdot \cos \phi_i \\ k_y(t) \cdot \sin \theta_i \cdot \sin \phi_i \\ k_z(t) \cdot \cos \theta_i \end{bmatrix}. \quad (4.23)$$

The calculated k-space positions are used in the non-uniform FFT reconstruction (section 4.1.3) facilitating regridding at the actual true k-space trajectory. The method described is able to correct for eddy currents and gradient amplitude inconsistencies. Corrections for spatial gradient nonlinearities are not covered but may be included by measurements at various  $\Delta r$  [216] or single volume selective experiments.

### 4.2.3 Methods

#### 4.2.3.1 In vivo cell tracking model

**Cell culture and labeling** Endothelial colony-forming progenitor cells (ECFCs) were selected because studies with labeled ECFCs have shown no decrease in viability and functionality in a wide range of iron concentrations [101, 219]. Animal serum was replaced by human platelet lysate in all experiments [220]. Large scale propagation was performed as demonstrated previously in an online video tutorial [221]. Cryopreservation of aliquots for repeated experimental use were carried out as specified previously [222]. Cell labeling was performed with a clinically applicable SPIO Resovist (Bayer Vital GmbH, Leverkusen, Germany). Appropriate SPIO uptake was achieved by incubating sub-confluent cells with 3  $\mu\text{g}/\text{ml}$  protamine sulfate in addition to 200  $\mu\text{g}/\text{ml}$  of the SPIO for 24 hours. These concentrations were comparable to previously established protocols [59, 67]. The iron load per cell was quantified using the susceptometric method described by Bowen et al. [35]. The cells reached an average iron content of 48 pg/cell.

**Cell implantation** To demonstrate the in vivo performance of the investigated protocols, ECFCs and MSCs were mixed (ratio 4:1) and applied subcutaneously into the flanks of an immune-deficient NSG mouse. To test the MR cell tracking performance, it was the aim to label only a minor fraction of the applied cells. Therefore, 1.6 million unlabeled ECFCs and 0.4 million unlabeled MSCs were mixed with 0/400/2000/10,000

(0/1.5/7/35 labeled cells/ $\mu\text{l}$ ) SPIO-labeled ECFCs in ice-cold extracellular matrix (Milipore) before application. The injection sites (left/right to the lungs with 0/35 labeled cells/ $\mu\text{l}$  and left/right to the pelvis with 1.5/7 labeled cells/ $\mu\text{l}$ ) were chosen in order to show the impact of respiratory motion on the used sequences. Anesthesia during imaging was achieved with Isoflurane (1.4% in 100% Oxygen, flow 1.8 l/min). Animal experiments were approved by the Animal Care and Use Committee at the Veterinary University of Vienna on behalf of the Austrian Ministry of Science and Research according to the Guide for the Care and Use of Laboratory Animals.

#### 4.2.3.2 In vivo imaging

The aim was to study in vivo cell visualization capabilities of the 3D radial UTE sequence based on the mouse model described before. The laboratory animal was successively imaged by the cell tracking gold-standard sequences 2D and 3D spoiled gradient echo followed by the implemented 3D UTE sequence. The scans were performed on a 3T clinical scanner with a dedicated whole body coil for mice. The acquisitions shared the same in-plane resolution of  $(160 \mu\text{m})^2$  and the number of slices was chosen in a way that all 3 sequences covered the same imaging volume. The 3D radial scan was performed with an undersampling ratio of 0.64. The measurement parameters are summarized in table 4.1. Imaging was performed 14 days after cellular implantation.

**Table 4.1:** Measurement parameters for the UTE in vivo experiment.  $\alpha$  = flip angle; NEX = number of excitations (averages).

	TR	TE	$\alpha$	slice thk.	matrix	FOV	NEX	time
	(ms)	(ms)	( $^\circ$ )	(mm)		(mm)		(min:sec)
2D GRE	18.0	7.4	15	1.5	320x240x32	50x38	4	9:12
3D GRE	19.0	7.9	15	0.3	256 <sup>2</sup> x160	41x41	3	38:54
3D UTE	20.0	0.1/5.0	12	0.16	320 <sup>3</sup>	50x50	1	43:41

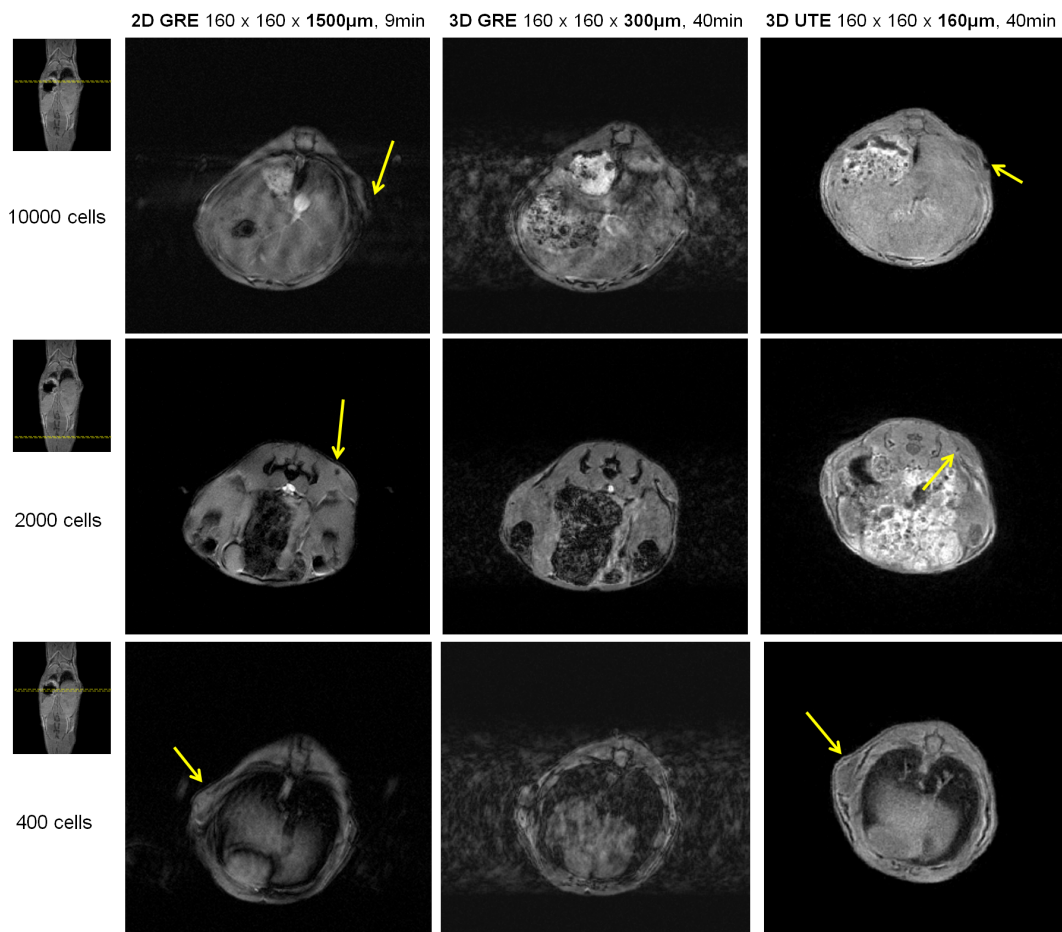
#### 4.2.4 Results

Figure 4.6 presents in vivo images acquired with 2D GRE, 3D GRE and 3D UTE, in the left, middle, right column respectively. The rows from top to bottom show injection sites

#### 4. CELL TRACKING WITH 3D RADIAL UTE

---

**Figure 4.6:** Panels compare 2D and 3D gradient echo acquisitions (1<sup>st</sup> and 2<sup>nd</sup> column) with the 3D UTE sequence (3<sup>rd</sup> column). Representative slices from the three injection sites (1<sup>st</sup> row: 10000 cells, 2<sup>nd</sup> row: 2000 cells and 3<sup>rd</sup> row: 400 cells) are shown. The yellow arrows point at the negative contrast produced by the cells. 3D GRE suffers from severe image artifacts in regions with respiratory motion, whereas the 2D GRE delivers quite reasonable images in all 3 cases. Nonetheless, 2D GRE with a 10-fold larger slice thickness compared to the 3D UTE sequence will fail to detect single labeled cells. A very unique feature of the UTE sequence is the applicability in tissues such as bone marrow (see boney structures of the pelvis in 2<sup>nd</sup> row) as well as in areas closed to air/tissue boundaries (1<sup>st</sup> row).



of 10,000 cells (close to liver), 2000 cells (near pelvis) and 400 cells (next to the lungs). To guide the eye, a yellow arrow labels the cellular negative contrast. 3D GRE suffers from severe image-artifacts in regions of respiratory motion, whereas the 2D acquisition, although not artifact free, keeps motional artifacts to an acceptable range at the three injection sites. As visible in the middle row, only the UTE sequence generates bright background signal within the pelvis. In addition, no motional artifacts - even in regions next to the lung parenchyma - are visible in the UTE images. Air/tissue boundaries are responsible for background signal degradation within the 2D GRE acquisition (directly at the injection site of the 10,000 cells, first row) which is absent in the UTE images.

#### 4.2.5 Discussion

The presented images show that the ultra-short time to echo formation in conjunction with 3D radial sampling is able to reduce almost all destructive motion artifacts known from Cartesian sampling. Nevertheless, UTE imaging has to deal with a reduced cellular CNR in bright homogeneous background tissue (see fig. 4.2c) compared to the  $>5$  ms TE of the gradient echoes. The reduced contrast, dictated by the available phase dispersion at  $100 \mu\text{s}$  TE, is opposed to the general benefit of the intrinsic isotropic resolution of the 3D UTE acquisition. The high image resolution of  $(160 \mu\text{m})^3$  enhances the contrast to small perturbers of 10 -  $100 \mu\text{m}$  in scale especially if the labeled cells are sparsely distributed where the contrast of a single cell has to be detected. 2D scanning techniques with manifold larger voxel volumes have a reduced total voxel phase dispersion, and hence contrast, if a single compact perturber is present. Additionally, in the particular case of a single labeled cell, an absolutely artifact free homogeneous background signal is required. This prerequisite is especially not satisfied by 3D GRE acquisition due to the unavoidable respiratory motion of the laboratory animal and the artifacts which come along. 2D GRE techniques, although more suitable when the subject under investigation is in motion, are prone to signal degradations caused by  $B_0$  inhomogeneities due to through-slice phase dispersions. As a result of the isotropic resolution of 3D UTE, and thus minimal global  $B_0$  variations within an image voxel, and the ultra-short echo time of  $100 \mu\text{s}$  presented, UTE imaging is insensitive to global  $B_0$  inhomogeneities. All in all, the artifact free background representation of UTE is beats the loss in cellular CNR.

However, high resolution 3D radial scanning is far more time consuming. While 3D near

#### 4. CELL TRACKING WITH 3D RADIAL UTE

---

isotropic Cartesian imaging has at least the same claims on scanning time, motional artifacts become even more severe because of the additional phase encoding direction compared to Cartesian 2D acquisitions.

In summary, the success of a cell tracking study based on gradient echo based imaging depends on the following aspects: the local concentration of iron oxides, the homogeneity of the background signal where the cells should be detected and the motion closed to the region of interest (e.g. respiration). For all three acquisition strategies presented, only the UTE sequence offers an artifact free image with bright homogeneous background signal in all tissues, even in bone marrow. Therefore, UTE imaging seems to be a powerful tool for stem cell imaging and may for the first time enable the detection of iron oxide nanoparticle labeled stem cells in bone marrow.

5

## Cell tracking with 3D radial UTE trajectories in coherent steady state

## 5. CELL TRACKING WITH 3D RADIAL UTE TRAJECTORIES IN COHERENT STEADY STATE

---

### 5.1 bSSFP imaging with half-echo acquisition

#### 5.1.1 Introduction

The inherent advantages of the fully balanced state concerning the high SNR due to the preservation of transversal magnetization (section 2.3.2) is highly appreciated for high resolution MR imaging. However, the complex  $T_2/T_1$  contrast and the sensitivity to global off-resonances manifested in the TR dependent banding artifacts are the reason why bSSFP acquisitions are more popular in large FOV (hence short TR), fast cardiac MRI studies [223, 224, 225]. The large gradient moments required for encoding high resolution images prolonge TR significantly, and hence, the applicability of bSSFP for high resolution applications depends on the possible reduction in TR.

Compared to Cartesian trajectories, time for phase encoding can be omitted in radial bSSFP acquisitions (section 4.1.1). If 3D radial projections are acquired, no slice selection gradient has to be played out and very short non-selective RF excitation can be employed [226] - both together significantly reduce TR.

Within this study, an acquisition technique is proposed which further reduces TR by employing 3D radial sampling with two half-echoes. The balanced steady state contrast of the proposed two echoes is investigated and an in vivo application of fast, high-resolution MR imaging on clinical hardware is presented.

Major aims of the study were:

- To investigate tissue contrast of half-echoes acquired directly after and before excitation and compare their image contrast to centered-echo bSSFP.
- To show that the SNR per unit measurement time of the new technique is improved compared to standard bSSFP acquisitions.
- To present an in vivo application to analyze
  - the gain in banding artifact reduction through TR reduction.
  - cell tracking performance at subcutaneously implanted SPIO labeled cells.

#### 5.1.2 Theory

Common bSSFP acquisitions use a centered full-echo, gained in the middle of the TR interval. The full-echo sampling requires a k-space trajectory starting at  $-k_{max}$  evolving to  $+k_{max}$ . Considering the phase coherence required to reach the balanced steady

## 5.1 bSSFP imaging with half-echo acquisition

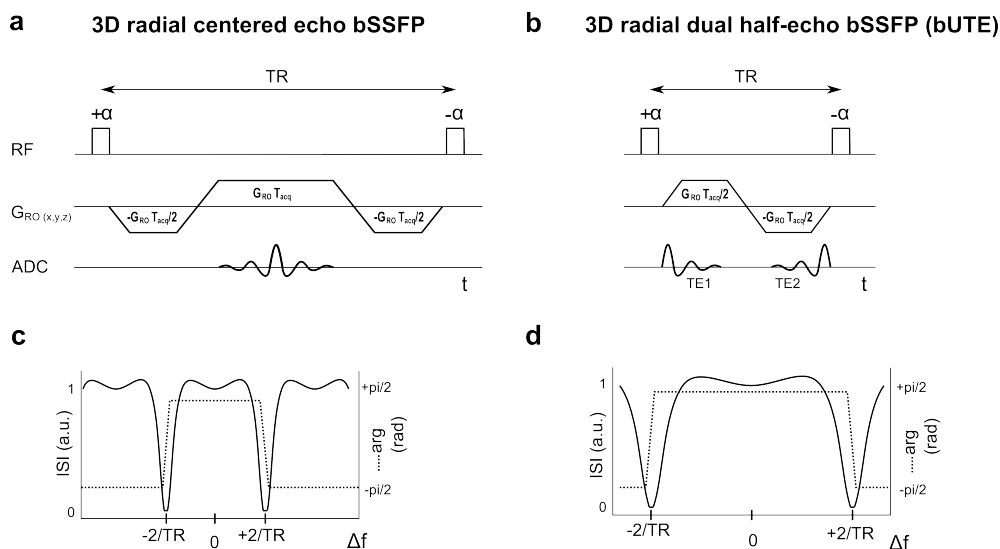


**Figure 5.1:** Sequence schemes of centered echo bSSFP (a) and bUTE (b) and their sensitivities to global off-resonances (c,d). bUTE imaging reduces TR almost to one half which considerably increases the artifact free passband in the frequency range of  $\pm 2/TR$ .

state (section 2.3.2) this implies that pre- and post-phasing gradients with a gradient moment  $|M_G| = G_{RO} \cdot T_{acq}/2$ , with  $G_{RO}$  the readout gradient amplitude and  $T_{acq}$  the sampling duration of the full-echo, have to encompass the image readout. Radial half-echo acquisitions start sampling at the k-space center (section 4.2.2.2), and therefore, do not require any pre-phasing gradients. In the purely hypothetical case of instantaneously switching the readout gradient, half-echoes would therefore be able to reduce TR to one half compared to 3D radial centered echo acquisitions with pre-phasers. The acquisition scheme of centered 3D radial bSSFP (fig. 5.1a) and the proposed technique (fig. 5.1b), both sequences sketched at the same timescale, exemplifies the reduction in TR through two half-echos. Because of similarity to the UTE acquisition scheme, the proposed acquisition was named balanced UTE (bUTE).

Figure 5.1c and 5.1d highlight the benefit in off-resonant signal behavior of the proposed bUTE approach. The bSSFP signal for spins with frequency offsets  $\Delta f$  is presented for full-echo and bUTE sampling, respectively. While both trajectories encode the same field of view at equal imaging bandwidth, the sensitivity to resonance offsets (artifact free imaging in the range  $BW = [-2/TR..+2/TR]$ ) is reduced for the proposed trajectory in fig. 5.1b. Based on the coherent magnetization gained in bSSFP, the same signal amplitude is acquired independently of TR [223]. Therefore, an increased

## 5. CELL TRACKING WITH 3D RADIAL UTE TRAJECTORIES IN COHERENT STEADY STATE

---

SNR per unit time is expected if TR is reduced as proposed with the presented trajectory. Current bSSFP trajectories are limited to an echo generation at TR/2 because of balancing all gradient moments within TR in addition to the requirement of shortest TR. As a result, literature and signal models for acquisitions outside TR are very limited. While  $B_0$  induced  $T_2^*$  weighting at echoes acquired apart from TR center was reported by Scheffler and Henning [132], there are no in vitro and in vivo studies investigating bSSFP contrast outside TR/2. Therefore, and in order to fully benefit from the expected improvements of the technique, the contrast of the two half-echos was investigated and compared to echo centered bSSFP.

### 5.1.3 Methods

#### 5.1.3.1 Pulse sequence and reconstruction

For the 3D bUTE sequence, a 3D radial UTE scheme was adapted as sketched in figure 5.1b. Omitting RF-spoiling and the gradient spoiler at the end of TR produces a coherent steady state (section 2.3.2). By flipping the RF phase by  $180^\circ$  at each TR interval, the magnetization profile for off-resonances as presented in fig. 5.1d is gained. Acquiring a second dataset with constant RF phase allowed for almost banding artifact free images by combining both acquisitions through a weighted combination [227]. Half echoes are acquired during gradient switching with non-equidistant k-space sampling (section 4.2.2.2). Within one TR period, two signals (TE1 at TR start, and TE2 at the end of TR) are sampled. These signals can either be used for two different images, or can be combined by sum-of-squares  $S_{\text{SOS}} = \sqrt{S_{\text{TE1}}^2 + S_{\text{TE2}}^2}$  for improved SNR. The excitation consists of a hard pulse of 0.1 ms duration. Reconstruction was performed with a conventional re-gridding procedure using a Kaiser-Bessel filter and density compensation (see section 4.13).

#### 5.1.3.2 Contrast phantom preparation

In order to investigate soft tissue contrast, a phantom mimicking 6 different tissue types (kidney, liver, spinal cord, skeleton muscle, white matter and gray matter) and blood was established first. Gd-DTPA (Magnevist, Bayer Vital GmbH, Leverkusen, Germany) and a SPIO contrast agent (Resovist, Bayer Vital GmbH, Leverkusen, Germany) were mixed with agarose to get desired  $T_2/T_1$  times within plastic tubes of 10

## 5.1 bSSFP imaging with half-echo acquisition

---

mm in diameter. Table 5.1 summarizes the used contrast agent concentrations and compares the gained  $T_1$  and  $T_2$  values with literature [156].

### 5.1.3.3 Relaxometry

Phantom  $T_1$  was measured employing an Inversion-Recovery-Fast-Spin-Echo (IR-FSE) with 6 different inversion times (50, 100, 200, 400, 800, 1600, 3200 ms) at a temperature of  $23.2^\circ$ , a turbo-factor of 3, TR = 5000 ms, FOV = 90 x 73 mm, matrix = 192 x 156 and a single 5 mm thick slice. Phantom  $T_2$  relaxometry measurements were realized with a 2D Carr-Purcell-Meiboom-Gill (CPMG) sequence with an echo-spacing of 11.1 ms and 24 echos, TR = 5000 ms, FOV = 90 x 73 mm, matrix = 192 x 156 and a single 5 mm slice. A circular polarized wrist-coil of approx. 7 cm in inner diameter was used for all measurements carried out at a 3 Tesla clinical MRI (MAGNETOM Trio, Siemens, Erlangen, Germany). Transverse and longitudinal relaxation times were calculated using a self-written program (IDL, Exelis Inc., CO, USA).  $T_2$  was determined with a linear fit of the logarithmized signal intensity over echo time (for all used TEs the SNR was  $> 5$ ), whereas the first echo was discarded.  $T_1$  was calculated using a 3-parameter fit of the IR-FSE dataset [153].

**Table 5.1:** Radial half-echo bSSFP tissue phantom properties. Relaxation times were measured at 3 T.

	Resovist (mM)	Gd-DTPA (mM)	agar (%)	$T_1$ (ms)		$T_2$ (ms)		$T_2/T_1$ Study
				Study	Lit.[156]	Study	Lit.	
kidney	0.09	0.06	1	987	1194	48	56	0.049
liver	0.17	0.15	0.5	561	812	32	42	0.057
gray m.	0.057	0	0.5	1688	1820	76	99	0.045
spinal	0.01	0.15	2	920	993	69	78	0.075
muscle	0.07	0.03	2	1353	1412	49	50	0.036
white m.	0.025	0.12	2	991	1084	65	69	0.066
blood	0	0.02	0.5	2761	1932	272	275	0.099

## 5. CELL TRACKING WITH 3D RADIAL UTE TRAJECTORIES IN COHERENT STEADY STATE

---

### 5.1.3.4 Phantom measurements

Images were acquired with the new 3D half-echo bSSFP sequence (bUTE) and, for comparison, with a conventional echo-centered 3D radial bSSFP acquisition (c-bSSFP) on the tissue phantom described above. The measurement parameters are summarized in table 5.2. The same imaging setup as used for the relaxometry measurements given above was employed. The individual sample SNR values were calculated for the centered bSSFP, the two echoes TE1 and TE2 gained through bUTE acquisition as well as the combined sum-of-squares image (bUTE average) of TE1 and TE2. To compare tissue image contrast, the sample SNR values were compared to blood and a contrast ratio  $CR = (SNR_{blood} - SNR_{tissue})/SNR_{blood}$  was calculated. In order to quantitatively compare the SNR gain of the new technique with standard radial bSSFP, a scan time ( $T_{aq}$ ) normalized SNR gain value was calculated by multiplying the bUTE SNR gain with  $\sqrt{T_{aq\_bSSFP}/T_{aq\_bUTE}}$ .

**Table 5.2:** Measurement parameters for the bUTE phantom experiment.  $\alpha$  = flip angle;  $N_s$  = number of spokes; m = image matrix; PC = number of phase cycles.

	TR (ms)	TE (ms)	$\alpha$ ( $^\circ$ )	$N_s$	m	FOV (mm)	PC	time (min:sec)
c-bSSFP	6.3	3.1	40	$192^2 \cdot 1.5$	$192^3$	80	2	5:42
bUTE	4.1	0.1/3.8	40	$192^2 \cdot 1.5$	$192^3$	80	2	6:24

### 5.1.3.5 In vivo imaging

To assess the general imaging performance of the bUTE sequence in vivo, images of a wild-type mouse at a resolution of  $(200 \mu\text{m})^3$  were acquired with the centered-echo bSSFP, gradient echo based UTE and the bUTE sampling scheme for comparison. The measurement parameters of those scans labeled as 'lr' are summarized in table 5.3. For those scans, two 18 mm surface coils (Rapid Biomedical, Rimpar, Germany) were used with the animals' knees placed in the center of the coils.

To assess the cell tracking performance, 3D scans of high resolution (voxel size  $(160 \mu\text{m})^3$ ) with standard UTE contrast and bUTE were acquired (measurement parameters of these scans labeled as 'hr' are summarized in table 5.3) and compared to the cell

## 5.1 bSSFP imaging with half-echo acquisition

---

tracking gold standard of 2D GRE. The 2D GRE scan was performed with the following measurement parameters: TR = 18 ms; TE = 7.4 ms;  $\alpha = 15^\circ$ ; matrix =  $320^2$ ; slice thickness = 1.5 mm; slices = 32; FOV = 80 mm; 4 averages; scan time = 9:01 min:sec. The images of the two acquired bUTE echoes were combined by sum-of-squares. A dedicated body coil for mice with an inner diameter of 35 mm (Rapid Biomedical, Rimpar, Germany) was used. The labeling protocol, ectopic subcutaneous injection protocol and animal handling were the same as described in section 4.2.3.1. The subcutaneous injection sites of labeled cells with cellular concentrations of the labeled entities of 7 and 35 cells/ $\mu\text{l}$  were selected to present in vivo cell tracking performance.

For all animal scans, anesthesia during imaging was achieved with Isoflurane (1.4% in 100% Oxygen, flow 1.8 l/min). The animal experiments were approved by the Animal Care and Use Committee at the Veterinary University of Vienna on behalf of the Austrian Ministry of Science and Research according to the Guide for the Care and Use of Laboratory Animals.

**Table 5.3:** Measurement parameters for the bUTE in vivo experiment.  $\alpha$  = flip angle;  $N_s$  = number of spokes; m = image matrix; PC = number of phase cycles.

	TR (ms)	TE (ms)	$\alpha$ ( $^\circ$ )	$N_s$	m (mm)	FOV	PC	time (min:sec)
UTE lr	14.0	0.1	10	$192^2 \cdot 1.28$	$192^3$	38	-	11:01
c-bSSFP lr	8.6	4.2	20	$192^2 \cdot 1.28$	$192^3$	38	2	6:46
bUTE lr	4.4	0.1/4.1	20	$192^2 \cdot 1.28$	$192^3$	38	2	6:58
UTE hr	25.0	0.1	12	$320^2$	$320^3$	50	-	42:40
bUTE hr	5.8	0.1/5.6	20	$320^2$	$320^3$	50	2	19:48

### 5.1.4 Results

#### 5.1.4.1 Phantom measurements

In figure 5.2, images acquired from the tissue phantom are presented. The first (TE1) and second (TE2) echo shown in the first row are merged via sum-of-squares to an averaged image presented in figure 5.2c. The dual-echo half-echo acquisition in the coherent steady state shows similar contrast to blood than the bSSFP acquisition with

## 5. CELL TRACKING WITH 3D RADIAL UTE TRAJECTORIES IN COHERENT STEADY STATE

---

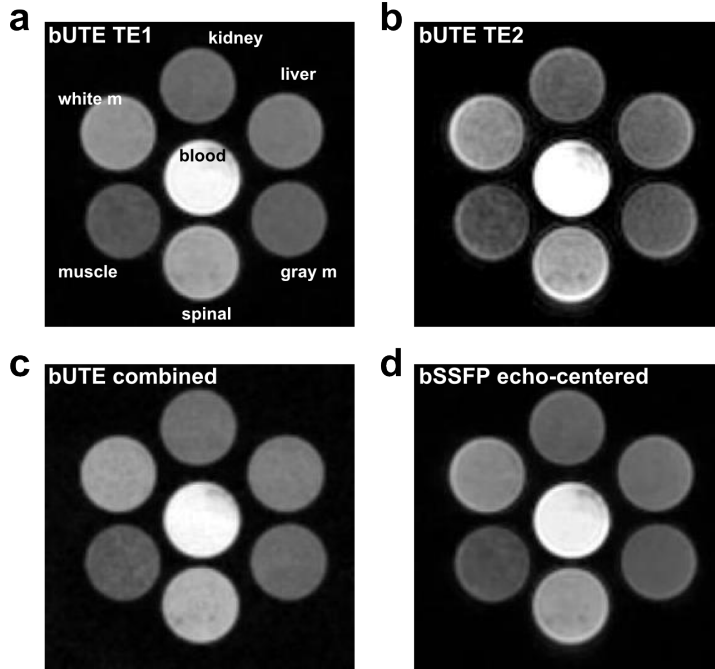


**Figure 5.2:** Phantom measurements comparing bUTE with echo-centered bSSFP tissue contrast. Six different tissues and blood (labeled in (a)) were mimicked through Gd-DTPA and a SPIO solvent mixed to agarose gel in order to reach tissue like  $T_2/T_1$  properties. **a:** bUTE contrast of first echo at  $TE1 = 100 \mu s$ . **b:** bUTE contrast of second echo at  $TE2 = 3.8$  ms. **c:** SOS combination of bUTE first and second echo. **d:** bSSFP contrast with centered echo. The combined bUTE image shows an almost identical tissue image contrast compared to the echo-centered bSSFP acquisition while the reduced TR of bUTE (4.1 ms compared to 6.3 ms of c-bSSFP) promises a considerable reduction in global banding artifacts for in vivo applications.

an centered echo (fig. 5.2d). These acquisitions were further analyzed in terms of tissue SNR presented in table 5.4.

Given these numbers, the contrast between tissue and blood signal was validated by the quantitative analysis presented in figure 5.3. Since blood has the highest signal intensity, a low number in CR means an enhanced relative signal difference, hence in contrast to blood.

While the first echo at  $TE1 = 100 \mu s$  offers a reduced tissue-to-blood contrast, the late echo at  $TE2 = 3.8$  ms yields an enhanced contrast value for all tissues investigated. According to the bSSFP signal equation (eq. 2.36) it is a valid assumption that the tissue signal undergoes a  $T_2$  dependent signal attenuation at later echo positions.

## 5.1 bSSFP imaging with half-echo acquisition

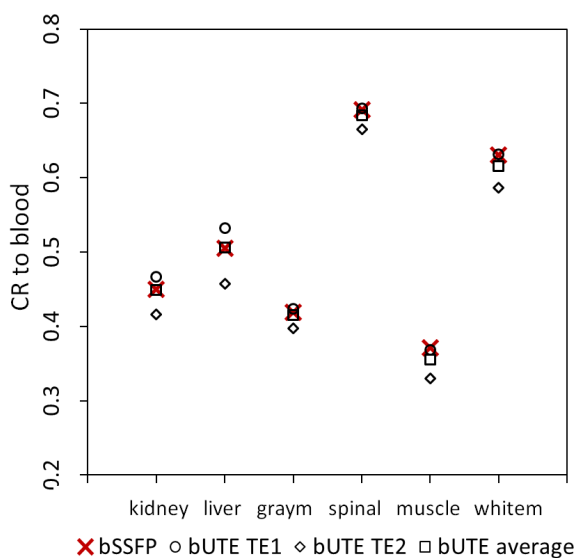


**Figure 5.3:** Contrast ratios  $CR = (SNR_{blood} - SNR_{tissue}) / SNR_{blood}$  of the mimicked six different tissue types to blood. The combination of the two echoes of the bUTE technique gained comparable tissue to blood contrast than the echo-centered bSSFP acquisition (red cross).

**Table 5.4:** SNR measurements comparing bUTE to echo-centered bSSFP (c-bSSFP).

	SNR c-bSSFP (a.u.)	SNR bUTE TE1 (a.u.)	SNR bUTE TE2 (a.u.)	SNR bUTE avg. (a.u.)	SNR gain $T_{aq}$ normalized (%)
kidney	36.48	40.37	28.42	49.83	21.6
liver	40.97	46.02	31.20	56.17	22.1
gray m.	34.00	36.66	27.13	46.02	20.6
spinal	56.08	59.98	45.43	75.83	20.4
muscle	30.09	31.86	22.51	39.41	16.6
white m.	51.11	54.63	40.06	68.31	19.0
blood	81.07	86.47	68.27	110.89	21.8

## 5. CELL TRACKING WITH 3D RADIAL UTE TRAJECTORIES IN COHERENT STEADY STATE

---

Taking into account that blood has a very long  $T_2$  decay, the difference in TE1 and TE2 contrasts is dominated by the tissues'  $T_2$  values. If the two echoes are averaged by sum-of-squares combination, a contrast very similar to the echo-centered bSSFP (labeled with red crosses) is reached, depicted by the match with the black squares in figure 5.3. The SNR numbers presented in table 5.4 were normalized to the actual acquisition time in order to conduct a fair comparison between the bUTE ( $T_{aq} = 5:42$  min) and centered bSSFP ( $T_{aq} = 6:24$  min) acquisitions. As summarized in table 5.4, a remarkable gain in SNR was achieved with the proposed bUTE average approach.

### 5.1.4.2 In vivo imaging

Gradient echo based UTE, centered echo bSSFP and TE1/TE2 merged bUTE images acquired from the hindlegs of a wildtype mouse are compared in figure 5.4. Tissue contrast changes significantly between non-coherent, spoiled (UTE) and the coherent steady state (bUTE). While standard UTE produces almost isointense background signal throughout the covered field of view, the two balanced techniques deliver bright tissue signal from water and lipid congregations. This is exceptionally well demonstrated at the left lower leg of the mouse showing an edema. The balanced UTE image with a significant shorter TR (4.44 vs. 8.62 ms) shows less residual artifacts originating from global off-resonant bands (see fig. 2.5 and fig. 5.1). While both balanced sequences provide an apparently better image SNR within most tissues, the comparison to UTE illustrates that coherent acquisitions will have a reduced applicability for sensing cells in bone marrow. bUTE delivers more intense marrow signal (e.g. well represented in the right femoral marrow) than echo centered bSSFP but most signal, almost equal to muscle, is produced by the UTE sequence.

In vivo images of subcutaneously injected SPIO labeled stem cells are shown in figure 5.5. While the 2D gradient echo has the shortest acquisition time among the compared sequences (2D GRE: 9 min.; 3D bUTE: 20 min.; 3D UTE: 42 min.), the 3D scans deliver a 9-fold finer slice resolution. At a cellular concentration of 7 cells/ $\mu\text{l}$ , the 2D GRE with a 1.5 mm thick slice fails to detect the majority of labeled specimen. At ultra-short TE, sparsely (7 cells/ $\mu\text{l}$ ) distributed cells do not gain enough contrast to background in order to be identified. However, the dark contrast at the injection site for a 5-fold higher cellular dosage (fig. 5.5 bottom) indicates that if individual cells begin

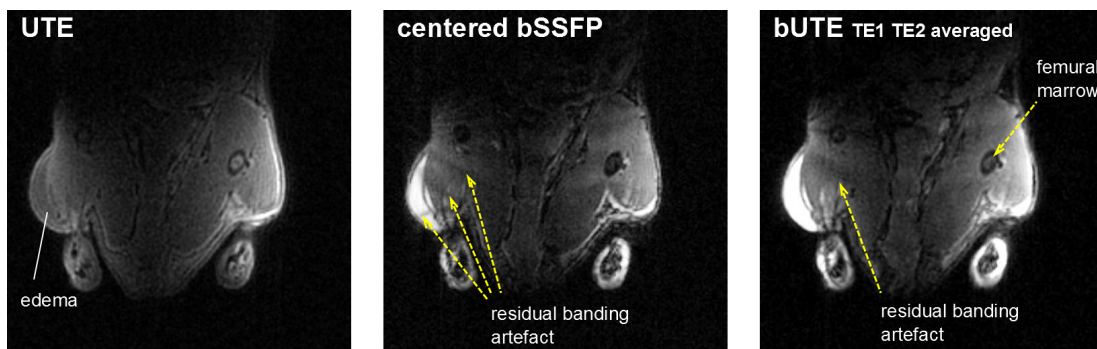


**Figure 5.4:** In vivo comparison of 3D UTE, echo-centered bSSFP and bUTE. The change in tissue image contrast between spoiled UTE and the coherent steady state is best visible at the edema on the left hindleg of the mouse. Compared to the echo-centered bSSFP, the short TR of the bUTE technique considerably reduces banding artefacts associated with global off-resonances.

to build clusters, they become detectable by UTE imaging.

### 5.1.5 Discussion

The bUTE approach seems to be a well-suited candidate for balanced high resolution imaging. The more efficient sampling of the steady state magnetization leads to a SNR gain (about 20 % within this study), and the short TR reduces macroscopic banding artifacts. The reduction in TR of bUTE is even more pronounced at higher resolutions compared to the conventional echo centered implementation.

Analysis of the signal behavior within a phantom of representative tissue relaxation rates shows that bUTE contrast is comparable to standard echo-centered bSSFP. This facilitates an easy in vivo contrast interpretation for radiologists familiar with bSSFP. bUTE acquisitions have a high sensitivity to the microscopic magnetic field perturbations of iron loaded cells, resulting in a negative cellular contrast representation. This is not surprising since the phase reversals of bands in the microscopic environment of the cells, responsible for most of the voxel signal degradation in bSSFP [110], are independent of the echo position within TR.

For tissues with a high  $T_2/T_1$  ratio, it is obvious that bUTE is much better suited for cell tracking because of the amplified background SNR. However, if  $T_2/T_1$  declines (as for example in bone marrow), the bright background of UTE may facilitate a better

## 5. CELL TRACKING WITH 3D RADIAL UTE TRAJECTORIES IN COHERENT STEADY STATE

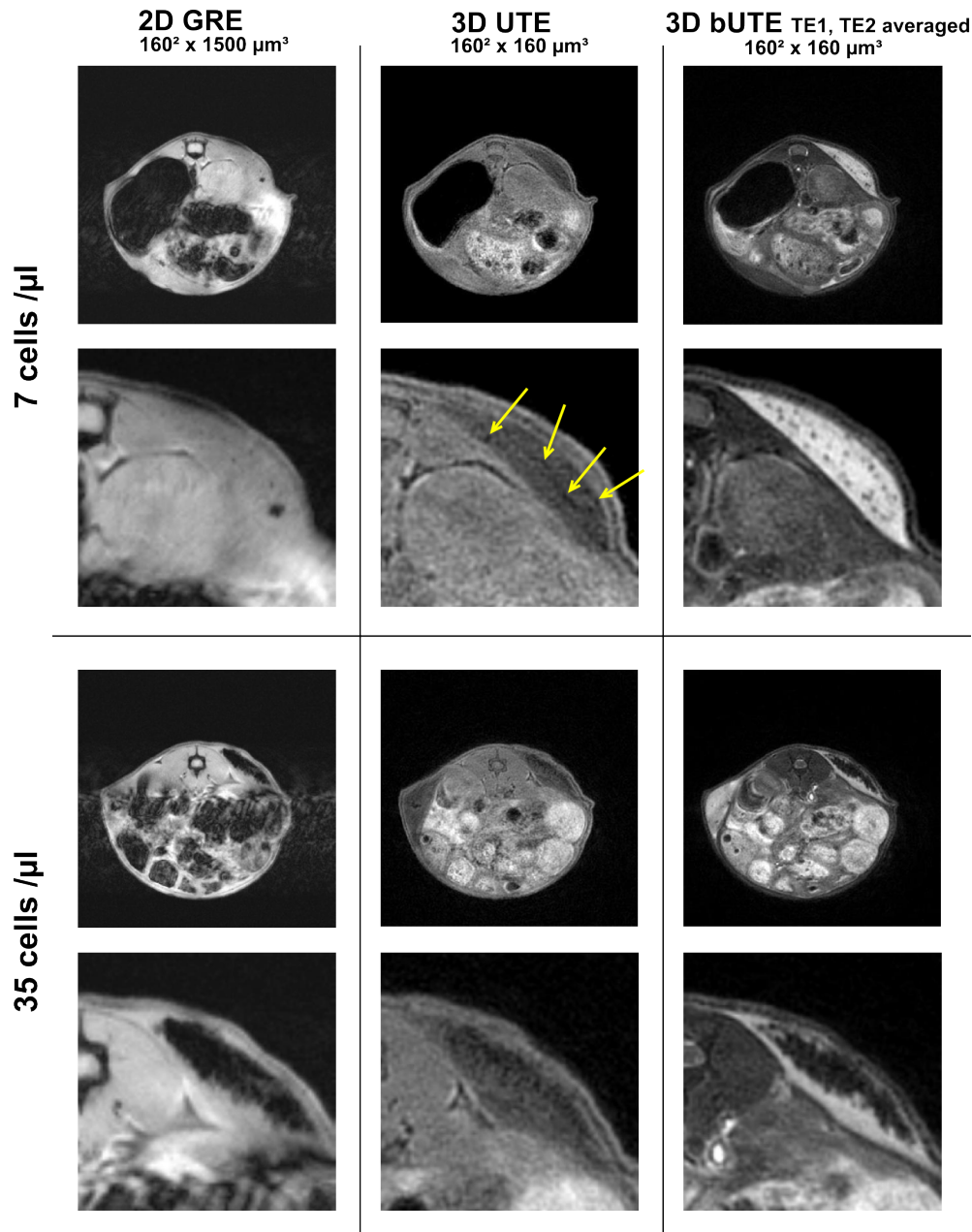


**Figure 5.5:** In vivo comparison of 2D GRE, 3D UTE and 3D bUTE. Subcutaneous injection sites of SPIO labeled progenitor cells at concentrations of 7 cells/μl (top two rows) and 35 cells/μl (bottom two rows) are presented. Magnified views on the cell depots are given in the 2<sup>nd</sup> and 4<sup>th</sup> row. Even though a very high in-plane resolution of 160 μm is achieved by the 2D GRE sequence, the large slice thickness hinders cellular depiction if the cells get more sparsely distributed (e.g. at the injection site of 7 cells/μl). The UTE sequence with a more than 4-fold prolonged acquisition time (43 min. compared to 9 min. for 2D GRE) shows sparsely distributed signal voids (yellow arrows) - originating from the SPIO-loaded cells. The 3D bUTE images presented on the right give best cellular contrast compared to the presented acquisition techniques for both, low and high cellular concentrations, at an acceptable scanning time of 20 minutes.

## 5.1 bSSFP imaging with half-echo acquisition

---

cellular distinction.

In summary, for the cell tracking model presented, the balanced UTE sequence gives best cell tracking performance. The bUTE images deliver a very detailed visualization for single cell depositions at 7 cells/ $\mu\text{l}$  as well as at higher cellular concentrations of 35 cells/ $\mu\text{l}$ .

## 5. CELL TRACKING WITH 3D RADIAL UTE TRAJECTORIES IN COHERENT STEADY STATE

---

### 5.2 Single cell detection using off-resonant reconstructions of 3D center-out bSSFP <sup>1</sup>

#### 5.2.1 Introduction

In the presented study, an acquisition and reconstruction technique is introduced that allows the detection of labeled cells at their initial voxel position with positive contrast. It is based on a bSSFP acquisition and the interaction of the imaging point-spread function (PSF) of center-out 3D radial acquisitions to off-resonant spins as previously reported [228]. Key of the technique is that displaced magnetization can be, in part, spatially refocused by an off-resonant frequency introduced before reconstruction. This results in signal amplification at the initial position of an iron oxide loaded cell. The refocusing of off-resonant spins has recently been published as co-RASOR approach [170, 229] for the spatially accurate visualization of macroscopic paramagnetic objects like brachytherapy seeds and biopsy needles. In the presented work, this principle was applied and investigated for much smaller structures at the mesoscopic scale, such as SPIO labeled cells. To maximize SNR for high resolution single cell detection, the co-RASOR principle was fused with a bSSFP acquisition for signal generation.

Major aims of the study were:

- To investigate the underlying mechanisms by numerical simulations of intra-voxel inhomogeneities produced by paramagnetically labeled cells.
- To determine the sensitivity of the technique to the iron load of cells.
- To investigate the impact of the acquisition parameters of imaging bandwidth and voxel size on the resulting contrast.
- To validate the detection sensitivity with measurements of sparsely distributed cells in agarose-phantoms.
- To give a proof of principle in vivo.

#### 5.2.2 Theory

Considering a single spherically shaped cell with a paramagnetic load producing a magnetic susceptibility shift relative to the surrounding media, the produced magnetic

---

<sup>1</sup>This chapter is based on the publication *Positive contrast of SPIO-labeled cells by off-resonant reconstruction of 3D radial half-echo bSSFP*, *NMR in Biomedicine (2014)* [22]

## 5.2 Single cell detection using off-resonant reconstructions of 3D center-out bSSFP

---

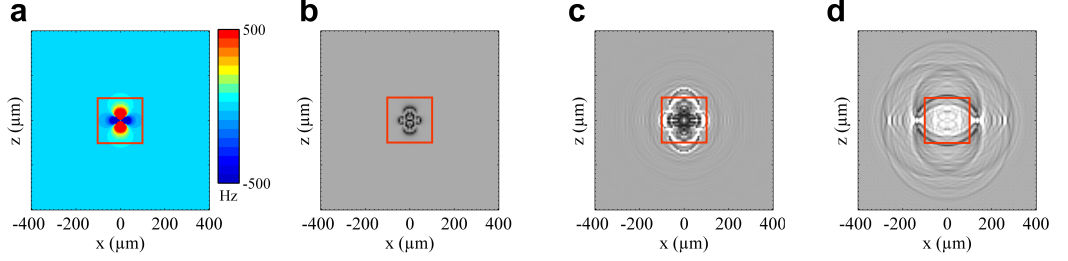


**Figure 5.6:** **a:** Field offset  $\Delta f$  surrounding a cell loaded with 10 pg Fe. The red box marks an isotropic 200  $\mu\text{m}$  voxel. **b:** Steady state signal response (magnitude) to the off-resonances introduced by the magnetic perturber. **c:** The bSSFP magnetization of (b) undergoes a spatial shifting due to the radial readout trajectory and the underlying frequency offset (exemplified for a readout bandwidth of 200 Hz/pixel). As a result, a magnitude aggregation in a certain distance to the cell is produced. **d:** Adding a global  $B_0$ -offset (e.q.  $\Delta B_{0\text{add}} = 100$  Hz) to the bSSFP data prior to the 3D radial reconstruction, the hyperintense areas visible in (c) are shifted to the center of the voxel resulting in a voxel with positive contrast to the background.

field disturbance and, hence, frequency offset outside the cell can be written as [35]

$$\Delta f_{r\theta} = \frac{\gamma}{4\pi} \frac{K_{Fe} m_c}{r^3} (3 \cos^2 \theta - 1) \quad (5.1)$$

where  $\gamma$  is the gyromagnetic ratio (MHz/T),  $K_{Fe} = 1.34 \cdot 10^{-19} T / (\text{pg}/\text{m}^3)$  a calibration coefficient between iron load and effective magnetization [35],  $m_c$  the mass of iron load of a single labeled cell in pg,  $\theta$  the polar angle relative to the direction of the main magnetic field  $B_0$ , and  $r$  the radius from the center of the cell (m). According to this formula, the majority of spins close to a magnetic perturber have a distinct frequency offset with respect to the main magnetic field. They experience an image displacement into the direction of the readout gradient [131]:

$$\Delta \mathbf{x}_{RO} = \frac{\Delta f \cdot N}{BW} \mathbf{e}_{RO}. \quad (5.2)$$

In the above expression,  $\Delta \mathbf{x}_{RO}$  is the image displacement in pixels of transversal magnetization with resonant offset  $\Delta f$  (Hz),  $N$  the imaging resolution,  $BW$  the total imaging bandwidth (Hz), and  $\mathbf{e}_{RO}$  the unity vector heading towards the direction of the readout gradient. For standard Cartesian sampling, the readout direction  $\mathbf{e}_{RO}$  does not change

## 5. CELL TRACKING WITH 3D RADIAL UTE TRAJECTORIES IN COHERENT STEADY STATE

---

with the acquired k-space line and therefore, broadening of the final image contrast into the readout direction is observed. For 3D radial trajectories, as employed within this study, the displacement can be described by a point-spread function for off-resonant spins which accounts for the different readout directions used for spherical k-space sampling. If  $M_{(r)}$  is the transversal magnetization of an imaging experiment at a radial distance  $\mathbf{r}$  from a field perturbing object and  $\Delta f_{(r)}$  the local frequency offset at that point, the acquired shifted magnetization  $M_{\Delta f}$  is calculated as

$$M_{\Delta f} = M_{(r)} \star PSF_{\Delta f_{(r)}} \quad (5.3)$$

where  $PSF_{\Delta f_{(r)}}$  is the off-resonant point-spread function depending on the sampling strategy and local field-offset  $\Delta f_{(r)}$  in Hz, and  $\star$  is the convolution. If a 3D radial center-out trajectory is employed,  $PSF_{\Delta f_{(r)}}$  is a spherical shell with radius  $r_{PSF} = \Delta f_{(r)}/BW/N$  in pixel units.

Figure 5.6 depicts the displacement of cellular contrast acquired with a 3D radial half-echo sampling trajectory. The field disturbance produced by a 10 pg Fe loaded cell is presented in figure 5.6a. Figure 5.6b shows the influence of the frequency offset on the transversal steady state magnetization following a fully balanced SSFP experiment. For a 3D radial half-echo acquisition, the acquired magnetization in figure 5.6c is the result of the convolution of the steady state magnetization (fig. 5.6b) with the off-resonant PSFs for the corresponding field-offsets. The radius of the PSFs depends on the local frequency offset, and as a result, the apparent displacement of the magnetization increases with decreasing radius to the cell. This finally leads to a signal loss at the center surrounded by a signal accumulation at a distinct distance to the perturber (hyperintense contour in figure 5.6c).

To gain localized positive contrast at the position of the cell, this almost spherical hyperintensity has to be shifted back to the central point. For a perfectly spherical signal displacement, the signal recovery at the center can be realized with a single de-convolution of a spherically shaped kernel. If a 3D radial half-echo trajectory is employed such a global convolution is equivalent to the acquisition of the magnetization under a global field-offset  $\Delta B0_{add}$ . As discussed by Seevinck et al. [170], this global field-offset can be introduced as a reconstruction step prior to the non-uniform FFT.

## 5.2 Single cell detection using off-resonant reconstructions of 3D center-out bSSFP

---

This is done by modulating the acquired raw data lines with a frequency offset  $\Delta B0_{add}$  (in Hz)

$$s'_k = s_k \cdot e^{j2\pi\Delta B0_{add}\tau_k} \quad (5.4)$$

where  $s_k$  is the sampled raw data at k-space position  $k$  and  $\tau_k$  the time elapsed from sampling k-space center to the k-space position  $k$ .

Applying an additional frequency offset  $\Delta B0_{add} = 100$  Hz yields the localized cellular positive contrast shown in figure 5.6d with a hyperintense signal for the central, cell containing voxel.

### 5.2.3 Methods

**Simulations** The bSSFP signal response  $M_{(r)}$  was simulated within a discretized imaging volume as described by Lebel et al. [110]. A 201 x 201 x 201 grid was employed covering a volume of interest of 1600 x 1600 x 1600  $\mu\text{m}^3$ . Except for the off-centered simulations in figure 5.15, a spherical perturber of radius 7  $\mu\text{m}$  was placed on the central grid position and its field map corresponding to equation 5.1 was calculated. Outside the cell, the transversal magnetization vector for each grid position was evaluated with Eq. 2, 3, 4 and 5 in [132]. For the experiments with additional  $\Delta B0_{add}$ , the local field-offset was changed according to  $\Delta f'_r = \Delta f_r + \Delta B0_{add}$ . The point-spread functions for off-resonant spins  $PSF_{\Delta f}$  were defined as spherical shells with radii of  $r_{PSF} = \Delta f / BW / N$ . In order to match the PSFs shell position to the discrete simulation grid with a spatial resolution of  $\Delta n = 8 \mu\text{m}$ , the exact local field-offsets  $\Delta f'_{(r)}$  were discretized to  $BW / N \cdot \Delta n / \Delta x$  increments with  $\Delta x$  as the voxel size. For all sub-voxels with the same field-offsets  $\Delta f$ , the 3D-convolution with  $PSF_{\delta f}$  was performed while sub-voxels with  $\Delta f'_{(r)} \neq \Delta f$  were set to zero. This was repeated for all present field-offsets and the convolution results were subsequently added to get the total off-resonant signal response. The final voxel contrast was calculated by convolving all sub-voxels with the idealized image-space point-spread function which is the 3D Fourier transform of the acquired k-space sphere [230]. Isotropic image resolutions of 200/300/400  $\mu\text{m}$  were investigated containing  $25^3/37^3/50^3$  sub-voxels. The repetition times of TR = 5, 7.5 and 10 ms and imaging bandwidths of  $BW / N = 100, 200$  and 300 Hz/pixel were

## 5. CELL TRACKING WITH 3D RADIAL UTE TRAJECTORIES IN COHERENT STEADY STATE

---

chosen in order to address the technical limitations assuming a clinical gradient system at resolutions mentioned above. Background  $T_1/T_2$  was set to a representative value for different parenchymas of 1200/80 ms [155, 156]. Excitation flip-angles were kept at the SNR optimum for the background signal [131]. Unless otherwise specified, a voxel size of 200  $\mu$ m, TR = 7.5 ms and a bandwidth of 200 Hz/pixel were used for all simulations.

**Half echo 3D bSSFP sequence and reconstruction** The bUTE sequence scheme as discussed in section 5.1 and sketched in figure 5.1b was used for data acquisition. Prior to reconstruction, each raw data line was modulated with the desired off-resonant frequency  $\Delta B0_{add}$  as given in equation 5.4. Since the aim was to find  $\Delta B0_{add}$  which produces the best signal recovery, the reconstruction of the 3D radial datasets was performed for a range of field-offsets. The spectral range was adjusted according to the iron load of the cells under investigation and the imaging bandwidth. A fast parallel 3D regridding algorithm [231] using a Kaiser-Bessel kernel [232, 233] was implemented employing the parallel computing capabilities of a graphics processing unit (GPU) using Compute Unified Device Architecture (CUDA). The used implementation was inspired by a threaded multicore CPU implementation [234]: The 3D k-space grid was divided into smaller subunits, and calculations were performed in parallel both within and over these subunits. Special care was taken to reduce memory latencies by using the GPUs shared memory as a cache within those subunits. The final implementation allowed for a reconstruction of a 256 x 256 x 256 matrix out of  $256^2$  radial spokes within 1.4 s on a GeForce GTX 670 with 4 GB of total memory (NVIDIA Corporation, CA, USA). For positive contrast with background suppression, a pixelwise search for the magnitude maxima and minima within the spectral range of off-resonant reconstructions followed by a subtraction of both was performed. In order to boost cellular CNR, the off-resonant subtraction images gained through TE1 and TE2 were consecutively combined via sum-of-squares.

**Cell labeling and phantom preparation** Cell labeling was performed, and the model of ectopic vessel formation was used as described in section 4.2.3.1. Images were acquired 14 days after injection.

For the in vitro phantom, a second patch of ECFCs was labeled with the same protocol

## 5.2 Single cell detection using off-resonant reconstructions of 3D center-out bSSFP

---

as in section 4.2.3.1 but with an SPIO concentration of 400  $\mu\text{g}/\text{ml}$  Fe. The quantification with the susceptometric method described in section 2.2.3.4 resulted in an average iron content per cell of 79 pg.

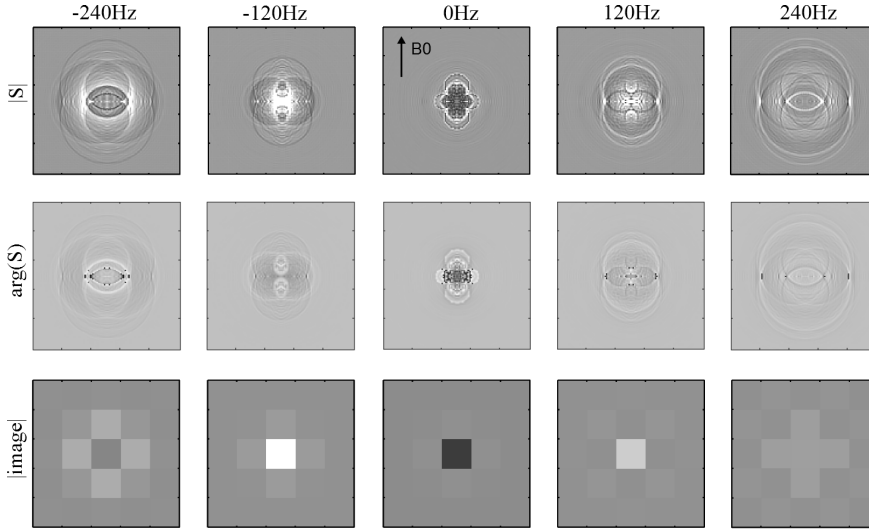
The single-cell phantom was prepared by filling a 50 ml polycarbonate tube with 1 % agarose gel containing 5 mm NMR tubes which were removed after the gel had solidified in order to provide small cavities for subsequent placing of the labeled cells. To gain a background signal comparable with numerical simulations, 0.15 mM Gd-DTPA and 0.05 mM Resovist were added to the gel to reach relaxation times of  $T_1/T_2 = 1074/65.9$  ms. The centrifuged SPIO-labeled cells were resuspended in 0.5 % agarose gel to reach densities of 2.5, 5, 10, and 20 cells/ $\mu\text{l}$  and filled into the cavities within the agarose-filled 50 ml tube. Unlabeled ECFCs (20 cells/ $\mu\text{l}$ ) were filled into the central cavity.

**MR imaging** The sequence was implemented on a 3T clinical MRI (MAGNETOM Skyra, Siemens Healthcare, Erlangen, Germany) with a gradient strength of  $G_{max} = 43$  mT/m at a slew rate of 180 mT/(m·ms). A circular polarized whole body volume coil for mice with an inner diameter of 3.5 cm and an overall length of 6 cm (RAPID Biomedical GmbH, Rimpar, Germany) was used for all experiments. The phantom tube was positioned along the main magnetic field and scanned with the 3D radial dual half-echo sequence and a non-selective 100  $\mu\text{s}$  hard pulse with varying resolutions of 200, 300 or 400  $\mu\text{m}$  and the scan parameters: TR = 7.5/5.7/5.1 ms,  $\alpha = 29^\circ$ , TE1 = 0.1 ms, TE2 = 7.3/5.5/4.9 ms at a matrix size of 256<sup>3</sup>/160<sup>3</sup>/128<sup>3</sup>, an imaging bandwidth of 199/313/391 Hz/pixel and 256<sup>2</sup>/160<sup>2</sup>/128<sup>2</sup> spokes. For in vitro CNR measurements, an automated detection of voxels containing labeled cells was performed. The voxels were selected within the on-resonant bSSFP image if their signal intensities dropped below an upper threshold. A threshold of 0.8-fold the mean background signal was chosen which corresponds to a minimum CNR value  $> 5$  within all imaging resolutions. A Tukey boxplot was used to depict the different acquisition and reconstruction CNRs. The in vitro sample of 20 cells/ $\mu\text{l}$  was selected for CNR validation and 16/11/8 slices were evaluated at the 200/300/400  $\mu\text{m}$  scans. About 8 voxels/ $\mu\text{l}$  fell below the detection threshold at the 200  $\mu\text{m}$  scan. This density is 2.5-fold lower than the cellular count of 20 cells/ $\mu\text{l}$  from cell culture. Therefore some clustering of cells and an exclusion of labeled entities by the threshold were assumed. To investigate the dependency of the ORRS

## 5. CELL TRACKING WITH 3D RADIAL UTE TRAJECTORIES IN COHERENT STEADY STATE

---

**Figure 5.7:** Results of intra-voxel simulations with a single 25 pg Fe perturber placed at the central position acquired with an imaging bandwidth of 200 Hz/pixel and applied field-offsets  $\Delta B_{0_{add}} = -240/-120/0/120/240$  Hz. The magnitude and phase of the intra-voxel signal are presented in the top and middle row. The final image contrast of a 200  $\mu\text{m}$  voxel volume is presented in the bottom row. For  $\Delta B_{0_{add}} = 0$  Hz, the standard (negative) bSSFP contrast is shown. Signal recovery with hyperintense contrast is obtained at the reconstruction of -120 Hz, and a second, less intense maximum is observed at 120 Hz.



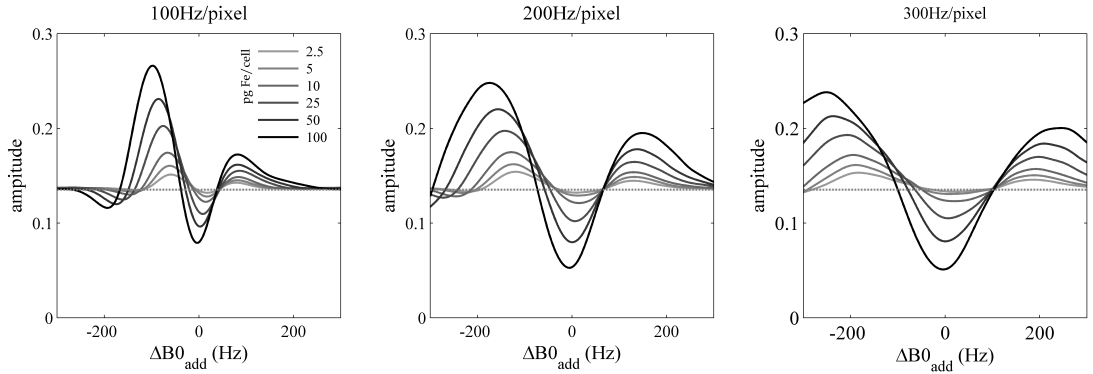
on intra-voxel cellular position, half-voxel shifted images of the in vitro dataset were calculated by a linear phase modulation of k-space as described by Scheffler [235]. In vivo images were acquired with a total acquisition time of 19 min 48 sec acquiring  $320^2$  spokes with two consecutive phase cycles ( $\alpha/-\alpha$ ;  $\alpha/\alpha$ ), without respiratory triggering (TR = 5.8 ms,  $\alpha = 20^\circ$ , TE1 = 0.1 ms, TE2 = 5.6 ms, BW = 256 Hz/pixel) resulting in a  $320^3$  matrix with an isotropic resolution of 160  $\mu\text{m}$ . The combination of the two phase-cycled bSSFP acquisitions was performed after modulation and reconstruction with  $\Delta B_{0_{add}}$  by a weighted combination as described by Çukur et al. [227].

### 5.2.4 Results

**Simulations** The simulations in figure 5.7 show the sub-voxel signal distribution for the first half-echo (TE1) of a single 25 pg Fe perturber placed in the middle of the grid calculated for 5 representative global field-offsets. The presented slice is aligned in parallel to the main magnetic field  $B_0$ . The top and middle row show the magnitude

## 5.2 Single cell detection using off-resonant reconstructions of 3D center-out bSSFP

**Figure 5.8:** Simulations presenting the off-resonant reconstruction contrast (off-resonant reconstruction spectrum). The signal evolution of the central 200  $\mu\text{m}$  voxel containing a single cell (2.5..100 pg Fe/cell) for three representative readout bandwidths (100, 200 and 300 Hz/pixel) is presented. The dashed gray line marks the image signal without any perturber. At  $\Delta B_{0\text{add}} = 0$  Hz, the standard bSSFP signal for 3D radial half-echo sampling is produced. The signal maximum at  $\Delta B_{0\text{add}}(\max(|S|))$  produces a positive contrast against the background higher than the on-resonant negative contrast. The magnitude at and the off-resonant position of  $\Delta B_{0\text{add}}(\max(|S|))$  show a strong dependence on readout bandwidth and iron concentration.



and phase following the sub-voxel wise convolution with the off-resonant PSFs, and the bottom row presents the resulting image with an isotropic voxel size of 200  $\mu\text{m}$ . The contrast modulation of the central, cell containing voxel, referred to as off-resonant reconstruction spectrum (ORRS) herein, is presented in more detail in figure 5.8. The spectral position of maximum signal recovery  $\Delta B_{0\text{add}}(\max(|S|))$  and the gained amplitude scale with paramagnetic load and imaging bandwidth. There is a direct relation between the radius of the signal aggregation visible in the on-resonant intra-voxel simulation (fig. 5.7) and the maximum of signal recovery for 25 pg Fe in the central graph in figure 5.8 ( $\Delta B_{0\text{add}}(\max(|S|)) \approx -150$  Hz;  $r = -\Delta B_{0\text{add}}/\text{BW}/N \approx 0.75$  pixel). The asymmetry of the ORRS due to a major fraction of magnetization with a positive frequency offset is a result of the dipolar field stated in equation 5.1. The fractional signal change of the subtraction between reconstructions with  $\Delta B_{0\text{add}}(\max(|S|))$  and  $\Delta B_{0\text{add}}(\min(|S|))$  for different resolutions and iron loads per cell is presented in figure 5.9. The sensitivity of the proposed subtraction method for an isotropic 300  $\mu\text{m}$  acquisition still exceeds the standard 200  $\mu\text{m}$  bSSFP experiment (black dashed line). Figure 5.10 compares the signal modulation as a function

## 5. CELL TRACKING WITH 3D RADIAL UTE TRAJECTORIES IN COHERENT STEADY STATE

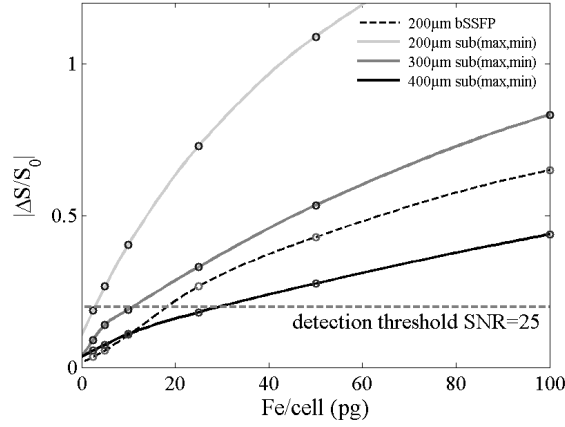


**Figure 5.9:** Simulations of the fractional signal change vs. cellular iron load. The dashed line represents standard dark bSSFP contrast at  $\Delta B_{0add} = 0$  Hz. With a combination of  $\Delta B_{0add}(\max(|S|))$  and the negative contrast at  $\Delta B_{0add} = 0$  Hz in a subtraction image, far bigger voxel dimensions can be chosen for single cell tracking at the same iron content. For a visual guidance, the detection limit with  $CNR = 5$  for an assumed image SNR of 25 is drawn as a gray dashed line.

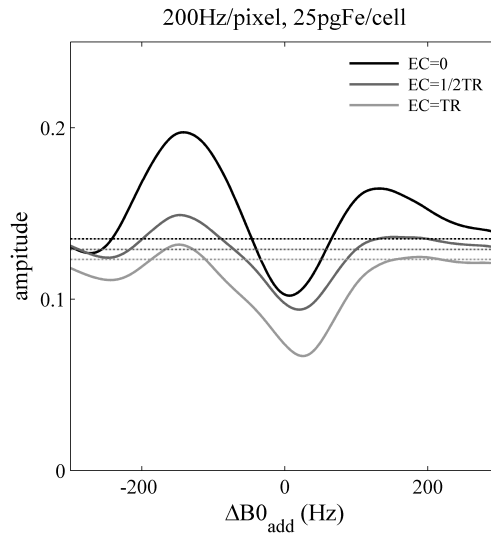
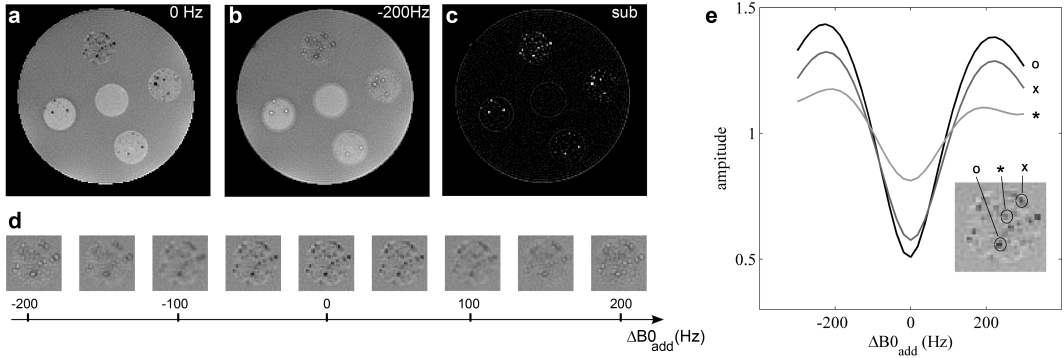


**Figure 5.10:** Off-resonant reconstruction spectrum for different echo (EC) positions within TR. The dashed line marks the background signal  $S_0$  without any perturber. All curves show similar contrast behavior, but largest signal difference ( $(\max(|S|) - \min(|S|)) / S_0$ ) is achieved directly after excitation. Since the position of signal maxima and minima slightly differ between echo positions, the subtraction contrast  $\max(|S|) - \min(|S|)$  is calculated before merging the two echoes (EC = 0 and EC = TR) via SOS.

## 5.2 Single cell detection using off-resonant reconstructions of 3D center-out bSSFP

**Figure 5.11:** Agarose cell phantom with 2.5/5/10/20 cells/ $\mu\text{l}$  (from top-left counter clockwise). The cells contain an average iron content of 79 pg Fe. The control in the center consists of unlabeled ECFCs in a density of 20 cells/ $\mu\text{l}$ . **a:** Standard bSSFP contrast, **b:** reconstructed image at  $\Delta B_{0_{add}} = -200$  Hz and **c:** voxel-wise subtraction of  $\max(|S|)$  and  $\min(|S|)$ . **d:** Reconstructions with varying field offsets  $\Delta B_{0_{add}} = -200..200$  Hz show the signal evolution over  $\Delta B_{0_{add}}$  (presented for the sample with 20 cells/ $\mu\text{l}$ ). **e:** ORRS (+/- 300 Hz, resolution: 15 Hz) for three different voxels (marked with \*,x,o) bearing labeled cells present their characteristic off-resonant signal evolution.



of  $\Delta B_{0_{add}}$  between different echo positions: directly after excitation, at  $\text{TR}/2$  and at  $\text{TR}$ . Echo acquisition directly after excitation yields maximum relative signal difference ( $\Delta S/S_0 = 0.70$ ;  $\Delta S = \max(|S|) - \min(|S|)$ ) followed by the late echo ( $\Delta S/S_0 = 0.52$ ) and at the centered echo ( $\Delta S/S_0 = 0.42$ ).

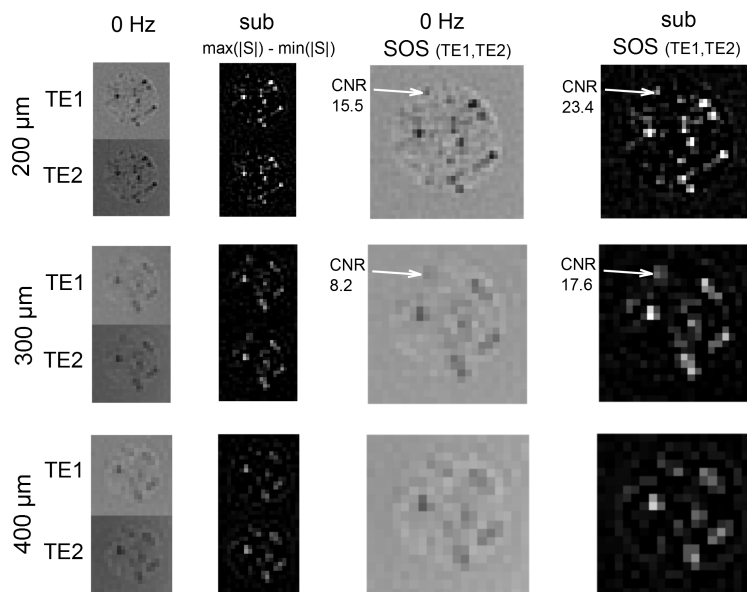
**In vitro study** The phantom used consists of cells at different cellular densities embedded in agarose gel. Figure 5.11 shows reconstructed images from the acquisition  $\text{TE}_1$  at an isotropic resolution of  $200 \mu\text{m}$ . The initially dark voxels (standard bSSFP contrast) (fig. 5.11a) experience a signal recovery due to the off-resonant reconstruction resulting in a hyperintense voxel signal (fig. 5.11b). Selected voxels show a spectral course matching the numerical simulations, and negative frequency offsets yield a minimally higher signal gain (fig. 5.11e). An automated pixel-wise search for the signal maximum and minimum used for the subtraction image allows for optimal positive contrast independently of the total iron load and intra-voxel positioning within a voxel (fig. 5.11c).

Figure 5.12 compares the cellular contrast of bSSFP (0 Hz) with the proposed off-resonant subtraction (sub) method using a SOS combination of  $\text{TE}_1$  and  $\text{TE}_2$ . Three

## 5. CELL TRACKING WITH 3D RADIAL UTE TRAJECTORIES IN COHERENT STEADY STATE

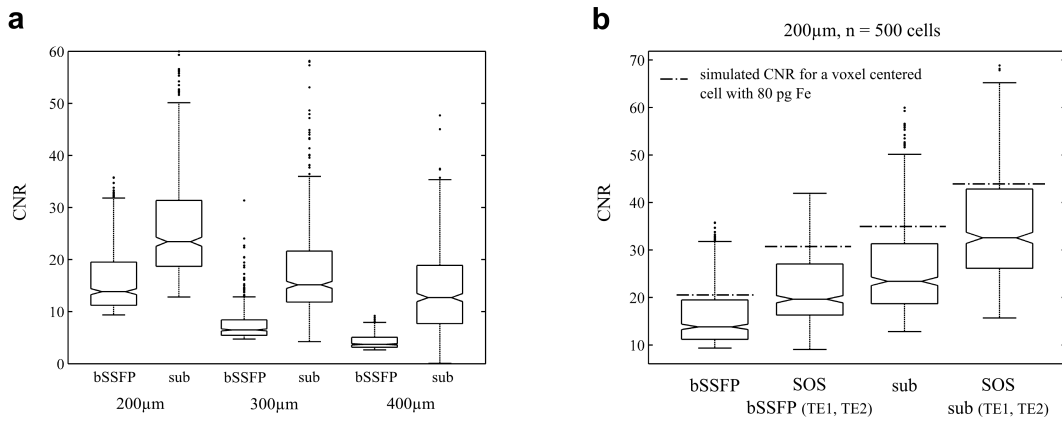
---

**Figure 5.12:** Images acquired with different resolutions and adapted imaging parameters (TR, BW). A speed-up of 6-fold was gained comparing 200  $\mu\text{m}$  with 400  $\mu\text{m}$ . The two columns on the right show the SOS combination of the early (TE1) and late echo (TE2). CNR enhancement between the on-resonant (0 Hz) standard bSSFP contrast and the off-resonant subtraction approach (sub) is clearly visible in voxels with a low iron content (white arrows).



## 5.2 Single cell detection using off-resonant reconstructions of 3D center-out bSSFP

**Figure 5.13:** Boxplots comparing the in vitro on-resonant bSSFP CNR with the new off-resonant reconstruction technique (sub) calculated from selected cell containing voxels. The box defines the first and third quartile, whiskers correspond to 1.5-fold the interquartile range and outliers are labeled by dots. **a:** For the three resolutions investigated (200/300/400  $\mu\text{m}$ ), the off-resonant reconstruction technique achieves a considerably better cellular CNR performance than the on-resonant bSSFP reconstruction. **b:** With a SOS combination of TE1 and TE2, CNR is further increased.



acquisitions with isotropic resolutions of 200/300/400  $\mu\text{m}$  are presented. The aim was to reach the shortest possible scanning time by adapting the sequence parameters of imaging bandwidth, TR, matrix size and acquired number of radial spokes. The acquisition time was significantly reduced from 8 min/15 sec to 1 min/27 s between 200  $\mu\text{m}$  and 400  $\mu\text{m}$  image resolution while image SNR for TE1 of the three measurements was 36.8, 37.7 and 31.2. The voxel highlighted in figure ?? indicates that similar cellular CNR performance is gained using the off-resonant subtraction approach with the fast 300  $\mu\text{m}$  (CNR = 17.6) scan compared to the standard bSSFP contrast at 200  $\mu\text{m}$  (CNR = 15.5).

Figure 5.13 shows the CNR of selected cell containing voxels (as described in the Experimental section) as boxplots. The off-resonant subtraction method shows a substantial increase in CNR compared to signal-void on-resonant bSSFP throughout the measured resolutions (fig. 5.13a), which is further improved by SOS combination (fig. 5.13b) of the two acquired echoes. The simulated CNR (80 pg Fe, dash-and-dot line in fig. 5.13b) is slightly above the median of the measured values for all methods.

## 5. CELL TRACKING WITH 3D RADIAL UTE TRAJECTORIES IN COHERENT STEADY STATE

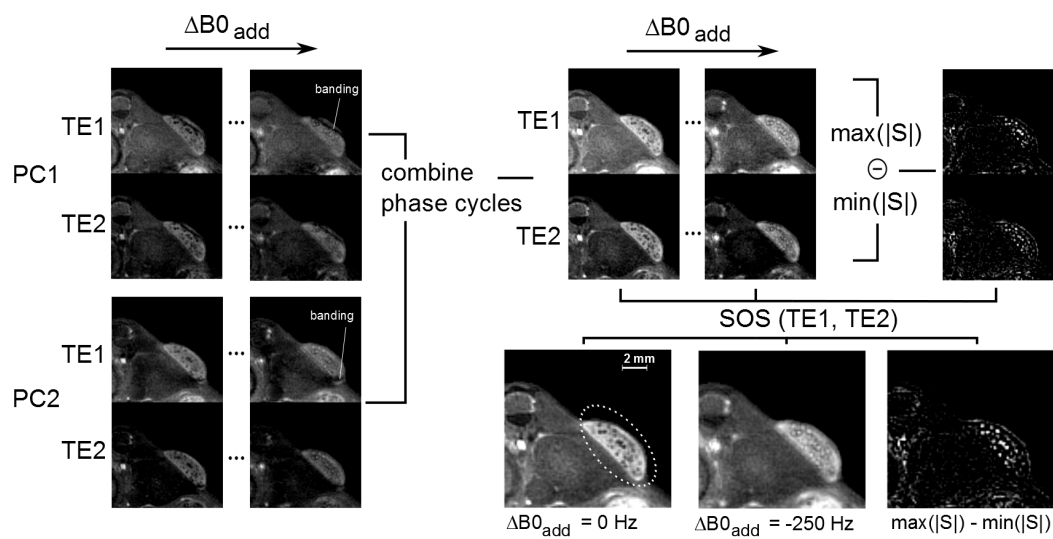


**Figure 5.14:** Axial view of the subcutaneous injection site (marked with dashed line) obtained with the 3D radial half-echo sequence and two phase cycles ( $PC1 = \alpha/-\alpha$ ,  $PC2 = \alpha/\alpha$ ). Reconstruction is performed as follows: First, the off-resonant reconstruction images are calculated. Second, the two phase cycles are combined. Third, the subtraction images are generated by a pixel wise search for the signal minimum and maximum within the off-resonant reconstruction spectrum. As a last step, the two half-echo images TE1 and TE2 are combined via sum-of-squares.

## 5.2 Single cell detection using off-resonant reconstructions of 3D center-out bSSFP

---

**In vivo study** Figure 5.14 shows an axial slice of 160  $\mu\text{m}$  in thickness of the subcutaneous injection site imaged 14 days after injection. The amount of bright spots visible is in fairly good agreement with the expected number of 17 cell containing voxels (injection volume throughout the slice = 2.5  $\mu\text{l}$ , and assuming a homogeneous distribution of cells within the islet of 6.7 cells/ $\mu\text{l}$ ). Intermediate steps of the image processing chain are presented. The 3D radial acquisition turns out to be motion insensitive and produces artifact free images in which the cell bearing voxels are clearly visible. For comparison, the images of an on-resonant reconstruction ( $\Delta B_{0\text{add}} = 0$  Hz), an off-resonant reconstruction ( $\Delta B_{0\text{add}} = -250$  Hz) and of the min/max subtraction are presented. Through phase cycling [236], magnitude bands within the subcutaneous injection site (PC1 and PC2 left in fig. 5.14) are effectively removed in the resultant images.

### 5.2.5 Discussion

This study presents a dedicated MRI acquisition and reconstruction method for in vivo hyperintense visualization of iron oxide labeled cells. The approach combines 3D radial encoding of a bSSFP sequence and multiple off-resonant reconstructions. The entire procedure results in a higher cellular contrast than attained with standard signal void bSSFP, and the gained sensitivity enhancement allows for cellular imaging at resolutions available on clinical platforms. Compared to other positive contrast cell tracking approaches, the presented method based on sub-voxel effects shows a voxel-localized appearance of the contrast and insensitivity for global  $B_0$  inhomogeneities. Possible banding artifacts of the bSSFP sequence are suppressed by a weighted combination of phase cycled acquisitions.

The performed simulations and measurements confirm that the co-RASOR principle [170, 229] can be applied for the refocusing of off-resonant spins in the sub-voxel dimension influenced by SPIO loaded cells. An interesting finding of the performed work is the characteristic signal variation of dipole perturbers for reconstructions with different resonance offsets. The simulations show that the global frequency offset  $\Delta B_{0\text{add}}(\max(|S|))$  for maximum signal recovery has to be chosen to match the used imaging bandwidth and total iron load. Variations in cellular iron load and accumulation of cells in vivo do not allow for an exact a priori estimation of the actual iron load. Therefore, the calculation of a set of reconstructions with different  $\Delta B_{0\text{add}}$  (denoted as ORRS) is used

## 5. CELL TRACKING WITH 3D RADIAL UTE TRAJECTORIES IN COHERENT STEADY STATE

---

for an automated search for the maximum signal recovery at each voxel. In order to gain a maximum signal recovery, figure 5.8 indicates that small imaging bandwidths are beneficial.

Using highly time-efficient reconstruction algorithms based on CUDA [231], the off-resonant reconstruction spectrum for all image voxels is reconstructed within a minute ( $256^3$  voxels ranging from  $\Delta B_{0_{add}} = -300$  Hz to 300 Hz in steps of 15 Hz). Positive contrast with background suppression is achieved by voxel-wise subtraction of the non-modulated on-resonant image from the hyperintense signal gained through reconstruction with  $\Delta B_{0_{add}}(\max(|S|))$ .

Simulations predict that while assuming an SNR of 25 for a resolution of  $200 \mu\text{m}$ ,  $> 5$  pg Fe per cell are sufficient for detection (Rose criterion:  $\text{CNR} > 5$  [237]) by the proposed subtraction technique compared to 25 pg Fe required for standard on-resonant bSSFP (which is in accordance to simulations by Heyn et al. [102]). In vitro CNR analysis of voxels containing sparsely distributed cells substantiate the additional contrast gain utilized by the difference between on-resonant hypointensity and the point of maximal signal recovery for  $\Delta B_{0_{add}}(\max(|S|))$ . Given the same amount of iron oxide per cell, this contrast enhancement can be employed to enlarge voxel size in order to accelerate image acquisition. CNR box-plots of selected voxels reveal that the off-resonant subtraction gained from a fast  $300 \mu\text{m}$  scan is equal to a  $200 \mu\text{m}$  on-resonant bSSFP acquisition while acquisition time is reduced to  $1/3^{\text{rd}}$ .

In comparison to spoiled gradient echo acquisitions, the bSSFP technique possesses two advantages. First, a high SNR is gained almost independently of the repetition time. Second, both echoes can be employed for off-resonant reconstruction. While GRE suffers from dephasing at later echoes, the main difference between the first and second echo in bSSFP consists in the influence of  $T_2$ , not  $T_2^*$ , as magnetization is refocused at the time point of  $\text{TR}/2$  [132]. Consequentially, as successfully demonstrated in vitro and in vivo, the combination of the two echoes enhances cellular CNR.

The proposed method shows excellent cell detection properties able to highlight the voxel containing the perturber. This is a remarkable difference to  $B_0$  mapping or gradient compensation techniques such as white marker [140] or GRASP [141] which highlight the surrounding volume of susceptibility-shift generating objects. Compared to alternative methods based on mapping  $B_0$  field-offsets [136, 137, 138, 139] for the detection of marked cells, the proposed technique stays fully functional in the vicinity

## 5.2 Single cell detection using off-resonant reconstructions of 3D center-out bSSFP

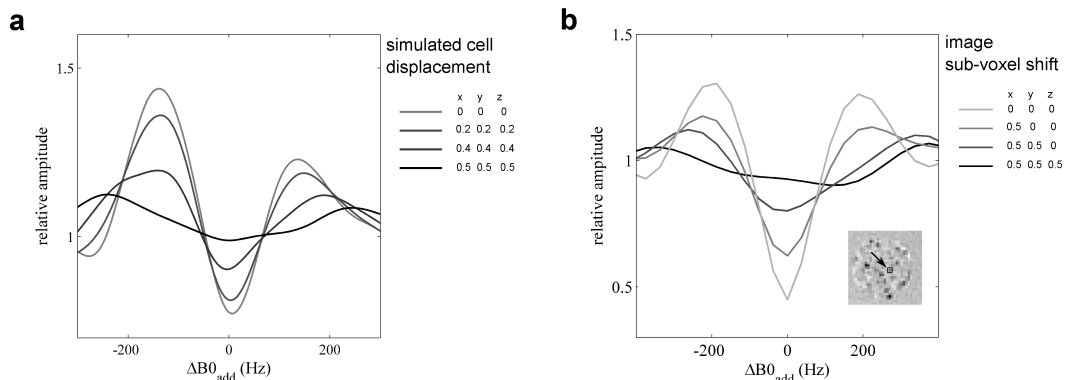


**Figure 5.15:** Change in the ORRS for cells which are not centered with respect to the image grid. **a:** Simulated ORRS from centered to maximally displaced (at the corner of the voxel). A change in magnitude and the off-resonance frequency  $\Delta B0_{add}$  with maximum signal is observed. **b:** Sub-voxel shifted reconstructions of the 200  $\mu\text{m}$  in vitro dataset show the same degradation of the ORRS maxima and minima for a voxel containing an iron loaded cell.

of global  $B_0$ -inhomogeneities related to a bad shim. For a certain global field-offset, the whole off-resonant reconstruction spectrum is shifted by this frequency offset, which does not limit the subtraction contrast if an automated search for the minimum and maximum within the ORRS is performed.

As common to all MR imaging techniques, the method is influenced by partial-volume effects. The change in ORRS due to intra-voxel positioning of cells is shown in figure 5.15. While spectral positioning of the signal maximum of the ORRS changes little with intra-voxel displacement, the reduction in magnitude modulation is quite pronounced. This is confirmed by observations of the ORRS in vitro (fig. 5.11) where magnitude modulation of the three selected voxels gives different CNR values but the spectral positioning of  $\Delta B0_{add}(\max(|S|))$  stays constant. Another issue is a loss in specificity at borders to tissues with a difference in magnetic susceptibility (e.g. fat/muscle at the aorta in fig. 5.14). Discrimination between those hyperintense areas from labeled entities may be addressed by the observation of the ORRS spectral asymmetry. However, the difference in amplitude between positive and negative frequencies observed in vitro (fig. 5.11, 5.15 right) stays below the expectations given by the simulations provided. We assume that the endosomal iron deposition and cellular clustering lead to deviations from the idealized dipolar field pattern simulated. Another way to discriminate cells

## 5. CELL TRACKING WITH 3D RADIAL UTE TRAJECTORIES IN COHERENT STEADY STATE

---

from unwanted off-resonant sources is an optical validation of reconstructed images close to  $\Delta B_{0_{add}}(\max(|S|))$  (e.g. figure 5.14 at  $\Delta B_{0_{add}} = -250$  Hz). In addition to cellular signal amplification, spherical magnitude degradation around the cell caused by shifted hypointensity is observed. This spherically shaped contrast simplifies the discrimination of the cellular contrast from signal variations of the background and, therefore, enhances cellular specificity.

# 6

## Summary & Discussion

### 6.1 Summary

This thesis covers extensions to existing methods and new methodical developments with the aim to amplify MR image contrast of exogeneously labeled stem cells. The presented techniques especially focus on applications in small mammals with the constraints dictated by the hardware of clinical MR devices. Therefore, SNR, cellular CNR, image speed and the reduction of image artifacts have been important aims of optimization. The main contributions of this work are:

- The introduction of an image reconstruction technique based on gradient echo acquisitions which reduces partial volume effects of punctuate magnetic perturbers and, therefore, amplifies contrast to labeled cells. It is demonstrated that additional sampling points, gained through zero-padding preceding the Fourier transform of image reconstruction, access the cellular contrast usually masked by the partial volume effect.
- In the context of stem cell imaging in bone marrow, an existing acquisition strategy (IRON) is further expanded to administer the high lipid content of marrow for cellular signal generation. It is shown that the positive cellular contrast of the IRON technique is further enhanced by the proposed dual spectral selective scheme.

## 6. SUMMARY & DISCUSSION

---

- A 3D radial sampling scheme is employed to compensate for motional artifacts known from Cartesian acquisitions. The stability of this trajectory design for intra- and inter-shot motion is shown to deliver artifact-free background signal in vivo, highly desired for single cell detection. Instantaneous sampling of the FID and spatially isotropic scanning allows for the distinction of labeled cells at very low cellular densities. In addition, it is demonstrated that while using ultra-short echo times, a bright background signal in bone marrow (as required for detection of the negative contrast of SPIO labeled cells) is achieved.
- The successful concept of 3D radial image acquisition is expanded to gain images in the coherent steady state (bSSFP). While bSSFP is well known for its high NMR signal efficiency, a new trajectory is employed to enable bSSFP contrast at high resolutions ( $<160\ \mu\text{m}$ ) with considerably short repetition times ( $<8\ \text{ms}$ ). The main finding of this study is that the developed bUTE approach has the same tissue contrast as standard bSSFP but reduces TR to almost one half. The excellent cell tracking contrast of bSSFP acquisitions is preserved while the half-echo bUTE reduces steady state banding artifacts.
- The efficient bUTE trajectory is further employed and expanded by a dedicated reconstruction technique allowing for a very specific contrast from labeled cells. Hyperintense contrast is formed within the voxel bearing the perturber, exceeding the sensitivity values known from well established negative contrast bSSFP protocols. The method has successfully been applied to SPIO labeled cells in vitro and in vivo on a clinical MRI platform where the acquisition scheme shows robustness to motion and produces high resolution isotropic images.

### 6.2 Discussion & Future Work

Two design rationals for acquisition strategies have been followed to allow a clear identification of iron loaded stem cells in vivo: on the one hand, methods producing hyperintense contrast to background employing the dipolar field produced by the cells, and on the other hand, techniques homogenizing and amplifying background tissue signal which allow for a clear delineation of the pure dissipative, hypointense, cellular

contrast mechanism of  $T_2'$ .

While in the past both strategies have been followed independently, it seems to be very promising to merge both disciplines. Both techniques have prominent features for themselves, namely the high sensitivity of dissipative  $T_2'$  contrast on the one hand and the specific features which the dipolar field pattern delivers on the other. The framework presented in chapter 6.2 already gives an insight into the possibilities such merged techniques offer.

In this context, methods acting on global  $B_0$  distortions produced by condensed cell populations (as presented in chapter 3.2) are poor candidates for a combined approach not only because of their missing single cell detection capabilities. More of a concern is their basis on frequency shifts overreaching multiple voxels, hardly distinguishable from other sources of global field inhomogeneities (e.g. a bad shim). As a result, these techniques do not deliver the desired grade of cellular specificity.

Given the frameworks of chapter 3.1 and 5.2, a gain in specificity of current SPIO based cell tracking is achieved through the cells' dipolar field properties in the mesoscopic, voxel sized domain. Changing the imaging paradigm towards ever smaller resolutions, the dipolar field of single individual cells is accessed. Sensing cellular dipolar field information at this mesoscopic scale has the inherent advantage of being insensitive to other large-scale sources of field inhomogeneities. In addition, the described techniques inherently benefit from the dissipative contrast mechanism of  $T_2'$ .

Studies in chapter 3.1 and 5.2 point out that single cell detection methods, regardless of their acquisition strategy (Cartesian or radial), benefit from corrections of partial volume effects by re-locating the image grid to the position of the perturber. In chapter 3.1, a priori information on the interaction of the dipolar field with the image PSF allowed for an automated realignment and, therefore, a reduction in partial volume effect. The same is conceivable for the off-resonant reconstruction spectrum (ORRS) presented in chapter 5.2. Future work has to investigate if forward simulations of the cellular voxel ORRS may enable correlation-based automated search algorithms to determine true perturber position. A promising scenario based on a similar expansion would be a full spectral analysis of the ORRS which could deliver a compensation for partial volume effects and specific quantitative detection of the labeled cells.

Concerning the work on 3D radial off-resonant reconstructions, future studies will have to balance the benefits of data acquisition in the coherent steady state to the use of

## 6. SUMMARY & DISCUSSION

---

spoiled gradient echo based UTE acquisition. While in general the investigated cell tracking technique works for every 3D half-echo radial sampling scheme, it is quite conceivable that spoiled ultra-short TE acquisitions (chapter 4.2) may perform better in heterogeneous background scenarios such as in the spongy bone compared to the bSSFP acquisition used in the presented work.

### 6.2.1 Translating preclinical cell tracking to clinical practice

Cellular CNR improvements as gained with the off-resonant reconstruction technique stated in chapter 5.2 are important in the sense of biocompatibility and translational research. Two design rationals can be conducted with the gain in cellular image CNR. This could be either a reduction in intra-cellular contrast agent concentration, allowing for enhanced biocompatibility of the technique, or an improved CNR in order to enlarge voxel dimensions, which takes the technique one step further towards translational research.

However, successful translational applications are still missing. The presented work indicates that image resolutions in the range of  $(400 \mu\text{m})^3$  in combination with the robust scanning schemes presented may allow for the detection of sparsely distributed cells. Nonetheless, the data presented benefit from ideal in vitro conditions. No motion at all, a very high coil related SNR and a homogeneous background signal are conditions which are unlikely to be found in vivo. Even if a well suited surface coil and a field of view closed to the surface are employed, the SNR efficiency of the clinical image setup will be lower than delivered by the small animal coils used in the presented studies. Assuming an image SNR 4-fold smaller compared to the preclinical experiments, 16 averages and a resultant acquisition time of 22 minutes will lead to comparable SNR values as presented with the preclinical setup in chapter 5.2. In this scenario it is questionable if the patient is able to stay motionless for the time of acquisition in order to enable a clearly depicted  $400 \mu\text{m}$  scan. However, in recent years new coil developments based on cryogenically cooled hardware reach SNR gains of more than 2-fold, which would reduce the mentioned scan time to less than 5 minutes.

All in all, the feasibility of clinical cell tracking studies will be restricted by the imaging region of interest. Studies of stem cell infiltration into bone marrow have good chances to get clinical practice due to surface-near depots of haem active cell populations in the iliac crest.

Finally, the methods developed within this work provide a framework to perform pre-clinical cell tracking on clinical MR hardware through motion insensitive high resolution imaging protocols facilitating desirable tissue signal properties and data processing schemes which essentially enhance the sensitivity to iron labeled cells.

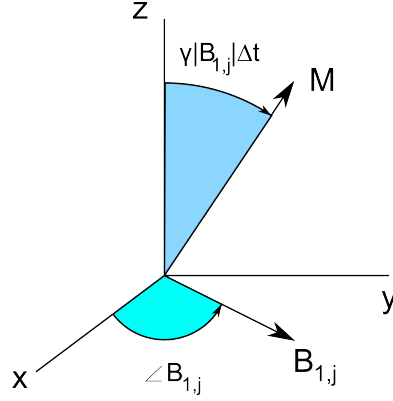
## 6. SUMMARY & DISCUSSION

---

Appendix A

Shinnar Le Roux (SLR)  
Transform

**Figure A.1:** Nutation caused by the  $j$ th hard pulse.



### A.1 SLR-based RF pulse design

Instead of a 3x3 orthogonal rotation matrix  $SO(3)$  as in equation 3.10, a 2x2 unitary matrix is used, so called unit quaternions or  $SU(2)$ , to describe rotations in 3D:

$$Q = \begin{bmatrix} \alpha & -\beta^* \\ \beta & \alpha \end{bmatrix}$$

$$\alpha = \cos(\Phi/2) - in_z \sin(\Phi/2) \tag{A.1}$$

$$\beta = -i(n_x + in_y) \sin(\Phi/2)$$

where  $\alpha$  and  $\beta$  are the Cayley-Klein parameters and  $\vec{n} = n_x\vec{e}_x + n_y\vec{e}_y + n_z\vec{e}_z$  is the axis of rotation with  $\Phi$  the rotation angle. The Cayley-Klein parameters can be used to describe a vector in 3D-space. This 2x1 complex vector is called spinor and represents the actual magnetization. A spinor can be understood, in simple terms, as  $\alpha$  is the component which corresponds to the  $z$  direction of the magnetization and  $\beta$  describes the transversal component  $M_{\perp} = M_x + iM_y$ . In the initial condition  $M_z = M_0$  the spinor describing the magnetization vector is:

$$s_0 = \begin{bmatrix} \alpha \\ \beta \end{bmatrix} = \begin{bmatrix} 1 \\ 0 \end{bmatrix}. \tag{A.2}$$

The rotation caused by one hard pulse  $B_{1,j}$  is shown in figure A.1 and is described by

the Cayley-Klein parameters  $C_j$  and  $S_j$ . Additionally for each hard pulse the result of the free precession over the hard pulse duration  $\Delta t$  is included by the matrix product:

$$\begin{aligned}
 Q_j &= \begin{bmatrix} C_j & -S_j^* \\ S_j & C_j \end{bmatrix} \begin{bmatrix} z^{1/2} & 0 \\ 0 & z^{-1/2} \end{bmatrix} \\
 C_j &= \cos(\gamma |B_{1,j}| \Delta t/2) \\
 S_j &= ie^{i\angle B_{1,j}} \sin(\gamma |B_{1,j}| \Delta t/2) \\
 z &= e^{j\Delta\omega\Delta t}.
 \end{aligned} \tag{A.3}$$

If a sequence of  $n$  pulses is applied, the net rotation can be calculated as the product of the individual rotations  $Q_j$ :

$$Q = Q_n Q_{n-1} \cdots Q_1. \tag{A.4}$$

In order to get rid of half-powers of  $z$ , the spinors describing the magnetization at timepoint  $j$ ,  $\alpha_j$  and  $\beta_j$ , are modified to

$$\begin{aligned}
 A_j &= z^{-j/2} \alpha_j \\
 B_j &= z^{-j/2} \beta_j.
 \end{aligned} \tag{A.5}$$

Including the definition of the hard-pulse rotation in Eq.A.3, the magnetization at timepoint  $j$  is calculated by the recursion:

$$\begin{bmatrix} A_j \\ B_j \end{bmatrix} = \begin{bmatrix} C_j & -S_j^* z^{-1} \\ S_j & C_j z^{-1} \end{bmatrix} \begin{bmatrix} A_{j-1} \\ B_{j-1} \end{bmatrix}. \tag{A.6}$$

With the initial condition for the magnetization in Eq.A.2, and after  $n$  hard pulses, the

## A. SHINNAR LE ROUX (SLR) TRANSFORM

---

Cayley-Klein parameters are (n-1) order polynomials in  $z^{-1}$ :

$$A_n(z) = \sum_{j=0}^{n-1} a_j z^{-j}$$

$$B_n(z) = \sum_{j=0}^{n-1} b_j z^{-j},$$
(A.7)

with

$$z^{-1} = e^{-i\Delta\omega\Delta t}.$$
(A.8)

Equation A.7 maps the RF pulse  $B_1(t)$  into two complex polynomials called the SLR transform. Key is that the base of the polynomials contains the phase evolution in time, just like a finite impulse response filter. It can be shown [178], that the constant term of the polynomial  $A_n$  is a product of all  $C_j$ , which for small tip angles become 1 ( $C_j = \cos(\gamma |B_{1,j}| \Delta t/2) \approx 1$ ) and every higher order term has at least one factor  $S_j$  included which tends towards zero for the small tip angle approximation ( $S_j = ie^{i\angle B_{1,j}} \sin(\gamma |B_{1,j}| \Delta t/2) \approx 0$ ).

The first step at the inverse problem is to find the polynomial  $B_n(z)$  which has a transfer function matching the desired spectral response of the RF pulse. At this point, it is important to point out that  $\beta$  describes the transversal magnetization  $M_\perp$ . The polynomial  $B_n(z)$  should be chosen to approximate the sine of half the desired rotation angle as given in equation A.1 with a linear phase. Other approaches are for example minimum phase designs which do not need a slice refocusing gradient at the expense of RF power or maximum phase designs which produce a maximal phase dispersion over the excited spectral region used for spoiling the transversal magnetization. Other properties of the  $B_n(z)$  polynomial are the width of the transition bands as well as in-band and out-of-band ripple. References [185, 238, 239] give a deeper insight into FIR filter design. According to the definition of  $z$  in equation A.8,  $|z| = 1$ , the polynomial  $A_n(z)$  can be calculated out of  $B_n(z)$  since they have to satisfy the magnitude constraint:

$$|A_n(z)|^2 + |B_n(z)|^2 = 1.$$
(A.9)

The phase of  $A_n(z)$  is chosen to fulfill a constraint which is most common the minimization of RF energy e.g. a minimal phase polynomial.

For the inverse transform, the goal is to derive the actual  $C_j$ ,  $S_j$  parameters out of  $A_n(z)$  and  $B_n(z)$  in order to calculate tip angle  $\Phi$  and phase of the hard pulses at the individual timepoints  $j$ . This is done by the backward recursion from equation A.6.

The inverse of the rotational matrix is:

$$\begin{bmatrix} C_j & -S_j^* z^{-1} \\ S_j & C_j z^{-1} \end{bmatrix}^{-1} = \begin{bmatrix} C_j & S_j^* \\ -S_j^* z & C_j z \end{bmatrix}, \quad (\text{A.10})$$

therefore

$$\begin{bmatrix} A_{j-1} \\ B_{j-1} \end{bmatrix} = \begin{bmatrix} C_j & S_j^* \\ -S_j^* z & C_j z \end{bmatrix} \begin{bmatrix} A_j \\ B_j \end{bmatrix} \quad (\text{A.11})$$

$$= \begin{bmatrix} C_j A_j + S_j^* B_j \\ z(-S_j A_j + C_j B_j) \end{bmatrix}. \quad (\text{A.12})$$

As the polynomials  $A_n(z)$   $B_n(z)$  are always of order  $(n-1)$ , both polynomials have to be reduced by one order within one backward recursion. Equation A.12 states that for  $A_{j-1}$  the coefficients of the highest power of  $A_j$  and  $B_j$  ( $A_{j,j-1}, B_{j,j-1}$ ) and for  $B_{j-1}$  the constant term of  $A_j$  and  $B_j$  ( $A_{j,0}, B_{j,0}$ ) has to drop out. Those constraints are used to calculate the RF properties of the segment  $j$  with:

$$\begin{aligned} C_j A_{j,j-1} + S_j^* B_{j,j-1} &= 0 \\ -S_j A_{j,0} + C_j B_{j,0} &= 0 \end{aligned} \quad (\text{A.13})$$

it can be shown [178] that those equations are equivalent. Using the second constraint,  $B_{1,j}$  is calculated:

## A. SHINNAR LE ROUX (SLR) TRANSFORM

---

$$\frac{B_{j,0}}{A_{j,0}} = \frac{S_j}{C_j} \quad (\text{A.14})$$

$$= \frac{ie^{i\angle B_{1,j}} \sin(\gamma |B_{1,j}| \Delta t/2)}{\cos(\gamma |B_{1,j}| \Delta t/2)} \quad (\text{A.15})$$

$$|B_{1,j}| = \frac{2}{\gamma \Delta t} \tan^{-1} \left| \frac{B_{j,0}}{A_{j,0}} \right| \quad (\text{A.16})$$

$$\angle B_{1,j} = \angle \left( -\frac{iB_{j,0}}{A_{j,0}} \right). \quad (\text{A.17})$$

# References

- [1] HERTER-SPRIE G. S., KUNG A. L., AND WONG K.-K. **New cast for a new era : preclinical cancer drug development revisited.** *The Journal of Clinical Investigation.*, **123**(9):3639–3645, 2013. 1
- [2] WESSELS J. T., BUSSE A. C., MAHRT J., DULLIN C., GRABBE E., AND MUELLER G. A. **In vivo imaging in experimental preclinical tumor researchA review.** *Cytometry Part A*, **71A**(8):542–549, 2007. 1
- [3] FASS L. **Imaging and cancer: a review.** *Molecular oncology*, **2**(2):115–52, August 2008. 1
- [4] FRANGIONI J. **In vivo near-infrared fluorescence imaging.** *Current Opinion in Chemical Biology*, **7**(5):626–634, October 2003. 1
- [5] KHALIL M. M., TREMOLEDA J. L., BAYOMY T. B., AND GSELL W. **Molecular SPECT Imaging: An Overview.** *International Journal of Molecular Imaging*, **2011**:796025–796040, January 2011. 1
- [6] CLARK D. AND BADEA C. **Micro-CT of rodents: State-of-the-art and future perspectives.** *Physica Medica*, **30**(6):619 – 634, 2014. 1
- [7] BADEA C. T., DRANGOVA M., HOLDSWORTH D. W., AND JOHNSON G. A. **In vivo small-animal imaging using micro-CT and digital subtraction angiography.** *Physics in Medicine and Biology*, **53**(19):R319, 2008. 1
- [8] HERMANN P., KOTEK J., KUBÍČEK V., AND LUKEŠ I. **Gadolinium(III) complexes as MRI contrast agents: ligand design and properties of the complexes.** *Dalton Transactions*, (23):3027–3047, June 2008. 1
- [9] ZHANG Y., DODD S. J., HENDRICH K. S., WILLIAMS M., AND HO C. **Magnetic resonance imaging detection of rat renal transplant rejection by monitoring macrophage infiltration.** *Kidney International*, **58**(3):1300–1310, September 2000. 1, 2
- [10] WEBER R., RAMOS-CABRER P., AND HOEHN M. **Present status of magnetic resonance imaging and spectroscopy in animal stroke models.** *Journal of cerebral blood flow and metabolism: official journal of the International Society of Cerebral Blood Flow and Metabolism*, **26**(5):591–604, May 2006. 1, 2
- [11] WILLIAMS J. B., YE Q., HITCHENS T. K., KAUFMAN C. L., AND HO C. **MRI detection of macrophages labeled using micrometer-sized iron oxide particles.** *Journal of Magnetic Resonance Imaging*, **25**(6):1210–1218, June 2007. 1, 2, 31
- [12] KRAITCHMAN D. L. AND BULTE J. W. M. **Imaging of stem cells using MRI.** *Basic research in cardiology*, **103**(2):105–113, March 2008. 1, 2, 19
- [13] YANG Y., SCHUMACHER A., YANG Y., LIU J., SHI X., HILL W. D., AND HU T. C.-C. **Monitoring bone marrow-originated mesenchymal stem cell traffic to myocardial infarction sites using magnetic resonance imaging.** *Magnetic Resonance in Medicine*, **65**(5):1430–1436, 2011. 1, 2
- [14] KRAITCHMAN D. L., GILSON W. D., AND LORENZ C. H. **Stem cell therapy: MRI guidance and monitoring.** *Journal of Magnetic Resonance Imaging*, **27**(2):299–310, 2008. 2
- [15] DIWOKY C., GUNGL D., STRUNK D., AND STOLLBERGER R. **Enhanced contrast of punctuate paramagnetic structures through zero-padding.** *Proceedings of the 22th Annual Meeting of ISMRM, Milan, Italy*, page 2806, 2014. 4
- [16] DIWOKY C., REINISCH A., STRUNK D., AND STOLLBERGER R. **MRI of Stem Cells in Bone Marrow, Graz, Austria.** *ÖGMP Annual Meeting and 3rd AISCMP Meeting*, May 2008. 4
- [17] DIWOKY C., REINISCH A., NEUMAYER B., STRUNK D., AND STOLLBERGER R. **High Sensitivity Positive Contrast Imaging of Stem Cells in Bone Marrow.** *World Molecular Imaging Congress, Nice, France*, 2008. 4
- [18] DIWOKY C., LIEBMANN D., REINISCH A., HOFMANN N. A., STRUNK D., AND STOLLBERGER R. **Robust In-vivo Detection of SPIO Labeled Cells with MRI.** *Proceedings of the BioNanoMed, Krems, Austria*, 2012. 4
- [19] DIWOKY C., REINISCH A., GROSS D., LEHMANN V., STRUNK D., AND STOLLBERGER R. **UTE Imaging for Single Cell Detection with Positive Contrast.** *Proceedings of the 17th Annual Meeting of ISMRM, Montral, Qubec, Canada*, page 804, 2009. 4
- [20] DIWOKY C., REINISCH A., KNOLL F., NEUMAYER B., STRUNK D., AND STOLLBERGER R. **On Possible Pitfalls in Working on SPIO Labeled Cells with 2D UTE Sequences.** *Proceedings of the 18th Annual Meeting of ISMRM, Stockholm, Schweden*, page 1875, 2010. 4
- [21] DIWOKY C. AND STOLLBERGER R. **3D Radial bUTE.** *Proceedings of the 19th Annual Meeting of ISMRM, Montral, Qubec, Canada*, page 387, 2011. 5
- [22] DIWOKY C., LIEBMANN D., NEUMAYER B., REINISCH A., KNOLL F., STRUNK D., AND STOLLBERGER R. **Positive contrast of SPIO-labeled cells by off-resonant reconstruction of 3D radial half-echo bSSFP.** *NMR in Biomedicine*, pages : epub ahead of print, DOI:10.1002/nbm.3229, November 2014. 5, 118
- [23] PURCELL E. M., TORREY H. C., AND POUND R. V. **Resonance Absorption by Nuclear Magnetic Moments in a Solid.** *Physical Review*, **69**(1-2):37–38, January 1946. 8
- [24] BLOCH F., HANSEN W. W., AND PACKARD M. **Nuclear Induction.** *Physical Review*, **69**(3-4):127–127, February 1946. 8

## REFERENCES

---

- [25] BLOCH F. **Nuclear Induction.** *Physical Review*, **70**(7-8):460–474, October 1946. 8
- [26] HAHN E. L. **Spin Echoes.** *Physical Review*, **80**(4):580–594, November 1950. 9, 66
- [27] GERALDES C. F. G. C. AND LAURENT S. **Classification and basic properties of contrast agents for magnetic resonance imaging.** *Contrast Media & Molecular Imaging*, **4**(1):1–23, 2009. 10
- [28] BLOEMBERGEN N., PURCELL E. M., AND POUND R. V. **Relaxation Effects in Nuclear Magnetic Resonance Absorption.** *Physical Review*, **73**(7):679–712, April 1948. 10, 11, 12
- [29] SOLOMON I. **Relaxation Processes in a System of Two Spins.** *Physical Review*, **99**(2):559–565, July 1955. 10, 11, 12
- [30] GUERON M. **Nuclear relaxation in macromolecules by paramagnetic ions: a novel mechanism.** *Journal of Magnetic Resonance*, **19**(1):58–66, July 1975. 10, 11
- [31] CRANGLE J. *Solid-state magnetism.* Van Nostrand Reinhold, New York, 1991. 12
- [32] NÉEL L. **Théorie du tramage magnétique des ferromagnétiques en grains fins avec applications aux terres cuites.** *Annales Geophysicae*, pages 99–136, 1949. 12
- [33] TORREY H. **Bloch Equations with Diffusion Terms.** *Physical Review*, **104**:563–565, Nov 1959. 14
- [34] YABLONSKIY D. A. AND HAACKE E. M. **Theory of NMR signal behavior in magnetically inhomogeneous tissues: the static dephasing regime.** *Magnetic Resonance in Medicine*, **32**(6):749–763, December 1994. 14, 16, 30, 66, 91
- [35] BOWEN C. V., ZHANG X., SAAB G., GAREAU P. J., AND RUTT B. K. **Application of the static dephasing regime theory to superparamagnetic iron-oxide loaded cells.** *Magnetic Resonance in Medicine*, **48**(1):52–61, July 2002. 14, 16, 26, 27, 28, 31, 60, 66, 100, 119
- [36] GILLIS P. AND KOENIG S. H. **Transverse relaxation of solvent protons induced by magnetized spheres: Application to ferritin, erythrocytes, and magnetite.** *Magnetic Resonance in Medicine*, **5**(4):323–345, 1987. 14, 15
- [37] YABLONSKIY D. A. **Quantitation of intrinsic magnetic susceptibility-related effects in a tissue matrix. Phantom study.** *Magnetic Resonance in Medicine*, **39**(3):417–428, 1998. 14, 15, 66
- [38] CARAVAN P., ELLISON J. J., McMURRY T. J., AND LAUFFER R. B. **Gadolinium(III) Chelates as MRI Contrast Agents: Structure, Dynamics, and Applications.** *Chemical reviews*, **99**(9):2293–2352, September 1999. 18
- [39] HERMANN P., KOTEK J., KUBEK V., AND LUKE I. **Gadolinium(III) complexes as MRI contrast agents: ligand design and properties of the complexes.** *Dalton Transactions*, (23):3027–3047, June 2008. 18
- [40] AIME S., CABELLA C., COLOMBATTO S., GENINATTI CRICH S., GIANOLIO E., AND MAGGIONI F. **Insights into the use of paramagnetic Gd(III) complexes in MR-molecular imaging investigations.** *Journal of Magnetic Resonance Imaging*, **16**(4):394–406, October 2002. 18
- [41] AHRENS E. T., ROTHBACHER U., JACOBS R. E., AND FRASER S. E. **A model for MRI contrast enhancement using T1 agents.** *Proceedings of the National Academy of Sciences of the United States of America*, **95**(15):8443–8448, July 1998. 18
- [42] ARBAB A. S., LIU W., AND FRANK J. A. **Cellular magnetic resonance imaging: current status and future prospects.** *Expert Review of Medical Devices*, **3**(4):427–439, July 2006. 18
- [43] HAO D., AI T., GOERNER F., HU X., RUNGE V. M., AND TWEEDLE M. **MRI contrast agents: basic chemistry and safety.** *Journal of Magnetic Resonance Imaging*, **36**(5):1060–1071, November 2012. 18
- [44] AOKI I., TAKAHASHI Y., CHUANG K.-H., SILVA A. C., IGARASHI T., TANAKA C., CHILDS R. W., AND KORETSKY A. P. **Cell labeling for magnetic resonance imaging with the T1 agent manganese chloride.** *NMR in Biomedicine*, **19**(1):50–59, 2006. 18
- [45] GILAD A. A., WALCZAK P., McMAHON M. T., NA H. B., LEE J. H., AN K., HYEON T., VAN ZIJL P. C. M., AND BULTE J. W. M. **MR tracking of transplanted cells with "positive contrast" using manganese oxide nanoparticles.** *Magnetic Resonance in Medicine*, **60**(1):1–7, July 2008. 18
- [46] GILAD A. A., WINNARD J., PAUL T, VAN ZIJL P. C. M., AND BULTE J. W. M. **Developing MR reporter genes: promises and pitfalls.** *NMR in biomedicine*, **20**(3):275–290, May 2007. 18, 19
- [47] WANG K., WANG K., SHEN B., HUANG T., SUN X., LI W., JIN G., LI L., BU L., LI R., WANG D., AND CHEN X. **MR reporter gene imaging of endostatin expression and therapy.** *Molecular Imaging and Biology*, **12**(5):520–529, October 2010. 18
- [48] VANDSBURGER M. H., RADOU L., COHEN B., AND NEEMAN M. **MRI reporter genes: applications for imaging of cell survival, proliferation, migration and differentiation.** *NMR in biomedicine*, **26**(7):872–884, July 2013. 18
- [49] AHRENS E. T. AND BULTE J. W. M. **Tracking immune cells in vivo using magnetic resonance imaging.** *Nature Reviews Immunology*, **13**(10):755–763, September 2013. 18
- [50] CARAVAN P., CLOUTIER N. J., GREENFIELD M. T., McDERMID S. A., DUNHAM S. U., BULTE J. W. M., AMEDIO J., JOHN C, LOOBY R. J., SUPKOWSKI R. M., HORROCKS J., WILLIAM DEW, McMURRY T. J., AND LAUFFER R. B. **The interaction of MS-325 with human serum albumin and its effect on proton relaxation rates.** *Journal of the American Chemical Society*, **124**(12):3152–3162, March 2002. 19
- [51] NAPOLITANO R., PARIANI G., FEDELI F., BARANYAI Z., ASWENDT M., AIME S., AND GIANOLIO E. **Synthesis and relaxometric characterization of a MRI Gd-based probe responsive to glutamic acid decarboxylase enzymatic activity.** *Journal of Medicinal Chemistry*, **56**(6):2466–2477, March 2013. 19

## REFERENCES

- [52] KORETSKY A. **Genetic control of MRI contrast by expression of the transferrin receptor.** *Proceedings of the 4th Annual Meeting of ISMRM, New York, NY, US*, page 5471, 1996. 19
- [53] MELDRUM F. C., HEYWOOD B. R., AND MANN S. **Magneto-ferritin: in vitro synthesis of a novel magnetic protein.** *Science*, **257**(5069):522–523, July 1992. 19
- [54] BULTE J. W., DOUGLAS T., MANN S., FRANKEL R. B., MOSKOWITZ B. M., BROOKS R. A., BAUMGARNER C. D., VYMAZAL J., STRUB M. P., AND FRANK J. A. **Magnetofer-ritin: characterization of a novel superparamag-netic MR contrast agent.** *Journal of Magnetic Resonance Imaging*, **4**(3):497–505, June 1994. 19
- [55] FAN K., CAO C., PAN Y., LU D., YANG D., FENG J., SONG L., LIANG M., AND YAN X. **Magnetoferfritin nanoparticles for targeting and visualizing tumour tissues.** *Nature Nanotechnology*, **7**(12):833–833, December 2012. 19
- [56] BULTE J. W. M. AND KRAITCHMAN D. L. **Iron oxide MR contrast agents for molecular and cellular imag-ing.** *NMR in biomedicine*, **17**(7):484–499, November 2004. 19, 23, 31, 44
- [57] DODD S. J., WILLIAMS M., SUHAN J. P., WILLIAMS D. S., KO-RETSKY A. P., AND HO C. **Detection of single mam-malian cells by high-resolution magnetic reso-nance imaging.** *Biophysical Journal*, **76**(1.1):103–109, January 1999. 19
- [58] FOSTER-GAREAU P., HEYN C., ALEJSKI A., AND RUTT B. K. **Imaging single mammalian cells with a 1.5 T clinical MRI scanner.** *Magnetic Resonance in Medicine*, **49**(5):968–971, 2003. 19, 36, 42
- [59] FRANK J. A., ANDERSON S. A., KALSHI H., JORDAN E. K., LEWIS B. K., YOCUM G. T., AND ARBAB A. S. **Methods for magnetically labeling stem and other cells for de-tection by in vivo magnetic resonance imaging.** *Cytotherapy*, **6**(6):621–625, 2004. 20, 100
- [60] HINDS K. A., HILL J. M., SHAPIRO E. M., LAUKKANEN M. O., SILVA A. C., COMBS C. A., VARNEY T. R., BALABAN R. S., KO-RETSKY A. P., AND DUNBAR C. E. **Highly efficient endo-somal labeling of progenitor and stem cells with large magnetic particles allows magnetic reso-nance imaging of single cells.** *Blood*, **102**(3):867–872, August 2003. 20
- [61] SHAPIRO E. M., SKRTIC S., AND KORETSKY A. P. **Sizing it up: cellular MRI using micron-sized iron oxide particles.** *Magnetic Resonance in Medicine*, **53**(2):329–338, February 2005. 20, 31, 56
- [62] DALDRUP-LINK H. E., RUDELIS M., OOSTENDORP R. A. J., SETTLES M., PIONTEK G., METZ S., ROSENBRUCK H., KELLER U., HEINZMANN U., RUMMENY E. J., SCHLEGEL J., AND LINK T. M. **Targeting of hematopoietic progenitor cells with MR contrast agents.** *Radiology*, **228**(3):760–767, September 2003. 20
- [63] OUDE ENGBERINK R. D., VAN DER POL S. M. A., DÖPP E. A., DE VRIES H. E., AND BLEZER E. L. A. **Comparison of SPIO and USPIO for in vitro labeling of human monocytes: MR detection and cell function.** *Ra-diology*, **243**(2):467–474, May 2007. 20
- [64] WALCZAK P., KEDZIOREK D. A., GILAD A. A., LIN S., AND BULTE J. W. M. **Instant MR labeling of stem cells using magnetoelectroporation.** *Magnetic Resonance in Medicine*, **54**(4):769–774, 2005. 20, 21
- [65] FRANK J. A., MILLER B. R., ARBAB A. S., ZYWICKE H. A., JORDAN E. K., LEWIS B. K., BRYANT L. H., AND BULTE J. W. M. **Clinically Applicable Labeling of Mam-malian and Stem Cells by Combining Superpara-magnetic Iron Oxides and Transfection Agents.** *Radiology*, **228**(2):480–487, August 2003. 21
- [66] ARBAB A., BASHAW L., MILLER B., JORDAN E., LEWIS B., KALISH H., AND FRANK J. **Characterization of Biophysical and Metabolic Properties of Cells Labeled with Superparamagnetic Iron Oxide Nanoparticles and Transfection Agent for Cel-lular MR Imaging.** *Radiology*, **229**(3):838–846, 2003. 21, 22, 23
- [67] ARBAB A. S., YOCUM G. T., WILSON L. B., PARWANA A., JOR-DAN E. K., KALISH H., AND FRANK J. A. **Comparison of transfection agents in forming complexes with ferumoxides, cell labeling efficiency, and cellu-lar viability.** *Molecular Imaging*, **3**(1):24–32, January 2004. 21, 100
- [68] WALCZAK P., RUIZ-CABELLO J., KEDZIOREK D. A., GILAD A. A., LIN S., BARNETT B., QIN L., LEVITSKY H., AND BULTE J. W. M. **Magnetoelectroporation: improved la-beling of neural stem cells and leukocytes for cel-lular magnetic resonance imaging using a single FDA-approved agent.** *Nanomedicine: Nanotechnol-ogy, Biology, and Medicine*, **2**(2):89–94, June 2006. 21
- [69] SUZUKI Y., ZHANG S., KUNDU P., YEUNG A. C., ROBBINS R. C., AND YANG P. C. **In vitro comparison of the biologi-cal effects of three transfection methods for mag-netically labeling mouse embryonic stem cells with ferumoxides.** *Magnetic Resonance in Medicine*, **57**(6):1173–1179, June 2007. 21
- [70] FOSHEIM S. L., FAHLVIK A. K., KLAVENESS J., AND MULLER R. N. **Paramagnetic liposomes as MRI contrast agents: influence of liposomal physicochemical properties on the in vitro relaxivity.** *Magnetic reso-nance imaging*, **17**(1):83–89, January 1999. 21
- [71] KAMALY N. AND MILLER A. D. **Paramagnetic Lipo-some Nanoparticles for Cellular and Tumour Imaging.** *International Journal of Molecular Sciences*, **11**(4):1759–1776, April 2010. 21
- [72] FRASCIONE D., DIWOKY C., ALMER G., OPIRIESSNIG P., VONACH C., GRADAUER K., LEITINGER G., MANGGE H., STOLLBERGER R., AND PRASSL R. **Ultrasmall superparamagnetic iron oxide (USPIO)-based liposomes as magnetic resonance imaging probes.** *International Journal of Nanomedicine*, page 2349, May 2012. 21
- [73] LANGEREIS S., GEELLEN T., GRÜLL H., STRUIJKERS G. J., AND NICOLAY K. **Paramagnetic liposomes for molecu-lar MRI and MRI-guided drug delivery.** *NMR in Biomedicine*, **26**(7):728–744, 2013. 21
- [74] VAN DEN BOS E. J., WAGNER A., MAHRHOLDT H., THOMPSON R. B., MORIMOTO Y., SUTTON B. S., JUDD R. M., AND TAYLOR D. A. **Improved efficacy of stem cell labeling for magnetic resonance imaging studies by the use of cationic liposomes.** *Cell Transplantation*, **12**(7):743–756, 2003. 21

## REFERENCES

---

- [75] JIAO Y., PENG Z.-H., ZHANG J.-Y., QIN J., AND ZHONG C.-P. **Liposome-Mediated Transfer Can Improve the Efficacy of Islet Labeling With Superparamagnetic Iron Oxide.** *Transplantation Proceedings*, **40**(10):3615–3618, December 2008. 21
- [76] TOYOTA T., OHGURI N., MARUYAMA K., FUJINAMI M., SAGA T., AND AOKI I. **Giant Vesicles Containing Superparamagnetic Iron Oxide as Biodegradable Cell-Tracking MRI Probes.** *Analytical Chemistry*, **84**(9):3952–3957, May 2012. 21
- [77] TORCHILIN V. P., RAMMOHAN R., WEISSIG V., AND LEVCHENKO T. S. **TAT peptide on the surface of liposomes affords their efficient intracellular delivery even at low temperature and in the presence of metabolic inhibitors.** *Proceedings of the National Academy of Sciences of the United States of America*, **98**(15):8786–8791, July 2001. 21
- [78] LEWIN M., CARLESSO N., TUNG C. H., TANG X. W., CORY D., SCADDEN D. T., AND WEISSLEDER R. **Tat peptide-derivatized magnetic nanoparticles allow in vivo tracking and recovery of progenitor cells.** *Nature Biotechnology*, **18**(4):410–414, April 2000. 22
- [79] KOK M. B., HAK S., MULDER W. J. M., VAN DER SCHAFT D. W. J., STRLIJKERS G. J., AND NICOLAY K. **Cellular compartmentalization of internalized paramagnetic liposomes strongly influences both T1 and T2 relaxivity.** *Magnetic Resonance in Medicine*, **61**(5):1022–1032, May 2009. 22
- [80] TERRENO E., GENINATTI CRICH S., BELFIORE S., BIANCONE L., CABELLA C., ESPOSITO G., MANAZZA A. D., AND AIME S. **Effect of the intracellular localization of a Gd-based imaging probe on the relaxation enhancement of water protons.** *Magnetic Resonance in Medicine*, **55**(3):491–497, March 2006. 22
- [81] LEWIN M., CLMENT O., BELGUISSE-VALLADIER P., TRAN L., CUNOD C. A., SIAUVE N., AND FRIJA G. **Hepatocyte targeting with Gd-EOB-DTPA: potential application for gene therapy.** *Investigative Radiology*, **36**(1):9–14, January 2001. 22
- [82] CRICH S. G., BIANCONE L., CANTALUPPI V., DU D., ESPOSITO G., RUSSO S., CAMUSSI G., AND AIME S. **Improved route for the visualization of stem cells labeled with a Gd-/Eu-Chelate as dual (MRI and fluorescence) agent.** *Magnetic Resonance in Medicine*, **51**(5):938–944, 2004. 22, 23
- [83] GENINATTI-CRICH S., BARGE A., BATTISTINI E., CABELLA C., COLUCCIA S., LONGO D., MAINERO V., TARONE G., AND AIME S. **Magnetic resonance imaging visualization of targeted cells by the internalization of supramolecular adducts formed between avidin and biotinylated Gd3+ chelates.** *Journal of Biological Inorganic Chemistry*, **10**(1):78–86, January 2005. 22
- [84] AMSALEM Y., MARDOR Y., FEINBERG M. S., LANDA N., MILLER L., DANIELS D., OCHERASHVILLI A., HOLBOVA R., YOSEF O., BARBASH I. M., AND LEOR J. **Iron-Oxide Labeling and Outcome of Transplanted Mesenchymal Stem Cells in the Infarcted Myocardium.** *Circulation*, **116**(11):38–45, November 2007. 23, 35, 36
- [85] PAWELCZYK E., ARBAB A. S., CHAUDHRY A., BALAKUMARAN A., ROBEY P. G., AND FRANK J. A. **In vitro model of bromodeoxyuridine or iron oxide nanoparticle uptake by activated macrophages from labeled stem cells: implications for cellular therapy.** *Stem Cells*, **26**(5):1366–1375, May 2008. 23
- [86] TERROVITIS J., STUBER M., YOUSSEF A., PREECE S., LEPPA M., KIZANA E., SCHÄR M., GERSTENBLITH G., WEISS R. G., MARBN E., AND ABRAHAM M. R. **Magnetic Resonance Imaging Overestimates Ferumoxide-Labeled Stem Cell Survival After Transplantation in the Heart.** *Circulation*, **117**(12):1555–1562, March 2008. 23
- [87] WINTER E., HOGERS B., VAN DER GRAAF L., GITTENBERGER-DE GROOT A., POELMANN R., AND VAN DER WEERD L. **Cell tracking using iron oxide fails to distinguish dead from living transplanted cells in the infarcted heart.** *Magnetic Resonance in Medicine*, **63**(3):817–821, 2010. 23, 35, 36
- [88] TWEEDLE M. F., HAGAN J. J., KUMAR K., MANTHA S., AND CHANG C. A. **Reaction of gadolinium chelates with endogenously available ions.** *Magnetic Resonance Imaging*, **9**(3):409–415, 1991. 23
- [89] GROBNER T. **Gadolinium—a specific trigger for the development of nephrogenic fibrosing dermopathy and nephrogenic systemic fibrosis? Nephrology Dialysis Transplantation**, **21**(4):1104–1108, April 2006. 23
- [90] AGARWAL R., BRUNELLI S. M., WILLIAMS K., MITCHELL M. D., FELDMAN H. I., AND ÜMSCHIED C. A. **Gadolinium-based contrast agents and nephrogenic systemic fibrosis: a systematic review and meta-analysis.** *Nephrology Dialysis Transplantation*, **24**(3):856–863, January 2009. 23
- [91] FENG X., XIA Q., YUAN L., YANG X., AND WANG K. **Impaired mitochondrial function and oxidative stress in rat cortical neurons: implications for gadolinium-induced neurotoxicity.** *Neurotoxicology*, **31**(4):391–398, August 2010. 23
- [92] TONEY G. M., CHAVEZ H. A., IBARRA R., AND JINKINS J. R. **Acute and subacute physiological and histological studies of the central nervous system after intrathecal gadolinium injection in the anesthetized rat.** *Investigative Radiology*, **36**(1):33–40, January 2001. 23
- [93] LI L., GAO F., ZHANG B., LUO B., YANG Z., AND ZHAO J. **Overdosage of intrathecal gadolinium and neurological response.** *Clinical Radiology*, **63**(9):1063–1068, September 2008. 23
- [94] WEISSLEDER R., STARK D. D., ENGELSTAD B. L., BACON B. R., COMPTON C. C., WHITE D. L., JACOBS P., AND LEWIS J. **Superparamagnetic iron oxide: pharmacokinetics and toxicity.** *American Journal of Roentgenology*, **152**(1):167–173, January 1989. 23
- [95] ARBAB A. S., WILSON L. B., ASHARI P., JORDAN E. K., LEWIS B. K., AND FRANK J. A. **A model of lysosomal metabolism of dextran coated superparamagnetic iron oxide (SPIO) nanoparticles: implications for cellular magnetic resonance imaging.** *NMR in Biomedicine*, **18**(6):383–389, 2005. 23

## REFERENCES

- [96] CRICHTON R. R., WILMET S., LEGSSYER R., AND WARD R. J. **Molecular and cellular mechanisms of iron homeostasis and toxicity in mammalian cells.** *Journal of Inorganic Biochemistry*, **91**(1):9–18, July 2002. 23
- [97] SOENEN S. J. H. AND DE CUYPER M. **Assessing cytotoxicity of (iron oxide-based) nanoparticles: an overview of different methods exemplified with cationic magnetoliposomes.** *Contrast Media & Molecular Imaging*, **4**(5):207–219, 2009. 23
- [98] FUKUCHI K., TOMOYASU S., TSURUOKA N., AND GOMI K. **Iron deprivation-induced apoptosis in HL-60 cells.** *FEBS Letters*, **350**(1):139–142, August 1994. 23
- [99] PORRECA E., UCCHINO S., DI FEBBO C., DI BARTOLOMEO N., ANGELUCCI D., NAPOLITANO A. M., MEZZETTI A., AND CUCCURULLO F. **Antiproliferative effect of desferrioxamine on vascular smooth muscle cells in vitro and in vivo.** *Arteriosclerosis and Thrombosis*, **14**(2):299–304, February 1994. 23
- [100] WILHELM C., CEBERS A., BACRI J.-C., AND GAZEAU F. **Deformation of intracellular endosomes under a magnetic field.** *European Biophysics Journal*, **32**(7):655–660, November 2003. 23
- [101] WILHELM C., BAL L., SMIRNOV P., GALY-FAUROUX I., CLMENT O., GAZEAU F., AND EMMERICH J. **Magnetic control of vascular network formation with magnetically labeled endothelial progenitor cells.** *Biomaterials*, **28**(26):3797–3806, September 2007. 23, 100
- [102] HEYN C., BOWEN C. V., RUTT B. K., AND FOSTER P. J. **Detection threshold of single SPIO-labeled cells with FIESTA.** *Magnetic Resonance in Medicine*, **53**(2):312–320, February 2005. 24, 31, 42, 56, 132
- [103] RIEMER J., HOEPKEN H. H., CZERWINSKA H., ROBINSON S. R., AND DRINGEN R. **Colorimetric ferrozine-based assay for the quantitation of iron in cultured cells.** *Analytical Biochemistry*, **331**(2):370–375, August 2004. 26
- [104] ALI M RAD B. J. **Measurement of quantity of iron in magnetically labeled cells: comparison among different UV/VIS spectrometric methods.** *BioTechniques*, **43**(5):627–636, 2007. 26
- [105] KOENIG S. H. AND KELLAR K. E. **Theory of  $1/T_1$  and  $1/T_2$  NMRD profiles of solutions of magnetic nanoparticles.** *Magnetic Resonance in Medicine*, **34**(2):227–233, 1995. 26, 49
- [106] BULTE J. W., BROOKS R. A., MOSKOWITZ B. M., BRYANT J., L H, AND FRANK J. A. **Relaxometry and magnetometry of the MR contrast agent MION-46L.** *Magnetic Resonance in Medicine*, **42**(2):379–384, August 1999. 26
- [107] ROHRER M., BAUER H., MINTOROVITCH J., REQUARDT M., AND WEINMANN H.-J. **Comparison of magnetic properties of MRI contrast media solutions at different magnetic field strengths.** *Investigative Radiology*, **40**(11):715–724, November 2005. 27
- [108] REILLY, CA , MCCONNELL, HM , AND MEISENHEIMER, RG . **Nuclear Magnetic Resonance Spectra of Annular Samples.** *Physical Review*, **98**(1):264–265, 1955. 27
- [109] CHU K. C., XU Y., BALSCHI J. A., AND SPRINGER C. S. **Bulk magnetic susceptibility shifts in nmr studies of compartmentalized samples: use of paramagnetic reagents.** *Magnetic Resonance in Medicine*, **13**(2):239–262, 1990. 27
- [110] LABEL R. M., MENON R. S., AND BOWEN C. V. **Relaxometry model of strong dipolar perturbers for balanced-SSFP: application to quantification of SPIO loaded cells.** *Magnetic Resonance in Medicine*, **55**(3):583–591, March 2006. 31, 40, 60, 115, 121
- [111] HEYN C., RONALD J. A., RAMADAN S. S., SNIR J. A., BARRY A. M., MACKENZIE L. T., MIKULIS D. J., PALMIERI D., BRONDER J. L., STEEG P. S., YONEDA T., MACDONALD I. C., CHAMBERS A. F., RUTT B. K., AND FOSTER P. J. **In vivo MRI of cancer cell fate at the single-cell level in a mouse model of breast cancer metastasis to the brain.** *Magnetic Resonance in Medicine*, **56**(5):1001–1010, November 2006. 31
- [112] HEYN C., RONALD J. A., MACKENZIE L. T., MACDONALD I. C., CHAMBERS A. F., RUTT B. K., AND FOSTER P. J. **In vivo magnetic resonance imaging of single cells in mouse brain with optical validation.** *Magnetic Resonance in Medicine*, **55**(1):23–29, January 2006. 31, 42
- [113] SMIRNOV P., GAZEAU F., BELOEL J.-C., DOAN B. T., WILHELM C., AND GILLET B. **Single-cell detection by gradient echo 9.4 T MRI: a parametric study.** *Contrast Media & Molecular Imaging*, **1**(4):165–174, August 2006. 31
- [114] HAASE A., FRAHM J., MATTHAEI D., HANICKE W., AND MERBOLDT K. D. **FLASH imaging. Rapid NMR imaging using low flip-angle pulses.** *Journal of Magnetic Resonance*, **67**(2):258–266, April 1986. 32
- [115] GIRARD O. M., DU J., AGEMY L., SUGAHARA K. N., KOTAMARAJU V. R., RUOSLAHTI E., BYDDER G. M., AND MATTREY R. F. **Optimization of iron oxide nanoparticle detection using ultrashort echo time pulse sequences: Comparison of  $T_1$ ,  $T_2^*$ , and synergistic  $T_1$   $T_2^*$  contrast mechanisms.** *Magnetic Resonance in Medicine*, **65**(6):1649–1660, 2011. 34
- [116] NORMAN A. B., THOMAS S. R., PRATT R. G., LU S. Y., AND NORGREN R. B. **Magnetic resonance imaging of neural transplants in rat brain using a superparamagnetic contrast agent.** *Brain Research*, **594**(2):279–83, 1992. 35
- [117] HAWRYLAK N., GHOSH P., BROADUS J., SCHLUETER C., GREENOUGH W. T., AND LAUTERBUR P. C. **Nuclear Magnetic Resonance (NMR) Imaging of Iron Oxide-Labeled Neural Transplants.** *Experimental Neurology*, **121**(2):181–192, June 1993. 35
- [118] YEH T. C., ZHANG W., ILDSTAD S. T., AND HO C. **Intracellular labeling of T-cells with superparamagnetic contrast agents.** *Magnetic Resonance in Medicine*, **30**(5):617–625, November 1993. 35
- [119] YEH T. C., ZHANG W., ILDSTAD S. T., AND HO C. **In vivo dynamic MRI tracking of rat T-cells labeled with superparamagnetic iron-oxide particles.** *Magnetic Resonance in Medicine*, **33**(2):200–208, February 1995. 35

## REFERENCES

---

- [120] BULTE J. W. M., ZHANG S.-C., VAN GELDEREN P., HERYNEK V., JORDAN E. K., DUNCAN I. D., AND FRANK J. A. **Neurotransplantation of magnetically labeled oligodendrocyte progenitors: Magnetic resonance tracking of cell migration and myelination.** *Proceedings of the National Academy of Sciences of the United States of America*, **96**(26):15256–15261, December 1999. 35, 44
- [121] HOEHN M., KÜSTERMANN E., BLUNK J., WIEDERMANN D., TRAPP T., WECKER S., FÖCKING M., ARNOLD H., HESCHELER J., FLEISCHMANN B. K., SCHWINDT W., AND BÜHRLE C. **Monitoring of implanted stem cell migration in vivo: A highly resolved in vivo magnetic resonance imaging investigation of experimental stroke in rat.** *Proceedings of the National Academy of Sciences of the United States of America*, **99**(25):16267–16272, October 2002. 35
- [122] JENDELOVÁ P., HERYNEK V., DECROOS J., GLOGAROV K., ANDERSSON B., HUEK M., AND SYKOV E. **Imaging the fate of implanted bone marrow stromal cells labeled with superparamagnetic nanoparticles.** *Magnetic Resonance in Medicine*, **50**(4):767–776, 2003. 35
- [123] LEE I.-H., BULTE J. W. M., SCHWEINHARDT P., DOUGLAS T., TRIFUNOVSKI A., HOFSTETTER C., OLSON L., AND SPENGER C. **In vivo magnetic resonance tracking of olfactory ensheathing glia grafted into the rat spinal cord.** *Experimental Neurology*, **187**(2):509–516, June 2004. 35
- [124] ARBAB A. S., PANDIT S. D., ANDERSON S. A., YOCUM G. T., BUR M., FRENKEL V., KHUU H. M., READ E. J., AND FRANK J. A. **Magnetic resonance imaging and confocal microscopy studies of magnetically labeled endothelial progenitor cells trafficking to sites of tumor angiogenesis.** *Stem Cells*, **24**(3):671–678, March 2006. 35, 36
- [125] RAMOS G. A. AND HARE J. M. **Cardiac cell-based therapy: cell types and mechanisms of actions.** *Cell Transplantation*, **16**(9):951–961, 2007. 35, 36
- [126] ITTRICH H., LANGE C., TÖGEL F., ZANDER A. R., DAHNKE H., WESTENFELDER C., ADAM G., AND NOLTE-ERNSTING C. **In vivo magnetic resonance imaging of iron oxidelabeled, arterially-injected mesenchymal stem cells in kidneys of rats with acute ischemic kidney injury: Detection and monitoring at 3T.** *Journal of Magnetic Resonance Imaging*, **25**(6):1179–1191, 2007. 35, 36
- [127] HUNG T.-C., SUZUKI Y., URASHIMA T., CAFFARELLI A., HOYT G., SHEIKH A. Y., YEUNG A. C., WEISSMAN I., ROBBINS R. C., BULTE J. M., AND YANG P. C. **Multimodality Evaluation of the Viability of Stem Cells Delivered Into Different Zones of Myocardial Infarction.** *Circulation: Cardiovascular Imaging*, **1**(1):6–13, January 2008. 35, 36
- [128] HSIAO J.-K., TAI M.-F., CHU H.-H., CHEN S.-T., LI H., LAI D.-M., HSIEH S.-T., WANG J.-L., AND LIU H.-M. **Magnetic nanoparticle labeling of mesenchymal stem cells without transfection agent: cellular behavior and capability of detection with clinical 1.5 T magnetic resonance at the single cell level.** *Magnetic Resonance in Medicine*, **58**(4):717–724, October 2007. 36
- [129] KÖHLER S., HILLER K.-H., GRISWOLD M., BAUER W. R., HAASE A., AND JAKOB P. M. **NMR-microscopy with TrueFISP at 11.75 T.** *Journal of Magnetic Resonance*, **161**(2):252–257, April 2003. 37, 49
- [130] FREEMAN R. AND HILL H. **Phase and intensity anomalies in fourier transform NMR.** *Journal of Magnetic Resonance*, **4**(3):366–383, June 1971. 37, 38
- [131] BERNSTEIN M. A. AND KING K. F. *Handbook of MRI pulse sequences.* Elsevier, Academic Press, Amsterdam; Boston, 2004. 38, 68, 69, 71, 84, 86, 87, 119, 122
- [132] SCHEFFLER K. AND HENNING J. **Is TrueFISP a gradient-echo or a spin-echo sequence?** *Magnetic Resonance in Medicine*, **49**(2):395–397, February 2003. 39, 108, 121, 132
- [133] BERNAS L. M., FOSTER P. J., AND RUTT B. K. **Imaging iron-loaded mouse glioma tumors with bSSFP at 3 T.** *Magnetic Resonance in Medicine*, **64**(1):23–31, 2010. 42
- [134] MCFADDEN C., MALLETT C. L., AND FOSTER P. J. **Labeling of multiple cell lines using a new iron oxide agent for cell tracking by MRI.** *Contrast Media & Molecular Imaging*, **6**(6):514–522, 2011. 42
- [135] NOAD J., GONZALEZ-LARA L. E., BROUGHTON H. C., MCFADDEN C., CHEN Y., HESS D. A., AND FOSTER P. J. **MRI tracking of transplanted iron-labeled mesenchymal stromal cells in an immune-compromised mouse model of critical limb ischemia.** *NMR in Biomedicine*, **26**(4):458–467, 2013. 42
- [136] STUBER M., GILSON W. D., SCHÄR M., KEDZIOREK D. A., HOFMANN L. V., SHAH S., VONKEN E.-J., BULTE J. W. M., AND KRAITCHMAN D. L. **Positive contrast visualization of iron oxide-labeled stem cells using inversion-recovery with ON-resonant water suppression (IRON).** *Magnetic Resonance in Medicine*, **58**(5):1072–1077, November 2007. 43, 44, 66, 67, 80, 132
- [137] CUNNINGHAM C. H., ARAI T., YANG P. C., MCCONNELL M. V., PAULY J. M., AND CONOLLY S. M. **Positive contrast magnetic resonance imaging of cells labeled with magnetic nanoparticles.** *Magnetic Resonance in Medicine*, **53**(5):999–1005, May 2005. 43, 44, 132
- [138] DHARMAKUMAR R., KOKTZOGLU I., AND LI D. **Generating positive contrast from off-resonant spins with steady-state free precession magnetic resonance imaging: theory and proof-of-principle experiments.** *Physics in Medicine and Biology*, **51**(17):4201–4215, September 2006. 43, 132
- [139] ÇUKUR T., YAMADA M., OVERALL W. R., YANG P., AND NISHIMURA D. G. **Positive contrast with alternating repetition time SSFP (PARTS): a fast imaging technique for SPIO-labeled cells.** *Magnetic Resonance in Medicine*, **63**(2):427–437, February 2010. 43, 44, 132
- [140] SEPPENWOOLDE J. H., VIERGEVER M. A., AND BAKKER C. J. G. **Passive tracking exploiting local signal conservation: the white marker phenomenon.** *Magnetic Resonance in Medicine*, **50**(4):784–790, October 2003. 43, 44, 132

## REFERENCES

- [141] MANI V., BRILEY-SAEBO K. C., ITSKOVICH V. V., SAMBER D. D., AND FAYAD Z. A. **Gradient echo acquisition for superparamagnetic particles with positive contrast (GRASP): sequence characterization in membrane and glass superparamagnetic iron oxide phantoms at 1.5T and 3T.** *Magnetic Resonance in Medicine*, **55**(1):126–135, January 2006. 43, 132
- [142] FRANCONI F., CHAPON C., LE JEUNE J. J., RICHOMME P., AND LEMAIRE L. **Susceptibility gradient quantization by MRI signal response mapping (SIRMA) to dephaser.** *Medical Physics*, **37**(2):877–884, February 2010. 43
- [143] PATIL S., JIRK D., SAUDEK F., HJEK M., AND SCHEFFLER K. **Positive contrast visualization of SPIO-labeled pancreatic islets using echo-dephased steady-state free precession.** *European Radiology*, **21**(1):214–220, January 2011. 43
- [144] DAHNKE H., LIU W., HERZKA D., FRANK J. A., AND SCHAEFFTER T. **Susceptibility gradient mapping (SGM): a new postprocessing method for positive contrast generation applied to superparamagnetic iron oxide particle (SPIO)-labeled cells.** *Magnetic Resonance in Medicine*, **60**(3):595–603, September 2008. 43
- [145] MILLS P. H., HITCHENS T. K., FOLEY L. M., LINK T., YE Q., WEISS C. R., THOMPSON J. D., GILSON W. D., AREPALY A., MELICK J. A., KOCHANEK P. M., HO C., BULTE J. W. M., AND AHRENS E. T. **Automated detection and characterization of SPIO-labeled cells and capsules using magnetic field perturbations.** *Magnetic Resonance in Medicine*, **67**(1):278289, 2012. 43, 44
- [146] MUJA N., COHEN M. E., ZHANG J., KIM H., GILAD A. A., WALCZAK P., BEN-HUR T., AND BULTE J. W. **Neural precursors exhibit distinctly different patterns of cell migration upon transplantation during either the acute or chronic phase of EAE: A serial MR imaging study.** *Magnetic Resonance in Medicine*, **65**(6):1738–1749, 2011. 44
- [147] MARZOLA P., OSCULATI F., AND SBARBATI A. **High field MRI in preclinical research.** *European Journal of Radiology*, **48**(2):165–170, November 2003. 45
- [148] KÖHLER S., HILLER K.-H., GRISWOLD M., BAUER W. R., HAASE A., AND JAKOB P. M. **NMR-microscopy with True-FISP at 11.75T.** *Journal of Magnetic Resonance*, **161**(2):252–257, April 2003. 45
- [149] EDELSTEIN W. A., GLOVER G. H., HARDY C. J., AND REDINGTON R. W. **The intrinsic signal-to-noise ratio in NMR imaging.** *Magnetic Resonance in Medicine*, **3**(4):604–618, 1986. 45
- [150] CALLAGHAN P. T. *Principles of Nuclear Magnetic Resonance Microscopy.* Oxford University Press, New York, 1993. 45, 46, 47, 51, 52, 65
- [151] MACOVSKI A. **Noise in MRI.** *Magnetic Resonance in Medicine*, **36**(3):494–497, 1996. 45
- [152] WATSON P. E., WATSON I. D., AND BATT R. D. **Total body water volumes for adult males and females estimated from simple anthropometric measurements.** *The American Journal of Clinical Nutrition*, **33**(1):27–39, January 1980. 46
- [153] HAACKE E. M. *Magnetic resonance imaging: physical principles and sequence design.* Wiley-Liss, New York, 1999. 46, 58, 109
- [154] MISPELTER J., LUPU M., AND BRIGUET A. *NMR Probeheads for Biophysical and Biomedical Experiments: Theoretical Principles & Practical Guidelines.* Imperial College Press, London, January 2006. 47
- [155] DE BAZELAIRE C. M. J., DUHAMEL G. D., ROFSKY N. M., AND ALSOP D. C. **MR imaging relaxation times of abdominal and pelvic tissues measured in vivo at 3.0 T: preliminary results.** *Radiology*, **230**(3):652–659, March 2004. 49, 69, 72, 122
- [156] STANISZ G. J., ODOBINA E. E., PUN J., ESCARAVAGE M., GRAHAM S. J., BRONSKILL M. J., AND HENKELMAN R. M. **T<sub>1</sub>, T<sub>2</sub> relaxation and magnetization transfer in tissue at 3T.** *Magnetic Resonance in Medicine*, **54**(3):507–512, September 2005. 49, 69, 109, 122
- [157] PRANTNER A. M., BRETTHORST G. L., NEIL J. J., GARBOW J. R., AND ACKERMAN J. J. **Magnetization transfer induced biexponential longitudinal relaxation.** *Magnetic Resonance in Medicine*, **60**(3):555–563, 2008. 49
- [158] BEUF O., JAILLON F., AND SAINT-JALMES H. **Small-animal MRI: signal-to-noise ratio comparison at 7 and 1.5 T with multiple-animal acquisition strategies.** *Magnetic Resonance Materials in Physics, Biology and Medicine*, **19**(4):202–208, 2006. 49
- [159] HAYES C. E., EDELSTEIN W. A., SCHENCK J. F., MUELLER O. M., AND EASH M. **An efficient, highly homogeneous radiofrequency coil for whole-body NMR imaging at 1.5 T.** *Journal of Magnetic Resonance*, **63**(3):622–628, July 1985. 49, 50
- [160] ROEMER P. B., EDELSTEIN W. A., HAYES C. E., SOUZA S. P., AND MUELLER O. M. **The NMR phased array.** *Magnetic Resonance in Medicine*, **16**(2):192–225, 1990. 50
- [161] PRUESSMANN K. P., WEIGER M., SCHEIDEGGER M. B., AND BOESIGER P. **SENSE: sensitivity encoding for fast MRI.** *Magnetic Resonance in Medicine*, **42**(5):952–962, November 1999. 50
- [162] GRISWOLD M. A., JAKOB P. M., HEIDEMANN R. M., NITTKA M., JELLUS V., WANG J., KIEFER B., AND HAASE A. **Generalized autocalibrating partially parallel acquisitions (GRAPPA).** *Magnetic Resonance in Medicine*, **47**(6):1202–1210, June 2002. 50
- [163] TOGA A. W. AND MAZZIOTTA J. C. *Brain mapping: the methods.* Academic Press, Amsterdam; Boston, 2002. 51
- [164] LIAO J. R., PAULY J. M., BROSNAN T. J., AND PELC N. J. **Reduction of motion artifacts in cine MRI using variable-density spiral trajectories.** *Magnetic Resonance in Medicine*, **37**(4):569–575, April 1997. 51
- [165] CARLSON J. W., DERBY K. A., HAWRYSZKO K. C., AND WEIDEMAN M. **Design and evaluation of shielded gradient coils.** *Magnetic Resonance in Medicine*, **26**(2):191–206, 1992. 52
- [166] TURNER R. **Gradient coil design: A review of methods.** *Magnetic Resonance Imaging*, **11**(7):903–920, 1993. 52

## REFERENCES

---

- [167] LIU F., ZHAO H., AND CROZIER S. **On the induced electric field gradients in the human body for magnetic stimulation by gradient coils in MRI.** *IEEE Transactions on Biomedical Engineering*, **50**(7):804–815, July 2003. 52
- [168] RAYLEIGH . **Investigations in optics, with special reference to the spectroscope.** *Philosophical Magazine Series 5*, **8**(49):261–274, 1879. 52
- [169] BERNSTEIN M. A., FAIN S. B., AND RIEDERER S. J. **Effect of windowing and zero-filled reconstruction of MRI data on spatial resolution and acquisition strategy.** *Journal of Magnetic Resonance Imaging*, **14**(3):270–80, September 2001. 58, 59, 60
- [170] SEEVINCK P. R., DE LEEUW H., BOS C., AND BAKKER C. J. G. **Highly localized positive contrast of small paramagnetic objects using 3D center-out radial sampling with off-resonance reception.** *Magnetic Resonance in Medicine*, **65**(1):146–156, 2011. 65, 118, 120, 131
- [171] MAJUMDAR S., THOMASSO D., SHIMAKAWA A., AND GENANT H. K. **Quantitation of the Susceptibility Difference between Trabecular Bone and Bone Marrow: Experimental Studies.** *Magnetic Resonance in Medicine*, **22**(1):111–127, 1991. 66
- [172] MAJUMDAR S. **Quantitative Study of the Susceptibility Difference between Trabecular Bone and BoneMarrow: Computer Simulations.** *Magnetic Resonance in Medicine*, **22**(1):101–110, 1991. 66
- [173] LIN J. C., AMLING M., NEWITT D. C., SELBY K., SRIVASTAV S. K., DELLING G., GENANT H. K., AND MAJUMDAR S. **Heterogeneity of Trabecular Bone Structure in the Calcaneus Using Magnetic Resonance Imaging.** *Osteoporosis International*, **8**(1):16–24, 1998. 66
- [174] WEHRLI F. W., SONG H. K., SAHA P. K., AND WRIGHT A. C. **Quantitative MRI for the assessment of bone structure and function.** *NMR in Biomedicine*, **19**(7):731–764, 2006. 66
- [175] JOSEPH P. M., AXEL L., AND O'DONNELL M. **Potential problems with selective pulses in NMR imaging systems.** *Medical Physics*, **11**(6):772–777, 1984. 71
- [176] SHINNAR M., BOLINGER L., AND LEIGH J. S. **The use of finite impulse response filters in pulse design.** *Magnetic Resonance in Medicine*, **12**(1):81–87, 1989. 72
- [177] LE ROUX P. **Exact synthesis of radio frequency waveforms.** *Proceedings of the 7th Annual Meeting of SMRM*, page 1049, 1988. 72
- [178] PAULY J., LE ROUX P., NISHIMURA D., AND MACOVSKI A. **Parameter relations for the Shinnar-Le Roux selective excitation pulse design algorithm [NMR imaging].** *IEEE Transactions on Medical Imaging*, **10**(1):53–65, 1991. 72, 144, 145
- [179] CONOLLY S., NISHIMURA D., AND MACOVSKI A. **Optimal control solutions to the magnetic resonance selective excitation problem.** *IEEE Transactions on Medical Imaging*, **5**(2):106–115, 1986. 72
- [180] LAPERT M., ZHANG Y., JANICH M. A., GLASER S. J., AND SUGNY D. **Exploring the Physical Limits of Saturation Contrast in Magnetic Resonance Imaging.** *Scientific Reports*, **2**:589–594, August 2012. 72
- [181] SKINNER T. E., GERSHENZON N. I., NIMBALKAR M., AND GLASER S. J. **Optimal control design of band-selective excitation pulses that accommodate relaxation and RF inhomogeneity.** *Journal of Magnetic Resonance*, **217**:53–60, April 2012. 72
- [182] VINDING M. S., MAXIMOV I. I., TONER Z., AND NIELSEN N. C. **Fast numerical design of spatial-selective rf pulses in MRI using Krotov and quasi-Newton based optimal control methods.** *The Journal of Chemical Physics*, **137**(5):54203–54213, August 2012. 72
- [183] EPSTEIN C. L. **Minimum energy pulse synthesis via the inverse scattering transform.** *Journal of Magnetic Resonance*, **167**(2):185–210, April 2004. 72
- [184] GOLD G. E., HAN E., STAINSBY J., WRIGHT G., BRITAIN J., AND BEAULIEU C. **Musculoskeletal MRI at 3.0 T: relaxation times and image contrast.** *American Journal of Roentgenology*, **183**(2):343–351, 2004. 72
- [185] OPPENHEIM A. V. AND SCHAFER R. W. *Digital signal processing.* Prentice-Hall, London, 1975. 74, 144
- [186] REN J., DIMITROV I., SHERRY A. D., AND MALLOY C. R. **Composition of adipose tissue and marrow fat in humans by 1H NMR at 7 Tesla.** *Journal of Lipid Research*, **49**(9):2055–2062, September 2008. 76
- [187] LAUTERBUR P. C. **Image formation by induced local interactions. Examples employing nuclear magnetic resonance.** *Nature*, **242**:190–191, 1973. 84
- [188] KUMAR A., WELTI D., AND ERNST R. R. **NMR Fourier zeugmatography. 1975.** *Journal of Magnetic Resonance*, **213**(2):495–509, December 2075. 84
- [189] LIKES R. S. **Moving gradient zeugmatography.** *US Patent No: 4,307,343*, 1979. 84
- [190] UECKER M., ZHANG S., VOIT D., MERBOLDT K.-D., AND FRAHM J. **Real-time MRI: recent advances using radial FLASH.** *Imaging in Medicine*, **4**(4):461–476, August 2012. 84
- [191] FENG L., GRIMM R., BLOCK K. T., CHANDARANA H., KIM S., XU J., AXEL L., SODICKSON D. K., AND OTAZO R. **Golden-angle radial sparse parallel MRI: Combination of compressed sensing, parallel imaging, and golden-angle radial sampling for fast and flexible dynamic volumetric MRI.** *Magnetic Resonance in Medicine*, **72**(3):707–717, 2014. 84
- [192] BIANCHI A., OZIER A., OUSOVA O., RAFFARD G., AND CRÉMILLIEUX Y. **Ultrashort-TE MRI longitudinal study and characterization of a chronic model of asthma in mice: inflammation and bronchial remodeling assessment.** *NMR in Biomedicine*, **26**(11):1451–1459, November 2013. 84
- [193] DU J. AND BYDDER G. M. **Qualitative and quantitative ultrashort-TE MRI of cortical bone.** *NMR in Biomedicine*, **26**(5):489–506, May 2013. 84

## REFERENCES

- [194] SERAI S. D., LAOR T., DWEK J. R., ZBOJNIEWICZ A. M., AND CARL M. **Feasibility of ultrashort TE (UTE) imaging of children at 1.5 T.** *Pediatric Radiology*, **44**(1):103–8, January 2014. 84
- [195] GLOVER G. H., PAULY J. M., AND BRADSHAW K. M. **Boron4 1 Imaging with a Three-dimensional Reconstruction Method.** *Journal of Magnetic Resonance Imaging*, **2**(1):47–52, 1992. 86
- [196] WONG S. T. AND ROOS M. S. **A strategy for sampling on a sphere applied to 3D selective RF pulse design.** *Magnetic Resonance in Medicine*, **32**(6):778–84, December 1994. 86, 94
- [197] GLOVER G. H. AND PAULY J. M. **Projection reconstruction techniques for reduction of motion effects in MRI.** *Magnetic Resonance in Medicine*, **28**(2):275–289, December 1992. 86, 89, 90
- [198] SCHEFFLER K. AND HENNIG J. **Reduced circular field-of-view imaging.** *Magnetic Resonance in Medicine*, **40**(3):474–480, 1998. 87
- [199] KAK A. C. AND SLANEY M. *Principles of Computerized Tomographic Imaging.* SIAM, New York, 1988. 87
- [200] O’SULLIVAN J. D. **A Fast Sinc Function Gridding Algorithm for Fourier Inversion in Computer Tomography.** *IEEE Transactions on Medical Imaging*, **4**(4):200–207, 1985. 87
- [201] LAUZON M. L. AND RUTT B. K. **Polar sampling in k-space: Reconstruction effects.** *Magnetic Resonance in Medicine*, **40**(5):769–782, 1998. 87, 89
- [202] KAISER J. **Nonrecursive digital filter design using the  $i0$ -sinh window function.** *IEEE International Symposium on Circuits and Systems*, pages 20–23, 1974. 88
- [203] JACKSON J., MEYER C., NISHIMURA D., AND MACOVSKI A. **Selection of a convolution function for Fourier inversion using gridding [computerised tomography application].** *IEEE Transactions on Medical Imaging*, **10**(3):473–478, 1991. 88
- [204] MISTRETTA C. A. **Undersampled radial MR acquisition and highly constrained back projection (HYPR) reconstruction: potential medical imaging applications in the post-Nyquist era.** *Journal of Magnetic Resonance Imaging*, **29**(3):501–16, March 2009. 89
- [205] HAFNER S. **Fast imaging in liquids and solids with the Back-projection Low Angle ShoT (BLAST) technique.** *Magnetic Resonance Imaging*, **12**(7):1047–1051, 1994. 91
- [206] MADIO D. P. AND LOWE I. J. **Ultra-fast imaging using low flip angles and fids.** *Magnetic Resonance in Medicine*, **34**(4):525–529, 1995. 91
- [207] IDIYATULLIN D., CORUM C., PARK J.-Y., AND GARWOOD M. **Fast and quiet MRI using a swept radiofrequency.** *Journal of Magnetic Resonance*, **181**(2):342–349, August 2006. 91
- [208] GATEHOUSE P. AND BYDDER G. **Magnetic Resonance Imaging of Short T2 Components in Tissue.** *Clinical Radiology*, **58**(1):1–19, January 2003. 91
- [209] HOLMES J. E. AND BYDDER G. M. **MR imaging with ultrashort TE (UTE) pulse sequences: Basic principles.** *Radiography*, **11**(3):163–174, August 2005. 91
- [210] ROBSON M. D. AND BYDDER G. M. **Clinical ultrashort echo time imaging of bone and other connective tissues.** *NMR in Biomedicine*, **19**(7):765–780, 2006. 91
- [211] TYLER D. J., ROBSON M. D., HENKELMAN R. M., YOUNG I. R., AND BYDDER G. M. **Magnetic resonance imaging with ultrashort TE (UTE) PULSE sequences: Technical considerations.** *Journal of Magnetic Resonance Imaging*, **25**(2):279–289, February 2007. 91
- [212] WEIGER M., PRUESSMANN K. P., AND HENNEL F. **MRI with zero echo time: Hard versus sweep pulse excitation.** *Magnetic Resonance in Medicine*, **66**(2):379–389, 2011. 91, 97
- [213] CORUM C., IDIYATULLIN D., MOELLER S., PARK J.-Y., AND GARWOOD M. **Introduction to SWIFT (Sweep Imaging with Fourier Transformation) for Magnetic Resonance Imaging of Materials.** *MRS Proceedings*, **984**, 2012. 91
- [214] PIPE J. G. AND DUERK J. L. **Analytical resolution and noise characteristics of linearly reconstructed magnetic resonance data with arbitrary k-space sampling.** *Magnetic Resonance in Medicine*, **34**(2):170–8, August 1995. 95
- [215] PETERS D. C., DERBYSHIRE J. A., AND MCVEIGH E. R. **Centering the projection reconstruction trajectory: reducing gradient delay errors.** *Magnetic Resonance in Medicine*, **50**(1):1–6, July 2003. 97, 98
- [216] DUYN J. H., YANG Y., FRANK J. A., AND VAN DER VEEN J. W. **Simple correction method for k-space trajectory deviations in MRI.** *Journal of Magnetic Resonance*, **132**(1):150–3, May 1998. 98, 100
- [217] VAALS J. J. V. AND BERGMAN A. H. **Optimization of Eddy-Current Compensation.** *Journal of Magnetic Resonance*, **90**(1):52–70, 1990. 98
- [218] IANNI J. AND GRISSOM W. A. **k-SPIRiT: Non-Cartesian SPIRiT Image Reconstruction with Automatic Trajectory Error Compensation.** In *Proceedings of the 22th Annual Meeting of ISMRM, Milan, Italy*, number c, page 83, 2014. 98
- [219] DIWOKY C., REINISCH A., GROSS D., LEHMANN V., STRUNK D., AND STOLLBERGER R. **Imaging of SPIO Labelled Endothelial Networks at 3, 7 and 11.7 Tesla.** *Proceedings of the 17th Annual Meeting of ISMRM, Honolulu, Hawaii, USA*, page 915, 2009. 100
- [220] SCHALLMOSER K., BARTMANN C., ROHDE E., REINISCH A., KASHOFER K., STADELMEYER E., DREXLER C., LANZER G., LINKESCH W., AND STRUNK D. **Human platelet lysate can replace fetal bovine serum for clinical-scale expansion of functional mesenchymal stromal cells.** *Transfusion*, **47**(8):1436–1446, August 2007. 100
- [221] HOFMANN N. A., REINISCH A., AND STRUNK D. **Isolation and large scale expansion of adult human endothelial colony forming progenitor cells.** *Journal of Visualized Experiments*, **32**, 2009. 100

## REFERENCES

---

- [222] STRUNK D., ROHDE E., LANZER G., AND LINKESCH W. **Phenotypic characterization and preclinical production of human lineage-negative cells for regenerative stem cell therapy.** *Transfusion*, **45**(3):315–326, March 2005. 100
- [223] SCHEFFLER K. AND LEHNHARDT S. **Principles and applications of balanced SSFP techniques.** *European Radiology*, **13**(11):2409–18, November 2003. 106, 107
- [224] OSHINSKI J. N., DELFINO J. G., SHARMA P., GHARIB A. M., AND PETTIGREW R. I. **Cardiovascular magnetic resonance at 3.0 T: current state of the art.** *Journal of Cardiovascular Magnetic Resonance*, **12**(1):55, January 2010. 106
- [225] BIERI O. AND SCHEFFLER K. **Fundamentals of balanced steady state free precession MRI.** *Journal of Magnetic Resonance Imaging*, **38**(1):2–11, July 2013. 106
- [226] STEHNING C., BÖRNERT P., NEHRKE K., EGGERS H., AND STUBER M. **Free-breathing whole-heart coronary MRA with 3D radial SSFP and self-navigated image reconstruction.** *Magnetic Resonance in Medicine*, **54**(2):476–80, August 2005. 106
- [227] ÇUKUR T., BANGERTER N. K., AND NISHIMURA D. G. **Enhanced spectral shaping in steady-state free precession imaging.** *Magnetic Resonance in Medicine*, **58**(6):1216–1223, 2007. 108, 124
- [228] DIWOKY C., GUNGL D., REINISCH A., HOFFMANN N. A., STRUNK D., AND STOLLBERGER R. **Off-Resonant Reconstruction of Balanced 3D-Radial Acquisitions with Half-Echo Sampling for Unique Cell Tracking Contrast.** *Proceedings of the 21th Annual Meeting of ISMRM, Salt Lake City, Utah, USA*, page 765, 2013. 118
- [229] DE LEEUW H., SEEVINCK P. R., AND BAKKER C. J. G. **Center-out radial sampling with off-resonant reconstruction for efficient and accurate localization of punctate and elongated paramagnetic structures.** *Magnetic Resonance in Medicine*, **69**(6):1611–1622, 2012. 118, 131
- [230] RAHMER J., BÖRNERT P., GROEN J., AND BOS C. **Three-dimensional radial ultrashort echo-time imaging with T2 adapted sampling.** *Magnetic Resonance in Medicine*, **55**(5):1075–1082, May 2006. 121
- [231] KNOLL F., SCHWARZL A., DIWOKY C., AND SODICKSON K. **gpuNUFFT - An open source GPU library for 3D regridding with direct Matlab interface.** *Proceedings of the 22th Annual Meeting of ISMRM, Milan, Italy*, page 4397, 2014. 122, 132
- [232] BEATTY P., NISHIMURA D., AND PAULY J. **Rapid gridding reconstruction with a minimal oversampling ratio.** *IEEE Transactions on Medical Imaging*, **24**(6):799–808, 2005. 122
- [233] FESSLER J. AND SUTTON B. **Nonuniform fast Fourier transforms using min-max interpolation.** *IEEE Transactions on Signal Processing*, **51**(2):560 – 574, February 2003. 122
- [234] ZWART N. R., JOHNSON K. O., AND PIPE J. G. **Efficient sample density estimation by combining gridding and an optimized kernel.** *Magnetic Resonance in Medicine*, **67**(3):701–710, 2012. 122
- [235] SCHEFFLER K. **Superresolution in MRI?** *Magnetic Resonance in Medicine*, **48**(2):408; author reply 409, August 2002. 124
- [236] BANGERTER N. K., HARGREAVES B. A., VASANAWALA S. S., PAULY J. M., GOLD G. E., AND NISHIMURA D. G. **Analysis of multiple-acquisition SSFP.** *Magnetic Resonance in Medicine*, **51**(5):1038–1047, May 2004. 131
- [237] ROSE A. **The Sensitivity Performance of the Human Eye on an Absolute Scale.** *Journal of the Optical Society of America*, **38**(2):196–208, February 1948. 132
- [238] PARKS T. W. AND BURRUS C. S. *Digital filter design.* Wiley, New York, 1987. 144
- [239] LIM J. S. AND OPPENHEIM A. V. *Advanced topics in signal processing.* Prentice-Hall, London, 1988. 144

# Curriculum Vitae



## Personal Data

Name: Clemens Diwocky  
Date of Birth: January 17, 1981  
Citizenship: Austrian

## Education

2007 - 2014 Ph.D. study: 'Methodical developments for preclinical stem cell tracking on a clinical 3 Tesla MRI'  
(Graz University of Technology)  
2002 - 2007 Studies in Electrical and Biomedical Engineering  
(Graz University of Technology)  
Graduation to M.Sc. with distinction  
2001 - 2002 Studies in Electrical Engineering  
(Vienna University of Technology)  
1995 - 2000 Secondary College for Electrical Engineering  
(Higher Technical Institute Mödling)  
Graduation Diploma (Reife- und Diplomprüfung) with distinction

## Academic Experience

2014 - present University Assistant  
Medical University of Graz, Department of Neurology  
2013 - 2014 Scientific Assistant

## **CURRICULUM VITAE**

---

2012 - 2013      Graz University of Technology, Institute of Medical Engineering  
Scientific Project Collaborator

2007 - 2012      University of Graz, Institute of Mathematics and Scientific Computing  
University Assistant

Teaching:      Graz University of Technology, Institute of Medical Engineering  
Biosignal Processing Lecture (2009-2012)  
Biosignal Processing Lab (2009-2012)  
Imaging Lab (2009)  
Fundamentals of Biomedical Engineering Lab (2009-2012)

# List of Publications

## Peer Reviewed Journal Publications

- **Diwoy, C.**; Liebmann, D.; Neumayer, B.; Reinisch, A.; Knoll, F.; Strunk, D.; Stollberger, R.: Positive contrast of SPIO-labeled cells by off-resonant reconstruction of 3D radial half-echo bSSFP. - in: *NMR in Biomedicine*, Epub ahead of print, DOI: 10.1002/nbm.3229, 2014
- Magro, M.; Campos, R.; Baratella, D.; Lima, G.; Hol, K.; **Diwoy, C.**; Stollberger, R.; Malina, O.; Aparicio, C.; Zoppellaro, G.; Zbořil, R.; Vianello F.: A Magnetically Drivable Nanovehicle for Curcumin with Antioxidant Capacity and MRI Relaxation Properties. - in: *Chemistry - a European journal* 20(37):11913-11920, 2014
- Zoppellaro, G.; Kolokithas-Ntoukas, A.; Polakova, K.; Tucek, J.; Zboril, R.; Loudos, G.; Fragogeorgi, E.; **Diwoy, C.**; Tomankova, K.; Avgoustakis, K.; Kouzoudis, D.; Bakandritsos, A.: Theranostics of Epitaxially Condensed Colloidal Nanocrystal Clusters, through a Soft Biomineralization Route. - in: *Chemistry of Materials* 26(6):20622074, 2014
- Zoppellaro, G.; Maity, D.; Sedenkova, V.; Tucek, J.; Safarova, K.; Polakova, K.; Tomankova, K.; Stollberger, R.; **Diwoy, C.**; Machala, L.; Zboril, R.: Surface Design of Core-Shell Superparamagnetic Iron Oxide Nanoparticles Drives Record Relaxivity Values in Functional MRI Contrast Agents. - in: *Chemical Communications* 48:11398-11400, 2012
- Frascione, D.; **Diwoy, C.**; Almer, G.; Opriessnig, P.; Vonach, C.; Gradauer, K.; Leitinger, G.; Mangge, H.; Stollberger, R.; Prassl, R.: Ultrasmall superparamag-

## PUBLICATIONS

---

- netic iron oxide (USPIO)-based liposomes as magnetic resonance imaging probes. - in: *International Journal of Nanomedicine* 7:2349-2359, 2012
- Das, S. K.; Eder, S.; Schauer, S.; **Diwoky, C.**; Temmel, H.; Grtl, B.; Gorkiewicz, G.; Tamilarasan, K. P.; Kumari, P.; Trauner, M.; Zimmermann, R.; Vesely, P.; Himmerle, G.; Zechner, R.; Hfler, G.: Adipose Triglyceride Lipase Contributes to Cancer-Associated Cachexia. - in: *Science* 333(6039):233-238, 2011
  - Pantakar, J. V.; Chandak, P. G.; Obrowsky, S.; Pfeifer, T.; **Diwoky, C.**; Uellen, A.; Sattler, W.; Stollberger, R.; Hoefler, G.; Heinemann, A.; Battle, M.; Duncan, S.; Kratky, D.; Levak-Frank, S.: Loss of intestinal GATA4 prevents diet-induced obesity and promotes insulin sensitivity in mice. - in: *American Journal of Physiology / Endocrinology and Metabolism* 300(3):E478-488, 2011
  - Knoll, F.; Clason, C.; **Diwoky, C.**; Stollberger, R.: Adapted Random Sampling Patterns for Accelerated MRI. - in: *Magnetic Resonance Materials in Physics, Biology and Medicine* 24(1):43-50, 2011
  - Knoll, F.; Unger, M.; **Diwoky, C.**; Clason, C.; Pock, T.; Stollberger, R.: Fast reduction of undersampling artifacts in radial MR angiography with 3D total variation on graphics hardware . - in: *Magnetic Resonance Materials in Physics, Biology and Medicine* 23(2):103-114, 2010

## Oral Presentations

- **Diwoky, C.**; Liebmann, D.; Reinisch, A.; Hoffmann, N. A.; Strunk, D.; Stollberger, R.: Off-Resonant Reconstruction of Balanced 3D-Radial Acquisitions with Half-Echo Sampling for Unique Cell Tracking Contrast. - at: International Society for Magnetic Resonance in Medicine: Scientific Meeting & Exhibition 2013, SaltLake City, USA, page 765, 2013
- **Diwoky, C.**; Gungl, D.; Reinisch, A.; Hofmann, N. A.; Strunk, D.; Stollberger, R.: Robust In-vivo Detection of SPIO Labeled Cells with MRI. - at: BioNanoMed 2012, Krems, Austria, 2012

- **Diwoy, C.**; Stollberger, R.: 3D Radial bUTE. - at: International Society for Magnetic Resonance in Medicine: Scientific Meeting & Exhibition 2011, Montreal, Canada, page 387, 2011
- **Diwoy, C.**; Reinisch, A.; Gross, D.; Lehmann, V.; Strunk, D.; Stollberger, R.: UTE Imaging for Single Cell Detection with Positive Contrast. - at: International Society for Magnetic Resonance in Medicine: Scientific Meeting & Exhibition 2009, Honolulu, USA, page 804, 2009
- **Diwoy, C.**; Reinisch A.; Strunk D.; Stollberger R.: MRI of Stem Cells in Bone Marrow. - at: GMP Annual Meeting and 3rd AISCMP Meeting 2008, Graz, Austria, 2008

## Refereed Conference Proceedings

- **Diwoy, C.**; Liebmann, D.; Strunk, D.; Stollberger, R.: Enhanced Contrast of Punctuate Paramagnetic Structures Through Zero-Padding. - in: International Society for Magnetic Resonance in Medicine: Scientific Meeting & Exhibition 2014, page 2806, 2014
- Schloegl, M.; **Diwoy, C.**; Stollberger, R.: Motion Detection for 3D Radial Balanced SSFP Sequences. - in: International Society for Magnetic Resonance in Medicine: Scientific Meeting & Exhibition 2014, page 1604, 2014
- Knoll, F.; Schwarzl, A.; **Diwoy, C.**; Sodickson, D.: gpuNUFFT - An Open Source GPU Library for 3D Re gridding with Direct Matlab Interface. - in: International Society for Magnetic Resonance in Medicine: Scientific Meeting & Exhibition 2014, page 4297, 2014
- Knoll, F.; Block, K. T.; Bredies, K.; **Diwoy, C.**; Axel, L.; Sodickson, D.; Stollberger, R.: Accelerated 3D Radial Imaging with 3D Variational Regularization. - in: International Society for Magnetic Resonance in Medicine: Scientific Meeting & Exhibition 2013, page 2636, 2013
- Petrovic, A.; **Diwoy, C.**; Hassler, E.; Ogris, K.; Scheurer, E.: IDEAL Fat-Water Separation for the Detection and Characterization of Subcutaneous Hemorrhage.

## PUBLICATIONS

---

- in: International Society for Magnetic Resonance in Medicine: Scientific Meeting & Exhibition 2013, page 2420, 2013
- Aigner, C.; **Diwoky, C.**; Stollberger, R.: Development of a pulseoximeter to measure the oxygen saturation and the heartrate of sedated mice. - in: Biomedizinische Technik ; 58, Suppl. 1, 2013
  - Bettermann, K.; Mehta, A.; Lederer, E.; **Diwoky, C.**; Thringer, A.; Mller, H.; Mahajan, V.; Stumptner, C.; Kolbe, T.; Magin, T.; Denk, H.; Lackner, C.; Zatloukal, K.; Haybaeck, J.: Contribution of keratin-18 on steatohepatitis and liver cancer. - in: 45. Jahrestagung der sterreichischen Gesellschaft fr Gastroenterologie und Hepatologie 2012, 2012
  - Mehta, A.; Bettermann, K.; Lederer, E.; **Diwoky, C.**; Thringer, A.; Stumptner, C.; Mueller, H.; Kolbe, T.; Magin, T.; Lackner, C.; Denk, H.; Zatloukal, K.; Haybaeck, J.: Molecular pathogenesis and genetic susceptibility to steatohepatitis induced liver cancer. - in: 40th Keystone Symposia Conference on Molecular and Cellular Biology 2012, 2012
  - Bettermann, K.; Mehta, A.; Lederer, E.; **Diwoky, C.**; Thuringer, A.; Mueller, H.; Mahajan, V.; Stumptner, C.; Kolbe, T.; Magin, T.; Denk, H.; Lackner, C.; Zatloukal, K.; Haybaeck, J.: Steatohepatitis-driven hepatocellular carcinoma. - in: International journal of molecular medicine 30 2012, 2012
  - Almer, G.; Frascione, D.; Gradauer, K.; **Diwoky, C.**; Opriessnig, P.; Stollberger, R.; Mangge, H.; Prassl, R.: Targeted liposomes for imaging of atherosclerotic plaques. - in: BioNanoMed 2012, 2012
  - Frascione, D.; **Diwoky, C.**; Opriessnig, P.; Stollberger, R.; Almer, G.; Mangge, H.; Leitinger, G.; Ruth, P.: Liposomal Contrast Agents for Targeted Molecular Imaging. - in: GMBT Annual Meeting 2011, 2011
  - Reinisch, A.; Etchart, N.; Hoffmann, N.; Ortner, A.; Rohde, E.; Schallmoser, K.; Beham-Schmid, C.; Dullin, C.; **Diwoky, C.**; Hofmeister, A.; Stollberger, R.; Alves, F.; Strunk, D.: Human Vascular Progenitor Cells Can Guide Mesodermal Lineage Choice of Mesenchymal Stem and Progenitor Cells After Co-Transplantation In Vivo. - in: ASH Annual Meeting and Exposition 2010, 2010

- **Diwoky, C.**; Reinisch, A.; Knoll, F.; Neumayer, B.; Strunk, D.; Stollberger, R.: On Possible Pitfalls in Working on SPIO Labelled Cells with 2D UTE Sequences. - in: International Society for Magnetic Resonance in Medicine: Scientific Meeting & Exhibition 2010 , page 1875, 2010
- Neumayer, B.; **Diwoky, C.**; Reinisch, A.; Strunk, D.; Stollberger, R.: Quantification of Cell Density of SPIO-Labelled Cell Populations. - in: International Society for Magnetic Resonance in Medicine: Scientific Meeting & Exhibition 2010, page 4192, 2010
- **Diwoky, C.**; Binter, C.; Strasser, J. K.; Stollberger, R.: Waveform Optimized (Easy to Build) Pulsatile Flow Phantom of the Common Carotid Artery. - in: International Society for Magnetic Resonance in Medicine: Scientific Meeting & Exhibition 2010 , page 1353, 2010
- Neumayer, B.; Eva Elisa, F.; **Diwoky, C.**; Weinberg, A.-M.; Stollberger, R.: Examination of the Correlation between Hypervascularity and Physeal Bone Bridge Formation. - in:International Society for Magnetic Resonance in Medicine: Scientific Meeting & Exhibition 2009, page 851, 2009
- **Diwoky, C.**; Reinisch, A.; Gross, D.; Lehmann, V.; Strunk, D.; Stollberger, R.: Imaging of SPIO Labelled Endothelial Networks at 3, 7 and 11.7 Tesla. - in: International Society for Magnetic Resonance in Medicine: Scientific Meeting & Exhibition 2009 , page 915, 2009
- **Diwoky, C.**; Reinisch, A.; Neumayer, B.; Strunk, D.; Stollberger, R.: High Sensitivity Positive-Contrast Imaging of Stem Cells in Bone Marrow. - in: World Molecular Imaging Congress 2008, 2008
- Reinisch, A.; **Diwoky, C.**; Hoffmann, N.; Schallmoser, K.; Ingolic, E.; Linkesch, W.; Stollberger, R.; Strunk, D.: Magnetic Resonance Imaging of Functional Endothelial Progenitor Cells. - in: World Molecular Imaging Congress 2008, 2008
- Reinisch, A.; **Diwoky, C.**; Hoffmann, N.; Schallmoser, K.; Linkesch, W.; Stollberger, R.; Strunk, D.: Molecular Imaging of Bone Marrow Stromal Cells. - in: Bone Marrow Transplantation 2008, page 432, 2008

## PUBLICATIONS

---

- Fischerauer, E.; Neumayer, B.; **Diwoky, C.**; Lindtner, R.; Stollberger, R.; Hoellwarth, M.; Weinberg, A.-M.: Transphyseal lesion: Is hypervascularity associated with developing physeal bone bridges?. - in: 21. International Symposium on Paediatric Surgical Research 2008, 2008

## Miscellaneous

- ISMRM Educational Travel Stipend, years: 2009, 2010, 2011
- Finalist (3rd place) ISMRM 2012 Challenge: Fat/Water Separation

# Acknowledgements

I am very pleased to take this opportunity to thank numerous people who have accompanied and supported me over the time of my PhD thesis and thus essentially contributed to the completion of this work.

First of all, I would like to express my sincere gratitude to my supervisor Prof. Rudolf Stollberger for his ongoing support and his appreciation for the time needed to establish preclinical basic research in MRI.

I wish to thank Prof. Stefan Ropele, member of my dissertation committee, offering his time and guidance throughout the review of this document.

Moreover, I would like to thank Prof. Dirk Strunk (formerly Department of Haematology, Medical University of Graz) who initiated the idea of stem cell tracking by MRI for our MR research group and who has always been a great supporter of my work. Very special thanks to his team, especially to Andreas Reinisch who put very hard work on establishing the outstanding stem cell labeling protocols presented in this thesis, and to Daniel Liebmann who has taken over the stem cell management after him.

I gratefully thank Alexandra Lipfert for all the support she gave to me in animal imaging and the wonderful time at the MRI Lab Graz.

My sincere thanks go to Alexandra Jammer, who helped to put the sentences of this thesis finally into the right order.

I thank my wonderful colleagues at the Institute of Medical Engineering very heartily, especially my long-term PhD colleagues Bernhard Neumayer, Peter Opriessnig, Andreas Petrovic, Florian Knoll, Manuel Freiberger and Christian Langkammer. I learned a lot while discussing our MR and non-MR related issues at our weekly Stammtisch. I am thankful for the great time we had together.

Very special thanks go to my dear friends Anna Heschl, Andreas Vacek, Johannes Pohl, Paul and Magdalena Fuczek, Bernhard Rafetseder and Alexander Knipel for the long

## **ACKNOWLEDGEMENTS**

---

years of companionship.

Sincere deep thanks to my great sisters Barbara and Sandra and to my parents Edith and Johann Diwoy who have provided me with the great opportunity to reach the highest degree of education. This means the world to me.

Finally, I would like to thank my wife Isabelle for her everlasting love and support and my wonderful son Viktor, they are the best that ever happened to me.